Chapter 10

Scattering and absorption properties of nonspherical particles

The convenient availability and simplicity of the Lorenz–Mie theory has resulted in a widespread practice of treating nonspherical particles (especially those in random orientation) as if they were spheres to which Lorenz–Mie results are applicable. However, the assumption of sphericity is rarely made after first having studied the effects of nonsphericity and concluded that they are negligible but, rather, is usually based upon a perceived lack of practical alternatives. In fact, overwhelming evidence suggests that the scattering properties of nonspherical particles, including those in random orientation, can significantly differ from those of volume- or surface-equivalent spheres. Hence, the goal of this chapter is to provide a brief summary of recent research efforts aimed at a significantly better understanding of the effects of particle shape and morphology on electromagnetic scattering.

10.1 Interference and resonance structure of scattering patterns for nonspherical particles in a fixed orientation; the effects of orientation and size averaging

We have seen in Section 9.1 that scattering patterns for monodisperse spheres are heavily burdened with various interference and resonance features. The interference and resonance structure for monodisperse nonspherical particles in a fixed orientation is even more intricate because it acquires new complex, orientation-specific features. This is demonstrated in Figs. 10.1–10.3, which show the results of *T*-matrix computations of the intensity scattered by three types of particle in various orientations (all "orientations" of a

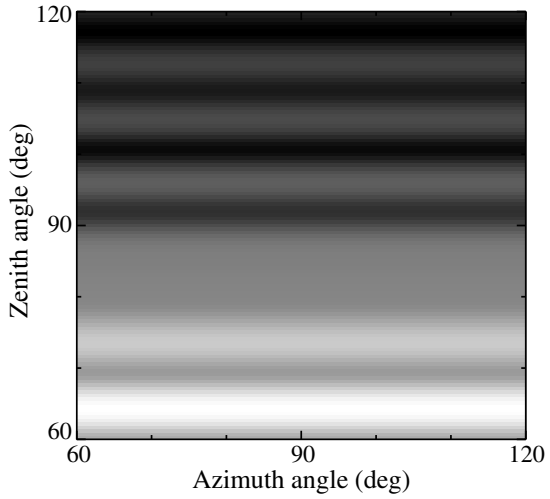

Figure 10.1. Scattered intensity (in arbitrary units) versus $\vartheta^{\rm sca}$ and $\varphi^{\rm sca}$ for a spherical particle illuminated by an unpolarized beam of light incident along the *z*-axis of the laboratory reference frame (cf. Fig. 1.2). The size parameter of the sphere is 20 and the relative refractive index is 1.53 + i0.008.

spherical particle yield, of course, the same scattering pattern). The sphere (Fig. 10.1) and also the spheroid and cylinder with rotation axes oriented along the *z*-axis of the laboratory coordinate system (the upper left panels of Figs. 10.2 and 10.3, respectively) show no azimuthal dependence of the scattered intensity, because the scattering geometry is axially symmetric and the incident light is unpolarized. However, the other panels of Figs. 10.2 and 10.3 demonstrate patchy patterns similar to those shown in Plate 8.1. The number of patches and the complexity of the scattering patterns rapidly mount with growing size parameter (Figs. 10.4 and 10.5), making it increasingly difficult to establish a definitive relationship between the physical and geometrical particle characteristics on the one hand and the structure of the scattering pattern on the other.

Panels (a)–(c) of Plate 10.1 represent another way of looking at the effects of nonsphericity and orientation on scattering patterns. They depict the degree of linear polarization of the scattered light, for unpolarized incident light, versus the zenith angle of the scattering direction and the surface-equivalent-sphere size parameter for monodisperse spheres (a) and for monodisperse, surface-equivalent oblate spheroids with two orientations of the rotation axis relative to the laboratory reference frame (b), (c). The polarization patterns for the spheres and the spheroids in the two fixed orientations are dramatically different. In particular, the lack of axial symmetry for the light-scattering geometry in panel (c) results in non-zero polarization values at $\vartheta^{\rm sca} = 0°$ and 180°.

Plate 10.1(d) shows that the polarization pattern computed for monodisperse spheroids in random orientation is much smoother and less complex than those for spheroids in fixed orientations. This smoothing effect of averaging over orientations is reinforced by averaging over sizes, which totally removes the residual interference

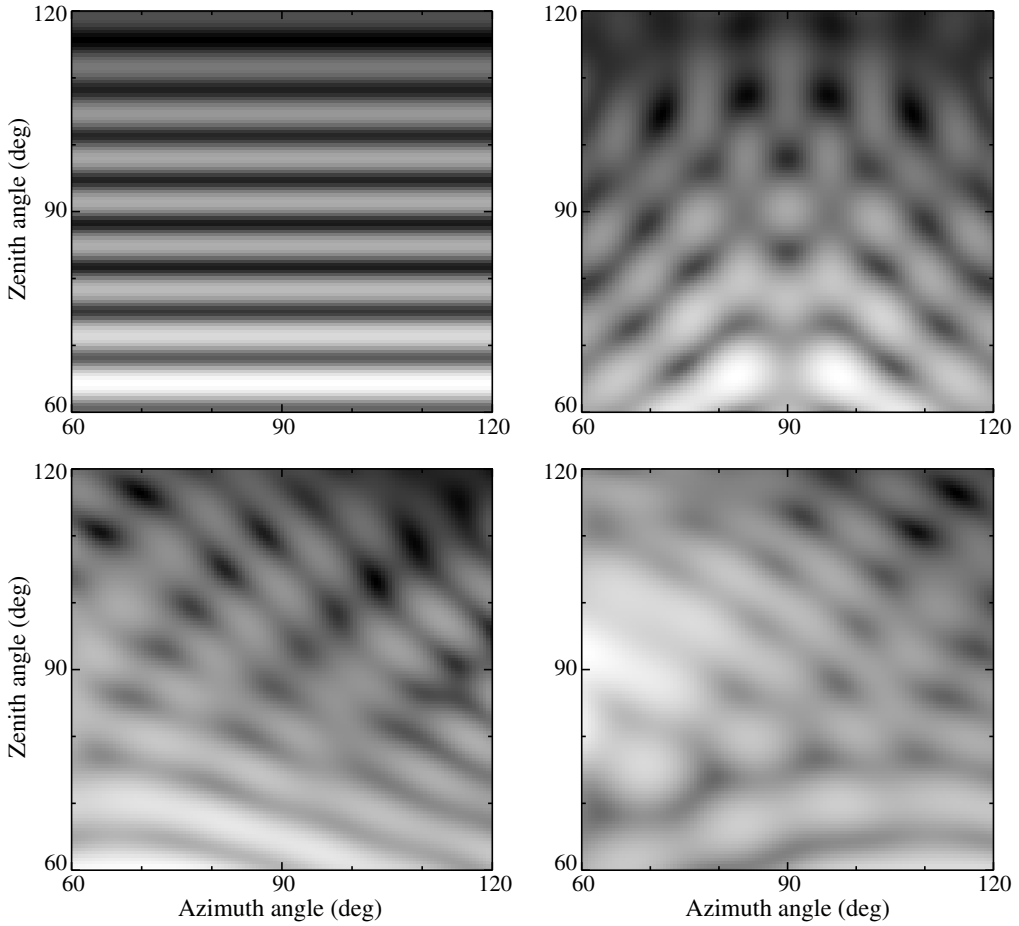

Figure 10.2. Scattered intensity (in arbitrary units) versus $\vartheta^{\rm sca}$ and $\varphi^{\rm sca}$ for a prolate spheroid with an axis ratio $a/b = 1/2$ illuminated by an unpolarized beam of light incident along the *z*-axis of the laboratory reference frame. The surface-equivalent-sphere size parameter of the spheroid is 20 and the relative refractive index is 1.53 + i0.008. The orientation of the spheroid rotation axis relative to the laboratory coordinate system is specified by the Euler angles $\alpha = 0°$, $\beta = 0°$ (upper left panel), $\alpha = 0°$, $\beta = 90°$ (upper right panel), $\alpha = 0°$, $\beta = 45°$ (lower left panel), and $\alpha = 45°$, $\beta = 45°$ (lower right panel).

and resonance structure still evident in Plate 10.1(d). This is demonstrated by Plate 10.2(d), which shows the *T*-matrix results for a modified power law distribution of surface-equivalent-sphere radii, given by Eq. (5.246) with $\alpha = -3$ and $v_{\rm eff} = 0.1$.

The most obvious reason for performing computations and measurements of light scattering by polydisperse rather than monodisperse particles is the desire to represent more closely natural particle ensembles, in which particles are most often distributed over a range of sizes and orientations. The second reason is the presence of the complicated and highly variable interference and resonance structure, which makes it highly problematic to compare computation and/or measurement results for monodisperse particles in a fixed orientation in order to derive useful conclusions about the

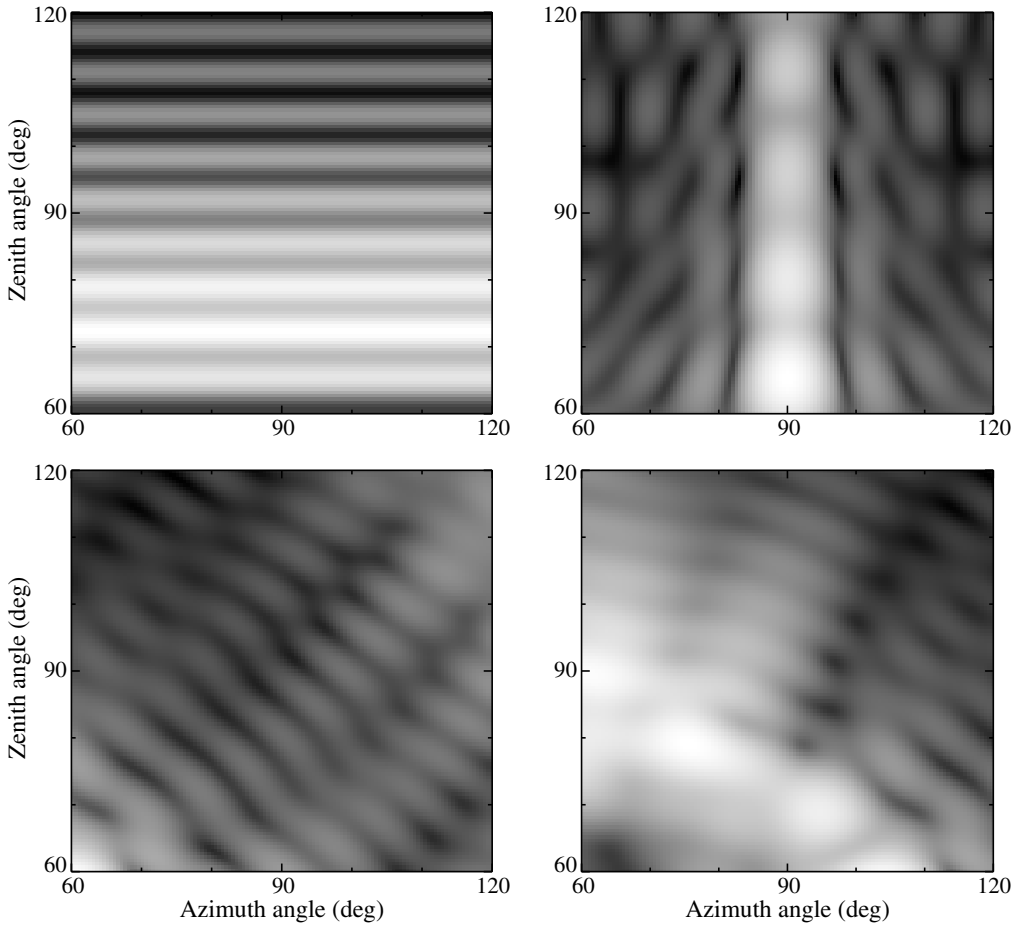

Figure 10.3. As in Fig.10.2, but for a prolate cylinder with a diameter-to-length ratio $1/2$.

specific effects of particle shape on electromagnetic scattering. Averaging over sizes for spheres and averaging over orientations and sizes for nonspherical particles largely removes the interference and resonance structure and enables meaningful comparisons of the scattering properties of different types of particle. Therefore, in the following sections we will mostly analyze polydisperse ensembles of randomly oriented nonspherical particles.

10.2 Randomly oriented, polydisperse spheroids with moderate aspect ratios

There are two reasons to begin our survey by considering spheroidal particles. First, the shape of a spheroid has the advantage of being described by only one shape pa-

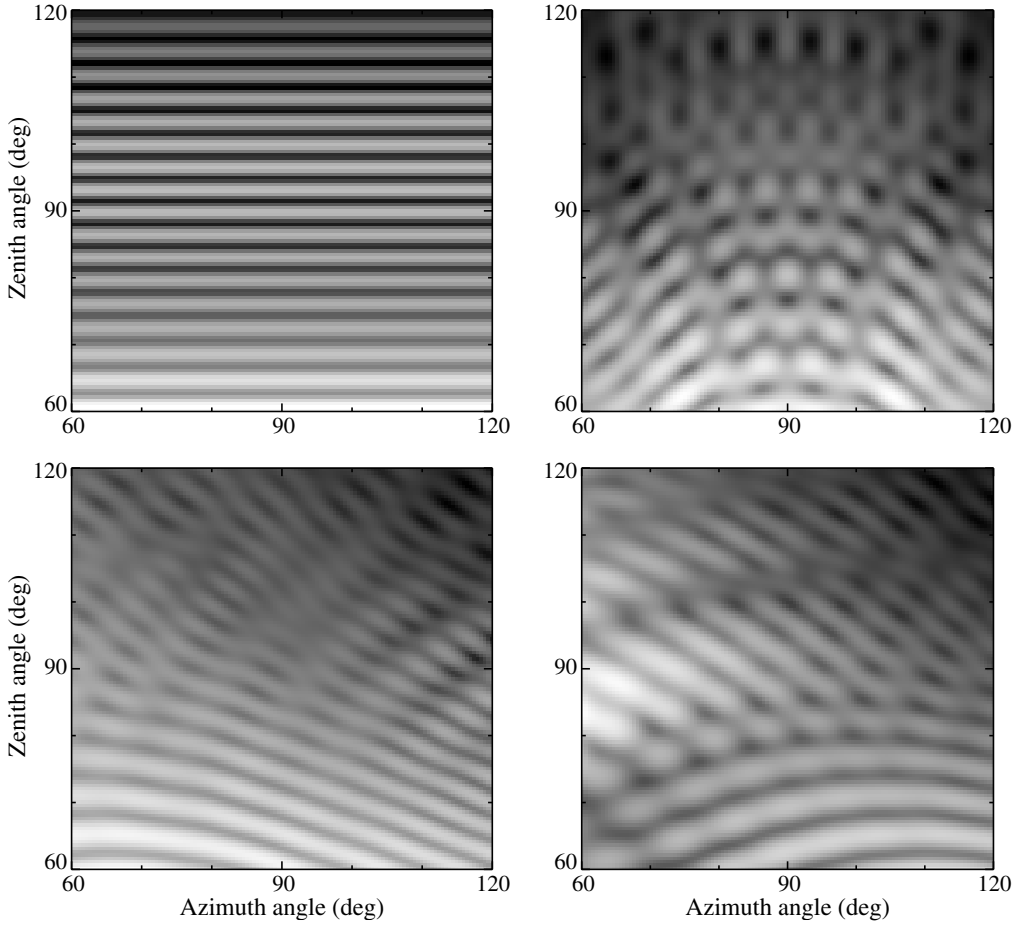

Figure 10.4. As in Fig.10.2, but for spheroid surface-equivalent-sphere size parameter 40.

rameter, specifically, the axis ratio a/b. By varying this single parameter, one can model a continuous sequence of shapes varying from perfect spheres $(a/b = 1)$ and nearly spherical particles $(a/b \sim 1)$ to needles $(a/b \ll 1)$ and plates $(a/b \gg 1)$. Second, spheroids are rotationally symmetric scatterers and, therefore, are especially suitable for efficient *T*-matrix computations (cf. subsection 5.8.3).

The *T*-matrix code described in Section 5.11 provides the option of using several types of size distribution function, given by Eqs. (5.242)–(5.246). As discussed in subsection 5.10.1, the maximum equivalent-sphere radius $r_{\max}$ for the modified gamma, log normal, and gamma size distributions must be increased until the scattering results converge within a prescribed numerical accuracy. This requirement may often necessitate a rather large value of the maximum radius, which can result in quite time-consuming *T*-matrix computations or even failure if the maximum radius is so large relative to the wavelength that the *T*-matrix code does not converge (cf. subsection 5.11.7). However, Hansen and Travis (1974) and Mishchenko and Travis

Table 10.1. Efficiency factors, single-scattering albedo, and asymmetry parameter for log normal, gamma, and modified power law size distributions of randomly oriented oblate spheroids with an axis ratio $a/b = 1.6$[a]

Size distribution	Q_{ext}	Q_{sca}	Q_{abs}	ϖ	$\langle \cos \Theta \rangle$
Log normal	2.35	1.90	0.445	0.810	0.747
Gamma	2.35	1.90	0.445	0.811	0.746
Modified power law	2.37	1.93	0.442	0.813	0.747

[a]All three distributions of surface-equivalent-sphere radii have the same effective radius, $r_{eff} = 1.5\,\mu m$, and effective variance, $v_{eff} = 0.1$. The power exponent of the modified power law size distribution is $\alpha = -3$. The relative refractive index is 1.53 + i0.008, and the wavelength of light in the surrounding medium is 0.6283 μm.

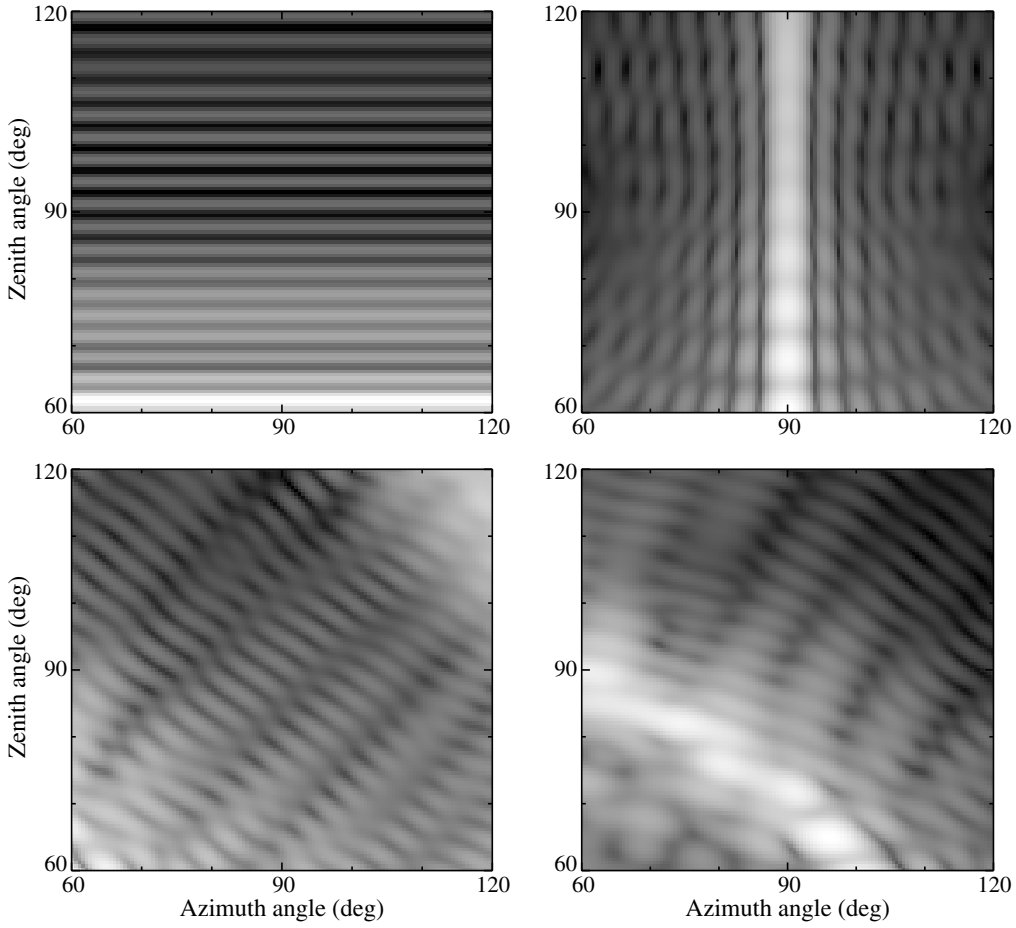

Figure 10.5. As in Fig. 10.3, but for cylinder surface-equivalent-sphere size parameter 40.

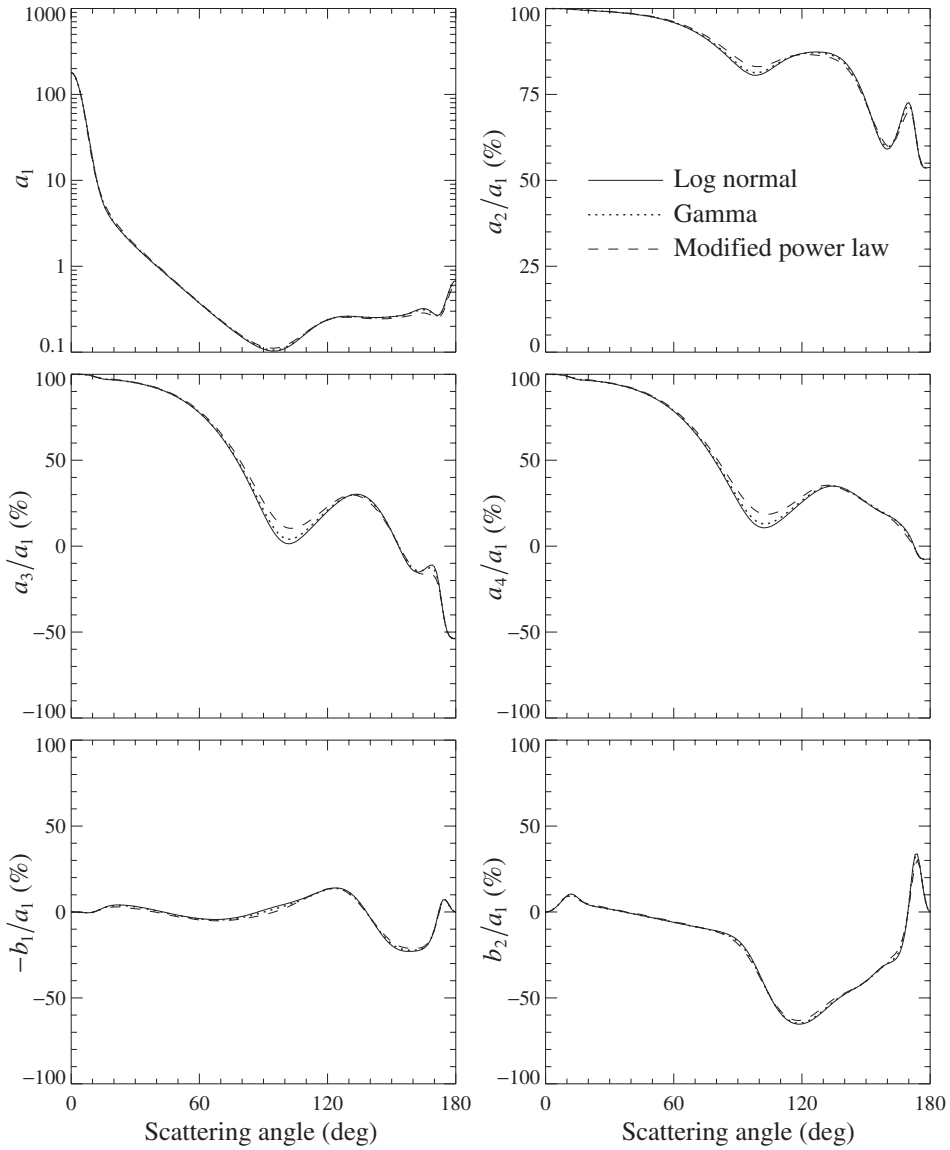

Figure 10.6. Elements of the normalized Stokes scattering matrix for log normal, gamma, and modified power law size distributions of randomly oriented oblate spheroids with an axis ratio $a/b = 1.6$. All three distributions of the surface-equivalent-sphere radii have the same effective radius $r_{\text{eff}} = 1.5\,\mu\text{m}$ and effective variance $v_{\text{eff}} = 0.1$. The power exponent of the modified power law size distribution is $\alpha = -3$. The relative refractive index is 1.53 + i0.008, and the wavelength of light in the surrounding medium is $0.6283\,\mu\text{m}$.

(1994c) showed that, in practice, many plausible size distributions of spherical and nonspherical particles can be adequately represented by just two parameters, viz., the effective radius and the effective variance, defined by Eqs. (5.248) and (5.249), respectively. This means that different size distributions that have the same values of r_{eff} and v_{eff} can be expected to have similar *dimensionless* scattering and absorption characteristics, as illustrated by Table 10.1 and Fig. 10.6. In this regard, the power

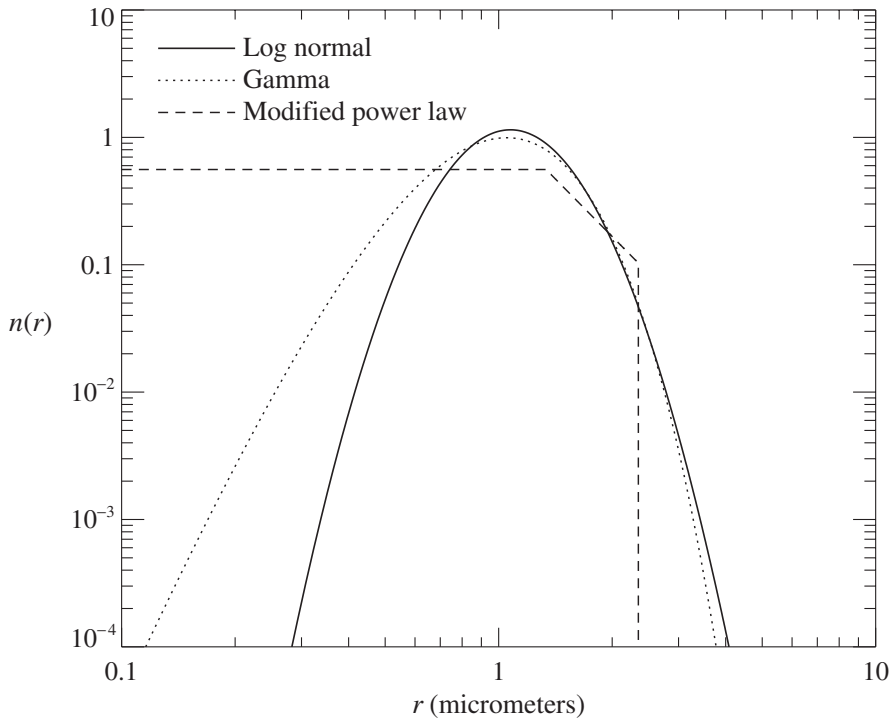

Figure 10.7. Log normal, gamma, and modified power law size distributions with $r_{\text{eff}} = 1.5\,\mu\text{m}$ and $v_{\text{eff}} = 0.1$. The power exponent of the modified power law size distribution is $\alpha = -3$.

and modified power law size distributions given by Eqs. (5.244) and (5.246) have the important practical advantage that their respective maximal radii $r_{\max} = r_2$ are finite by definition and can be significantly smaller than the corresponding convergent radii of the modified gamma, log normal, and gamma distributions with the same r_{eff} and v_{eff} (Fig. 10.7). Furthermore, the absence of a sharp cut-off at $r = r_1$ makes the scattering patterns generated by the modified power law distribution significantly smoother than those produced by the standard power law distribution. Hence, the majority of numerical results discussed in this and the following section have been computed using the modified power law size distribution. We used a fixed power exponent value of $\alpha = -3$ and determined the formal parameters of the size distribution, r_1 and r_2, from the system of equations (5.248), (5.249) for given values of the effective radius and effective variance. It is straightforward to show that for fixed α and v_{eff}, $r_1 = p_1 r_{\text{eff}}$ and $r_2 = p_2 r_{\text{eff}}$, where p_1 and p_2 are constant proportionality factors. The numerical values of these factors for a selection of v_{eff}-values are listed in Table 10.2.

Figures 10.8–10.11 show the phase function versus the scattering angle and the effective size parameter $x_{\text{eff}} = k_1 r_{\text{eff}}$ for polydisperse spheres and polydisperse, randomly oriented, surface-equivalent spheroids with m = 1.53 + i0.008, while the right-hand two columns of Plate 10.2 depict the ratio ρ of the phase function for spheroids

Table 10.2. Factors p_1 and p_2, for the modified power law distribution defined by Eq. (5.246) with $\alpha = -3$, as functions of v_{eff}

v_{eff}	p_1	p_2
0.1	0.89031	1.56538
0.2	0.61383	1.94912
0.4	0.37433	2.52160
1	0.11958	3.91046

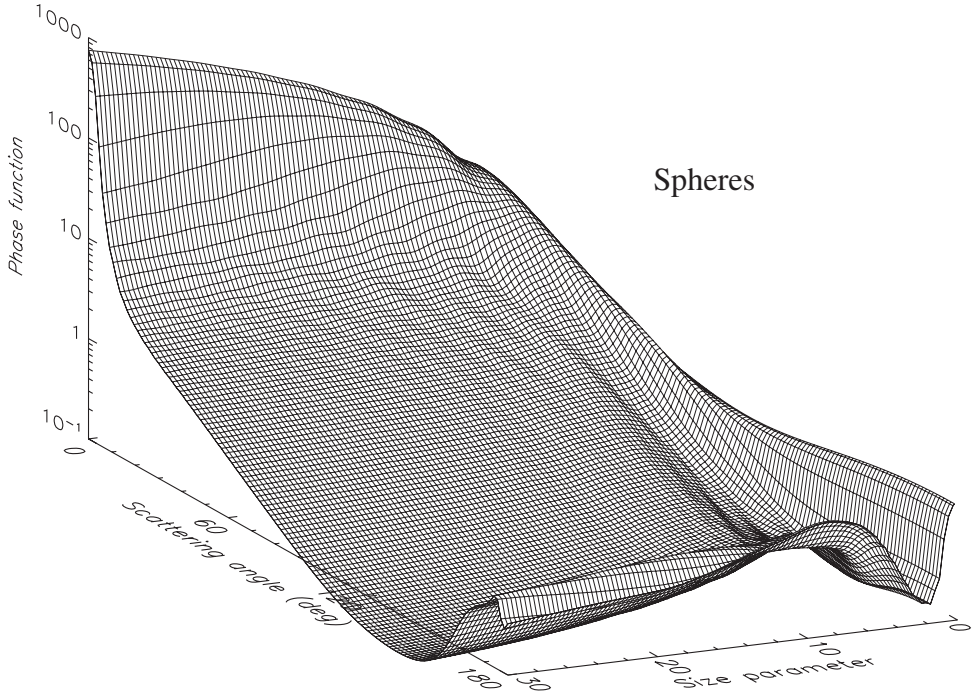

Figure 10.8. Phase function $a_1(\Theta)$ versus scattering angle and effective size parameter for the modified power law distribution of spheres with $\alpha = -3$ and $v_{\text{eff}} = 0.1$. The relative refractive index is 1.53 + i0.008.

to that for spheres. Note that the relative refractive index 1.53 + i0.008 is typical of dust-like and mineral terrestrial aerosols at visible wavelengths (d'Almeida *et al.* 1991). The 121 scattering angle gridlines in Figs. 10.8–10.11 are drawn at 1.5° intervals and correspond to scattering angles $\Theta = 0°, 1.5°, ..., 178.5°$, and 180°, while the 101 size parameter gridlines are drawn at 0.3 intervals and correspond to size parameters x_{eff} = 0, 0.3, …, 29.7, and 30. The residual small-amplitude ripple in Fig. 10.8 is caused by the cut-off at $r = r_2$ in Eq. (5.246) and is almost completely eliminated by averaging over spheroid orientations (Figs. 10.9–10.11).

It can be seen clearly that, excluding the region of Rayleigh scattering, five distinct ρ-value regions exist. In order of increasing scattering angle for both prolate and oblate spheroids they are:

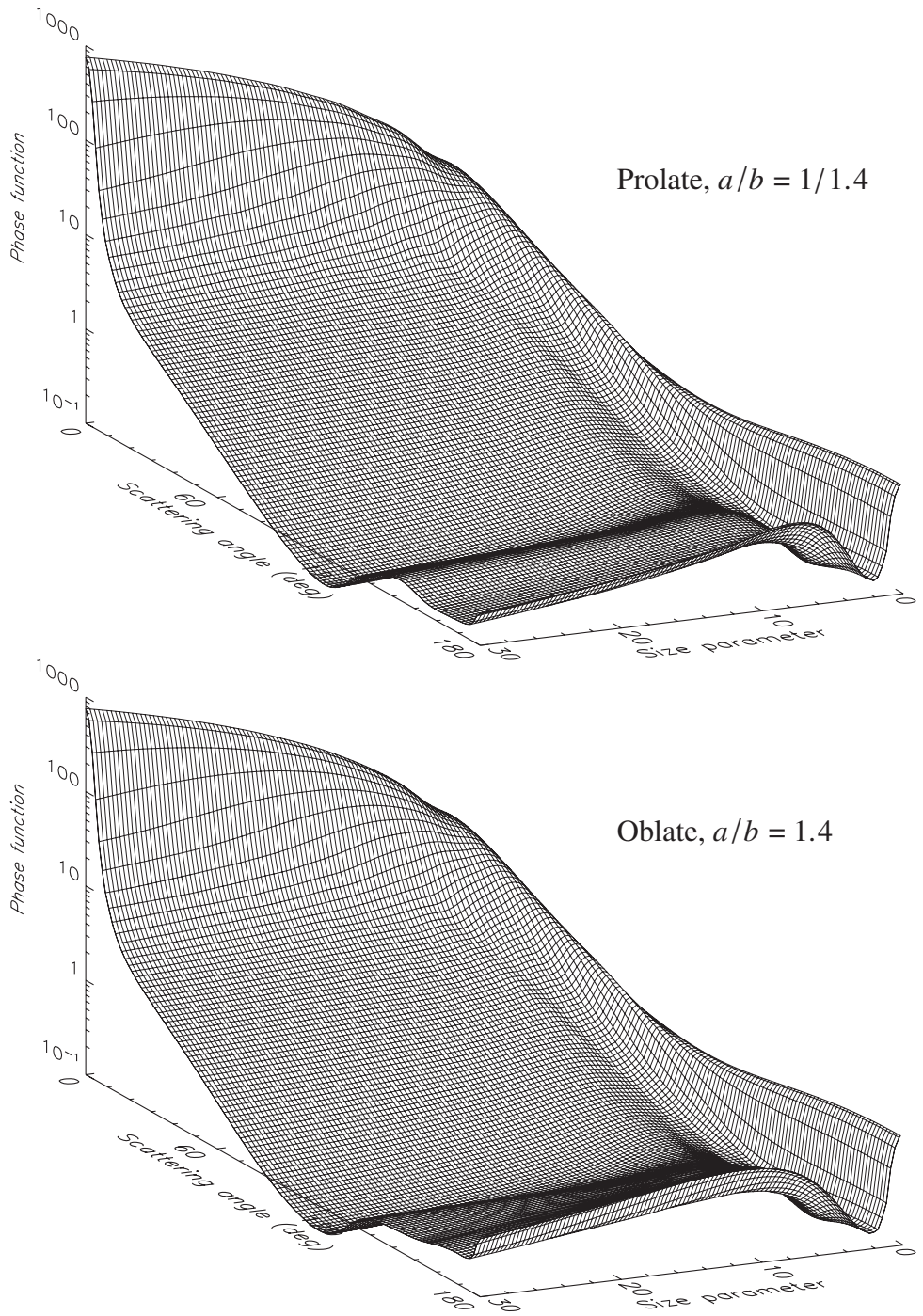

Figure 10.9. As in Fig. 10.8, but for surface-equivalent, randomly oriented prolate and oblate spheroids with aspect ratio 1.4.

(1) nonsphere $\approx$ sphere, i.e., $\rho \approx 1$; (2) nonsphere > sphere, i.e., $\rho > 1$;
(3) nonsphere < sphere, i.e., $\rho < 1$; (4) nonsphere $\gg$ sphere, i.e., $\rho \gg 1$; (10.1)
(5) nonsphere $\ll$ sphere i.e., $\rho \ll 1$.

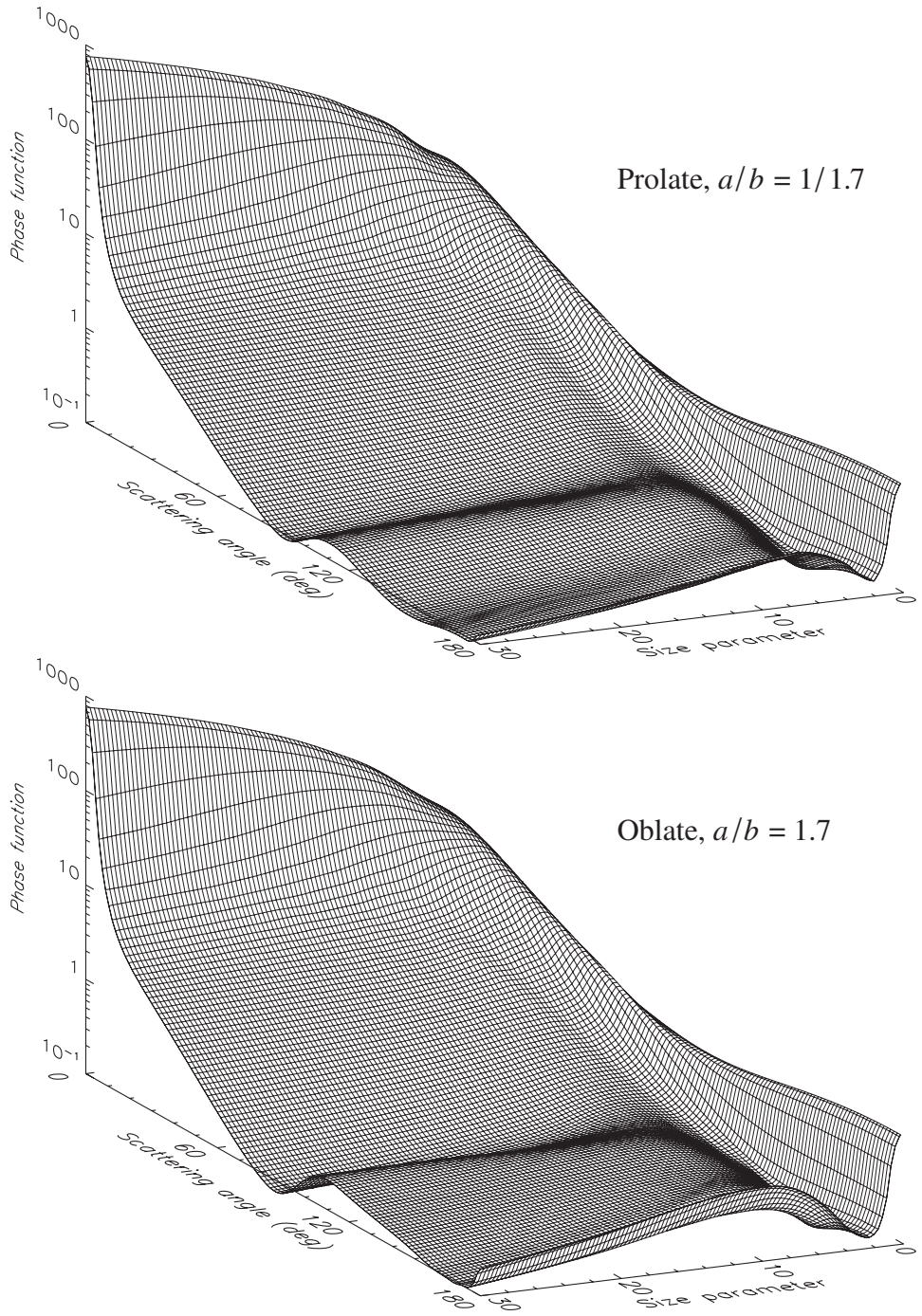

Figure 10.10. As in Fig. 10.8, but for surface-equivalent, randomly oriented prolate and oblate spheroids with aspect ratio 1.7.

The first of these regions is the region of nearly direct forward scattering. It is the region least sensitive to particle nonsphericity, because of the dominance of the diffraction contribution to the phase function; the latter is determined by the average area of the particle geometrical cross section (Section 7.4), which is the same for

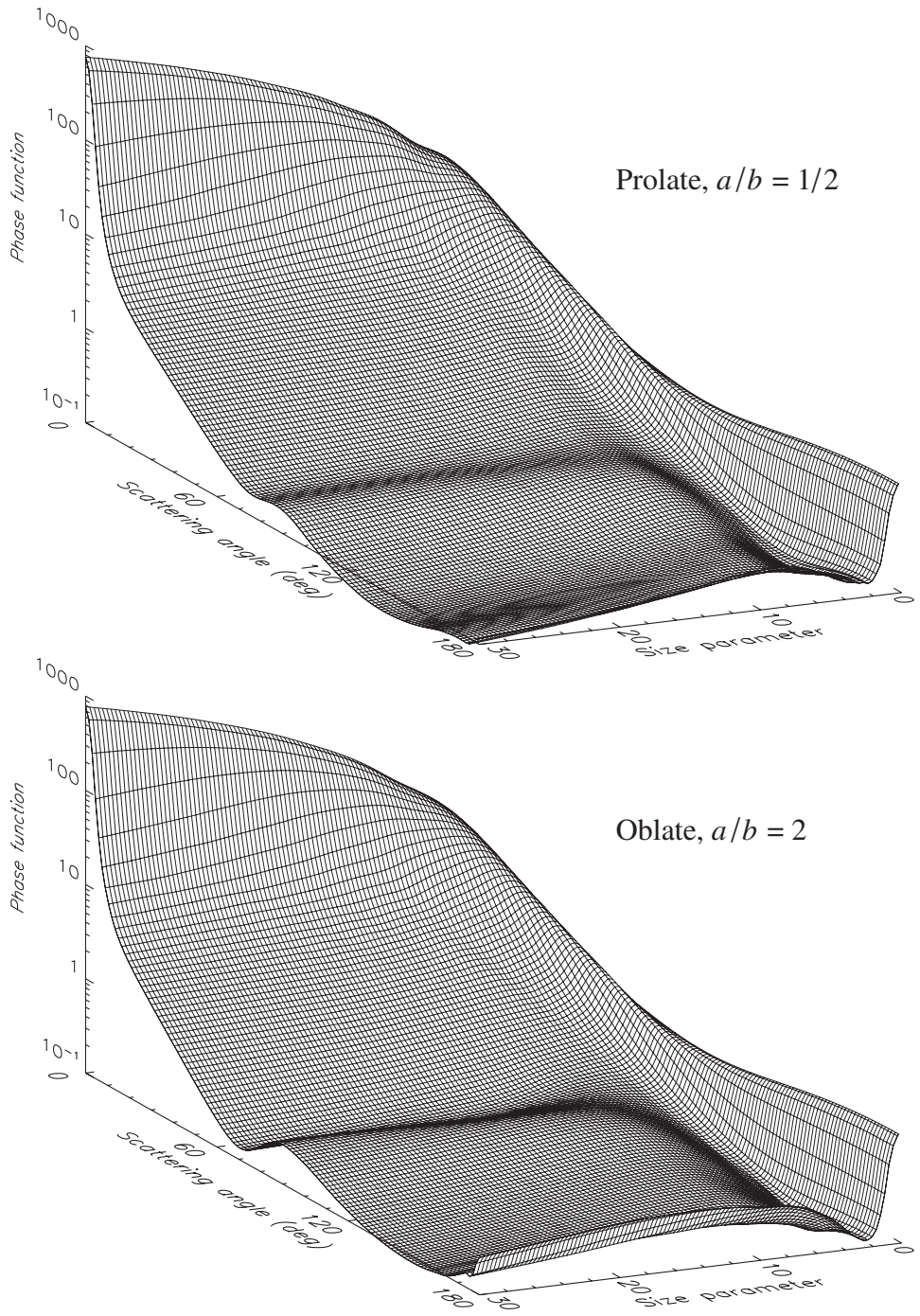

Figure 10.11. As in Fig. 10.8, but for surface-equivalent, randomly oriented prolate and oblate spheroids with aspect ratio 2.

surface-equivalent convex particles such as spheres and spheroids (Vouk 1948). The second region, $\rho > 1$, extends from about 5° to 30° and becomes more pronounced with increasing spheroid aspect ratio ε (i.e., the ratio of the larger to the smaller spheroid axes). Depending on aspect ratio, region 3, $\rho < 1$, extends from about 30° –

35° to 80°–110° and becomes narrower with increasing ε. In this region nonspherical–spherical differences are greater for oblate than for prolate spheroids with the same value of ε; the differences increase with increasing ε.

Region 4 extends from about 80°–110° to 150°–160° and is wider for particles with larger aspect ratios. In this region ρ can well exceed 4, indicating strongly enhanced side scattering as opposed to the deep and wide side-scattering minimum that is found for spherical particles (cf. Figs. 10.8–10.11). Both the left-hand boundary of this region and the position of maximum ρ-values shift towards smaller scattering angles with increasing ε. Interestingly, for prolate spheroids the maximum ρ-values are greater for the moderate aspect ratio 1.4 than for the larger aspect ratios 1.7 and 2.

In region 5, ρ can fall to values below 0.25, which means that another major effect of nonsphericity is to suppress the strong rainbow and glory features seen in calculations for surface-equivalent spheres (cf. Fig. 10.8). However, the backscattering enhancement traditionally associated with the glory survives as a rise of the backscattered intensity at 180° relative to that at 170°. Furthermore, as evident from Figs. 10.8 and 10.9, oblate spheroids with aspect ratio 1.4 can have even greater phase-function values at $\Theta = 180°$ than surface-equivalent spheres, thereby producing ρ-values exceeding unity and causing an exception to the region-5 criterion $\rho \ll 1$. The top two panels of Fig. 10.12 also show that for most size parameters oblate spheroids have larger backscattering phase function values than prolate spheroids with the same aspect ratio and that the ratio of the nonspherical to spherical phase functions at $\Theta = 180°$ has a distinct minimum at effective-size-parameter values 6–9. Also worth noting is that, for prolate spheroids, region 5 becomes more pronounced with increasing ε whereas for oblate spheroids ρ can be smaller for ε = 1.7 than for ε = 2, at larger effective-size-parameter values.

A comparison of the polydisperse polarization diagrams for randomly oriented spheroids and for spheres (cf. the two columns on the left of Plate 10.2 and the top middle panel of Plate 10.6) reveals that, at scattering angles larger than 60°, the degree of linear polarization for unpolarized incident light, $-b_1/a_1$, is strongly ε-dependent, the spherical–nonspherical differences becoming more pronounced with increasing ε; this indicates that the Lorenz–Mie theory is an inappropriate approximation for nonspherical particles in that region. However, at scattering angles less than 60° the linear polarization is weakly dependent on particle shape, thereby suggesting that polarization measurements at near-forward-scattering angles coupled with Lorenz–Mie computations are potentially useful for sizing nonspherical particles. In general, the polarization generated by spheroids is more neutral than that for spheres and shows less variability with size parameter and scattering angle. It is interesting, however, that the Rayleigh region extends to larger size parameters with increasing aspect ratio. The most prominent polarization feature for spheroids is the bridge of positive polarization near 120°, which extends from the region of Rayleigh scattering and separates two regions of negative or neutral polarization at small and large scattering angles. This bridge is absent for spherical particles and near-spherical

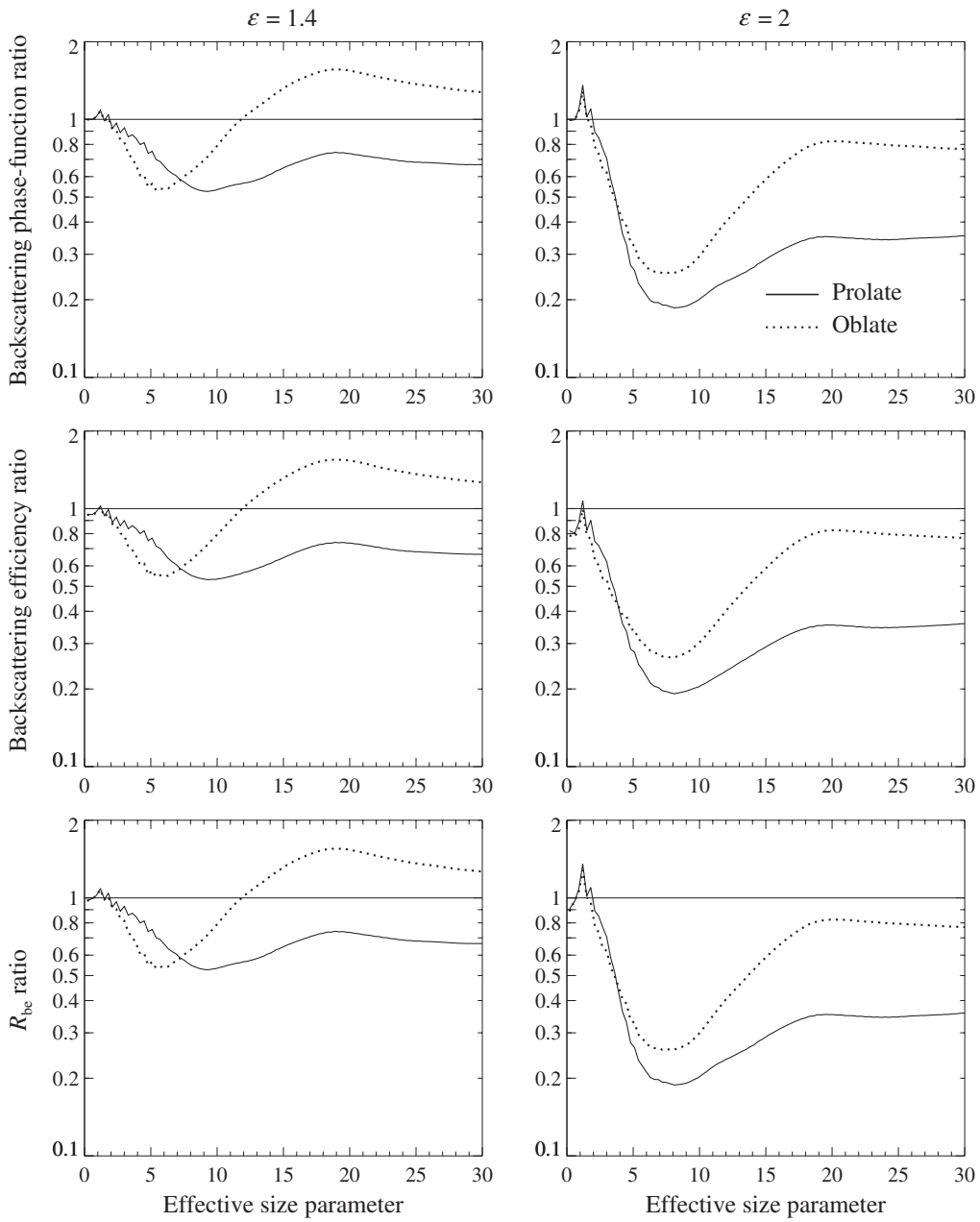

Figure 10.12. Top two panels: ratio of the phase function at $\Theta = 180°$ for randomly oriented polydisperse spheroids with aspect ratios of 1.4 and 2 to that for surface-equivalent spheres, versus effective size parameter. Middle two panels: as in the top panels, but for the ratio of the respective backscattering efficiency factors. Bottom two panels: as in the top panels, but for the ratio of the respective R_{be}-values. Curves are shown for prolate and for oblate spheroids.

spheroids, but develops fully for spheroids with ε - values greater than 1.6–1.7, being somewhat more pronounced for oblate than for prolate spheroids with the same ε (Mishchenko and Travis 1994b).

Whereas for spherical particles $a_2(\Theta)/a_1(\Theta) \equiv 1$, the two left-hand columns of

Plate 10.3 demonstrate that for spheroids this ratio can significantly deviate from unity, especially at side- and backscattering angles. The angular dependence of a_2/a_1 is quite different for prolate and oblate spheroids with the same ε-value, thereby making this ratio well suited for discriminating between elongated and flattened particles. For prolate spheroids, a_2/a_1 has a pronounced minimum centered at $120°-145°$ which shifts towards smaller scattering angles as ε increases. Another minimum occurs at backscattering angles and, surprisingly, is deeper for the less aspherical spheroids, with $\varepsilon = 1.4$, than for the spheroids with $\varepsilon = 1.7$ and 2. Oblate spheroids exhibit a shallow minimum at around $150°-170°$, which becomes more pronounced for particles with $\varepsilon = 2$, and another minimum at exactly the backscattering direction, $\Theta = 180°$, which exhibits a complicated dependence on ε. Also, oblate spheroids with $\varepsilon = 1.4$ show a shallow minimum at about $100°-110°$, which disappears with increasing ε. For both prolate and oblate spheroids, the ratio a_2/a_1 at scattering angles less than $70°$ and in the region of Rayleigh scattering is close to unity and is essentially insensitive to particle size and shape.

For spherical particles the ratio $a_3(\Theta)/a_1(\Theta)$ is identically equal to the ratio $a_4(\Theta)/a_1(\Theta)$; these are shown in the top middle and right-hand panels of Plate 10.5. For spheroids, these two ratios can substantially differ from each other, the ratio a_4/a_1 being larger than a_3/a_1 for most effective size parameters and scattering angles (cf. the two right-hand columns of Plate 10.3 and the two left-hand columns of Plate 10.4). For spheres, the ratio a_3/a_1, and thus a_4/a_1 also, has two negative regions at side- and backscattering angles, separated by a narrow positive branch. With increasing ε, the side-scattering negative region shifts towards smaller scattering angles, weakens in magnitude, and ultimately disappears, while the backscattering negative region becomes wider, especially for prolate spheroids. The backscattering region of negative a_3/a_1 values is wider and deeper than that for a_4/a_1. Unlike the ratio a_3/a_1, the ratio a_4/a_1 can become positive at backscattering angles. Both a_3/a_1 and a_4/a_1 are rather strongly size- and ε-dependent and thus can be sensitive indicators of particle size and shape. In particular, the regions of negative a_3/a_1 and a_4/a_1 are wider and deeper for prolate than for oblate spheroids with the same ε-value. The size-parameter dependence of the ratio a_4/a_1 at backscattering angles is also rather different for prolate and oblate spheroids with the same ε-value.

The right-hand top panel of Plate 10.6 and the two right-hand columns of Plate 10.4 show that the general pattern of the sign of the ratio $b_2(\Theta)/a_1(\Theta)$ is the same for spheres and spheroids, with a broad side-scattering region of negative values separating two positive branches at small and large scattering angles. The forward-scattering region is especially aspect-ratio independent, which renders possible the use of the Lorenz–Mie theory at small scattering angles for sizing nonspherical particles. However, large variations in magnitude of the ratio b_2/a_1 with particle shape at side- and backscattering angles make it sensitive to particle nonsphericity and appreciably different for prolate and oblate spheroids of the same aspect ratio. In particular, with increasing ε the region of smallest b_2/a_1 values becomes more shallow and shifts

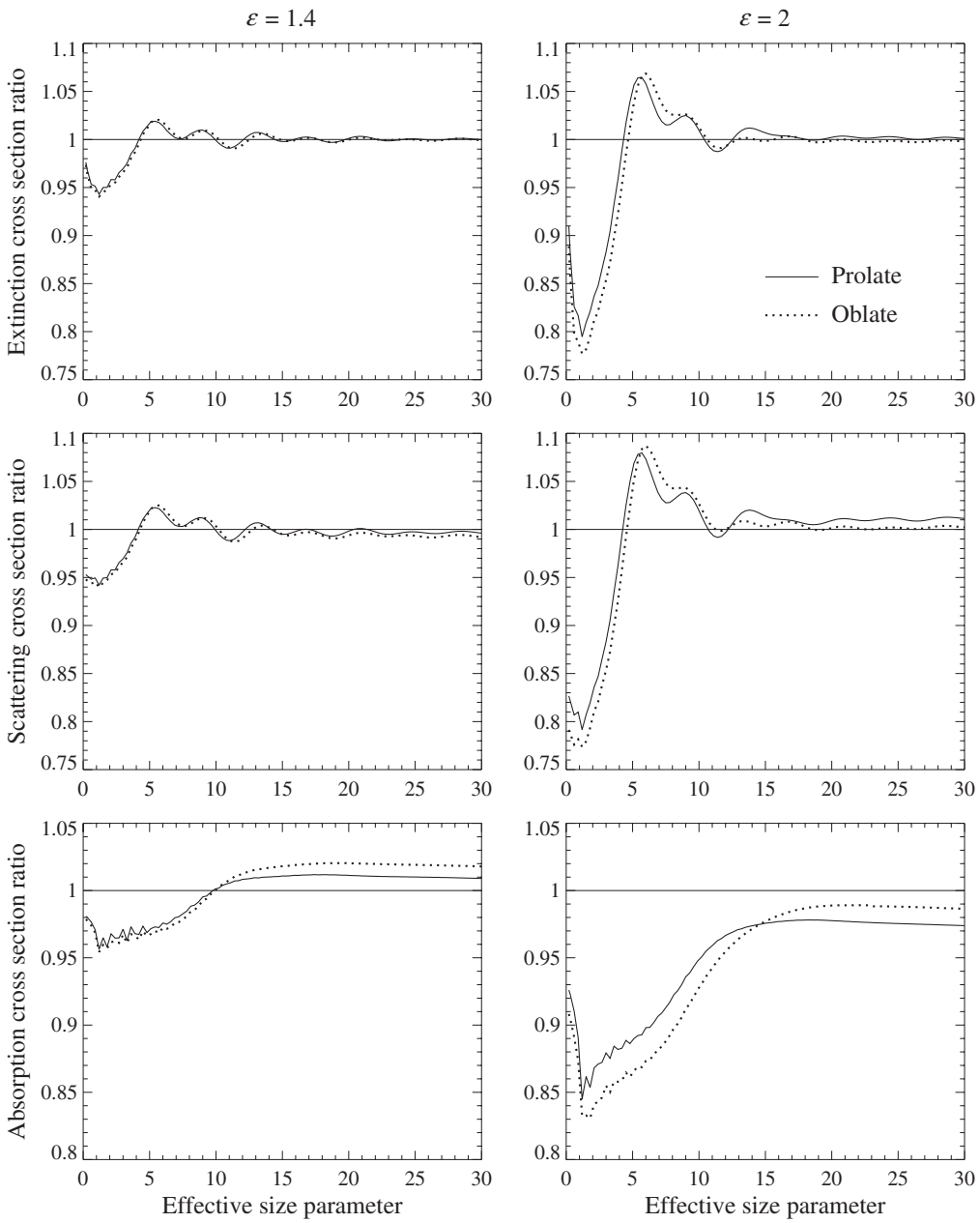

Figure 10.13. Top two panels: ratio of the extinction cross section for randomly oriented polydisperse spheroids with aspect ratios of 1.4 and 2 to that for surface-equivalent spheres, versus effective size parameter. Middle two panels: as in the top panels, but for the ratio of the respective scattering cross sections. Bottom two panels: as in the top panels, but for the ratio of the respective absorption cross sections. Curves are shown for prolate and for oblate spheroids.

towards smaller scattering angles, while the backscattering positive branch becomes less developed. The region of negative values is more shallow and the backscattering positive branch is much weaker for prolate than for oblate spheroids. In general, the differences between prolate spheroids and spheres are larger than those between ob-

late spheroids and spheres.

Unlike the elements of the scattering matrix, the integral photometric characteristics (the extinction, scattering, and absorption cross sections, the single-scattering albedo, and the asymmetry parameter) are much less dependent on particle shape, as Figs. 10.13 and 10.14 demonstrate. In most cases the nonspherical–spherical differences tend to decrease with increasing effective size parameter. For the optical cross sections and the single-scattering albedo, the differences are maximal at effective size parameters smaller than 5. The asymptotic geometrical optics limit, unity, for the extinction cross section ratio (cf. Section 7.4) is reached at relatively small size parameters of about 15. The nonspherical–spherical differences are especially small for the single-scattering albedo at size parameters exceeding unity. The curves for prolate and oblate spheroids with the same aspect ratio are very close to one another except for the asymmetry parameter, in which case the differences between the curves for prolate and oblate spheroids can be much larger than the differences between those for prolate spheroids and for spheres.

As discussed in Section 9.5, important backscattering characteristics widely used in radar and lidar applications are the backscattering efficiency factor $Q_{\rm b}$, defined by Eqs. (9.10) and (9.14), and the backscatter-to-extinction ratio $R_{\rm be}$, defined by Eq. (9.13). The four lower diagrams of Fig. 10.12 depict the ratios of these backscattering characteristics for randomly oriented polydisperse prolate and oblate spheroids to those for surface-equivalent spheres. Not surprisingly, these ratios differ from the backscattering-phase-function ratio (see the top two diagrams of Fig. 10.12) only at small size parameters, where the ratio of the scattering cross sections and the ratio of the single-scattering albedos for nonspherical and surface-equivalent spherical particles deviate noticeably from unity. It is seen that nonspherical–spherical differences in the backscattering efficiency factor and the backscatter-to-extinction ratio are quite significant, thus suggesting that shape effects should be explicitly taken into account in analyzing backscattering measurements for nonspherical particles. In general, spheroids are weaker backscatterers than surface-equivalent spheres, especially at size parameters from about 5 to 15. However, as we noted above, the curves for oblate spheroids with aspect ratio 1.4 illustrate that suppressed scattering at $\Theta = 180^\circ$ is not a universal optical characteristic of nonspherical particles.

Two quantities that are traditionally considered unequivocal indicators of particle nonsphericity are the linear and circular backscattering depolarization ratios, $\delta_{\rm L}$ and $\delta_{\rm C}$, defined as

$$\delta_{\rm L} = \frac{a_1(180^\circ) - a_2(180^\circ)}{a_1(180^\circ) + a_2(180^\circ)} \geq 0, \tag{10.2}$$

$$\delta_{\rm C} = \frac{a_1(180^\circ) + a_4(180^\circ)}{a_1(180^\circ) - a_4(180^\circ)} \geq 0 \tag{10.3}$$

(see Eqs. (4.55) and (4.56)). For macroscopically isotropic and mirror-symmetric media these ratios are not independent, because Eq. (4.63) yields

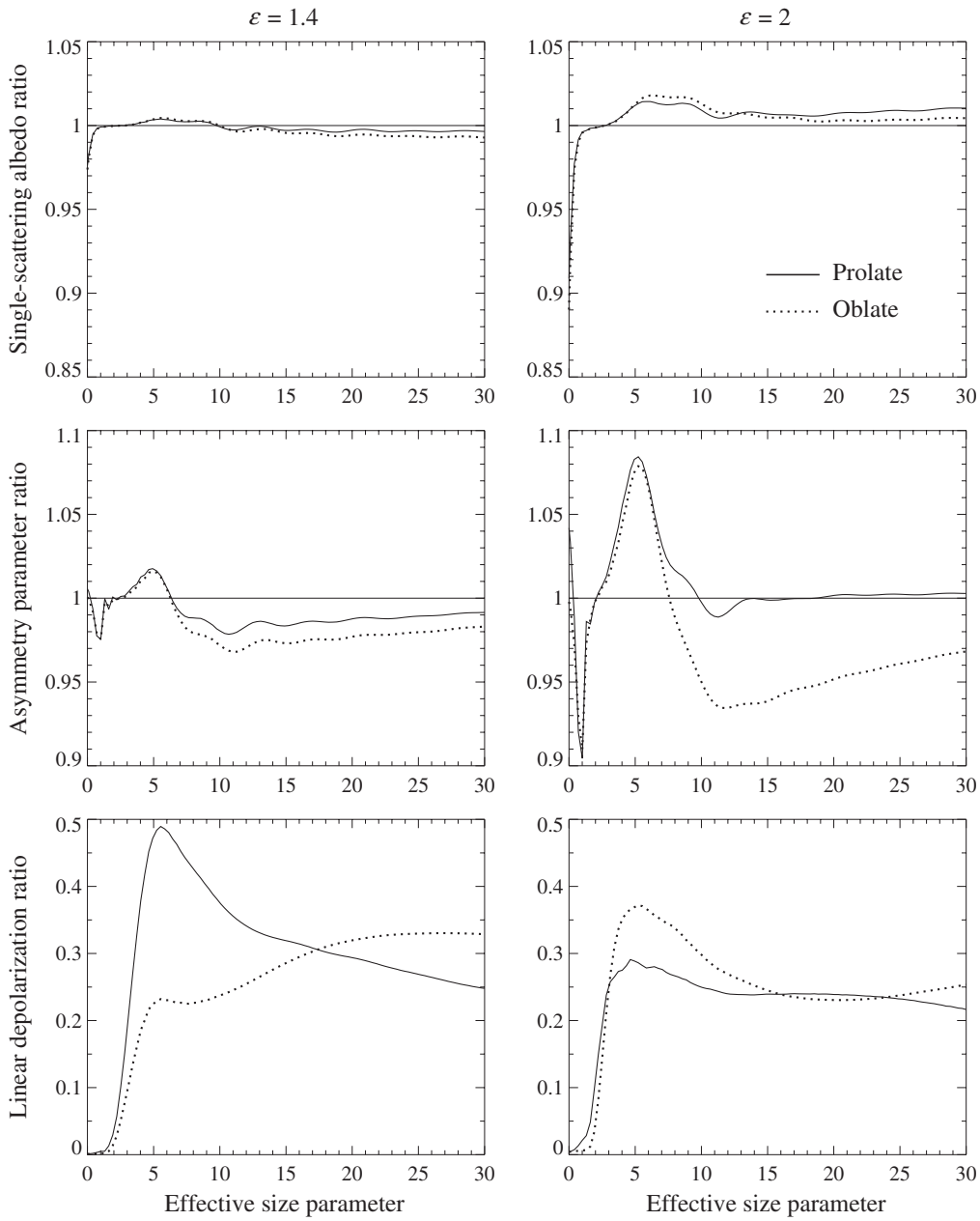

Figure 10.14. Top two panels: ratio of the single-scattering albedo for randomly oriented polydisperse spheroids with aspect ratios of 1.4 and 2 to that for surface-equivalent spheres, versus effective size parameter. Middle two panels: as in the top panels, but for the ratio of the respective asymmetry parameters. Bottom two panels: linear backscattering depolarization ratio for randomly oriented polydisperse spheroids with aspect ratios of 1.4 and 2 versus effective size parameter. Curves are shown for prolate and for oblate spheroids.

$$\delta_{\rm C} = \frac{2\delta_{\rm L}}{1-\delta_{\rm L}} \tag{10.4}$$

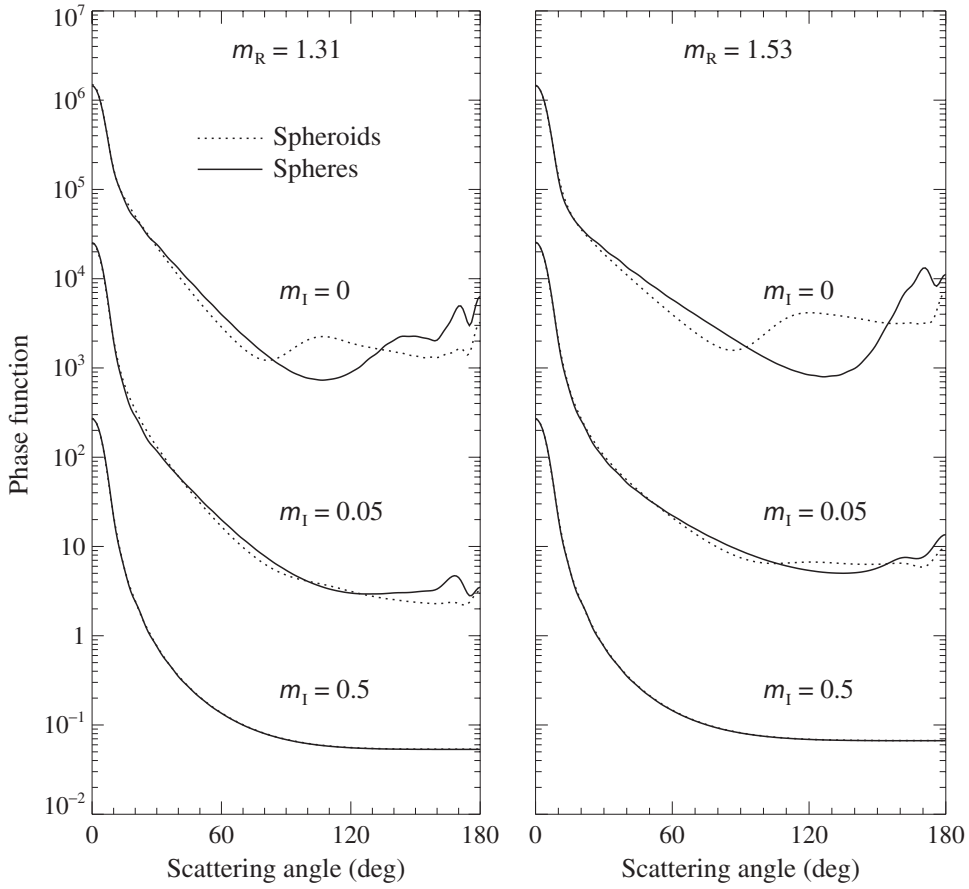

Figure 10.15. Phase function a_1 versus scattering angle Θ for polydisperse, randomly oriented oblate spheroids with an axis ratio 1.7 and for surface-equivalent spheres. The results are shown for two values of the real part of the relative refractive index ($m_R = 1.31$ and 1.53) and three values of the imaginary part ($m_I = 0$, 0.05, and 0.5). The size distribution is given by Eq. (5.246) with $\alpha = -3$ and $v_{eff} = 0.1$. The effective size parameter is $x_{eff} = 15$. The vertical axis scale applies to the curves with $m_I = 0.5$, the other curves being successively displaced upward by a factor of 100.

(Mishchenko and Hovenier 1995). For spheres, both ratios vanish since $a_2(180°) = a_1(180°)$ and $a_4(180°) = -a_1(180°)$ (see Eqs. (4.65) and (4.66)). For nonspherical particles these equalities do not generally hold, thus causing non-zero backscattering depolarization ratios. The bottom two diagrams in Fig. 10.14 show the linear depolarization ratio computed for randomly oriented polydisperse spheroids. It is seen that for both prolate and oblate spheroids δ_L can deviate substantially from zero, thus illustrating its use as an indicator of nonsphericity. However, the depolarization ratios cannot be considered an unambiguous measure of the degree of the departure of the particle shape from that of a sphere. Indeed, for prolate spheroids with $\varepsilon = 1.4$ the maximal δ_L-value is significantly larger than that for $\varepsilon = 2$. We will see later that even larger δ_L-values can be produced by spheroids with aspect ratios as small as 1.05.

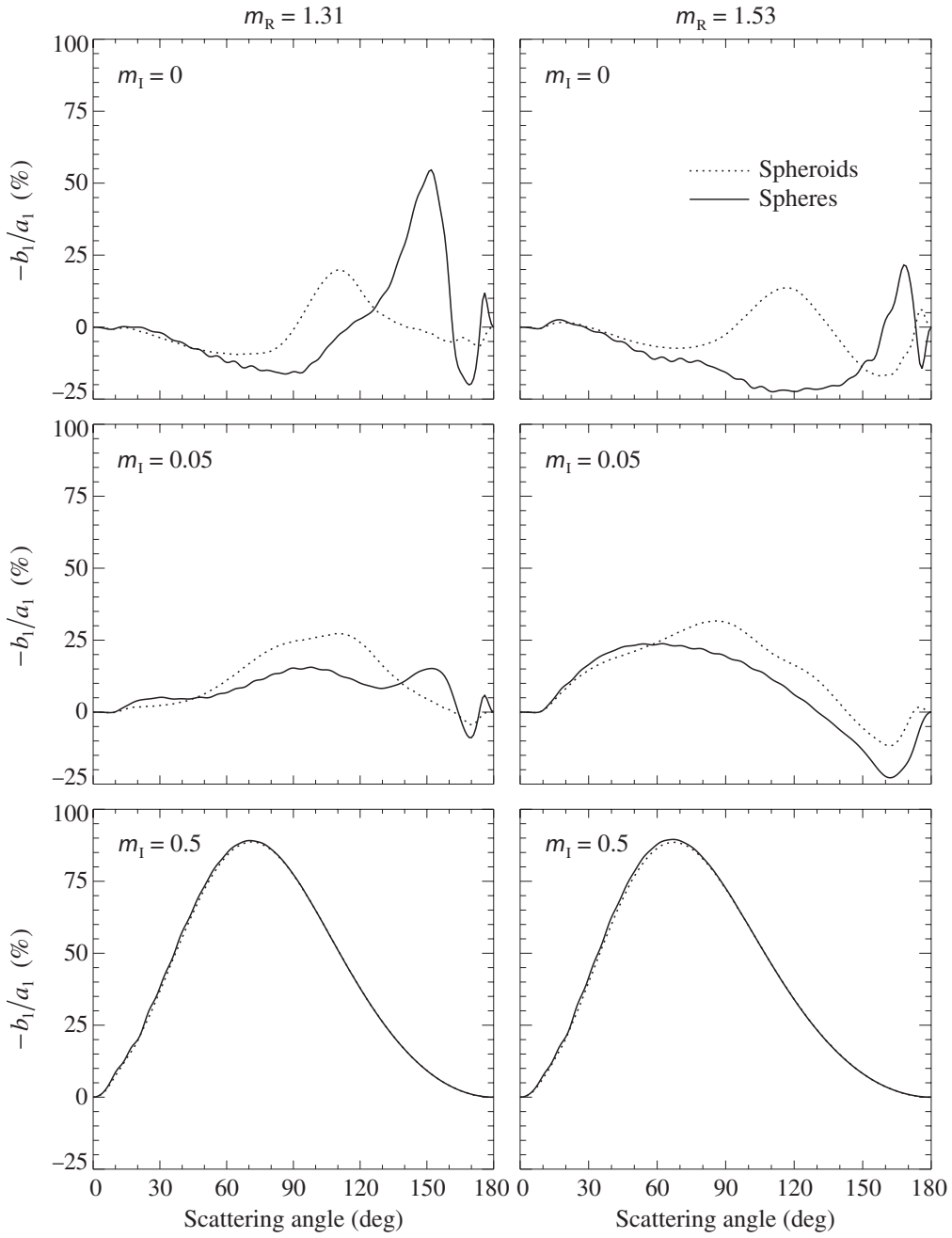

Figure 10.16. As in Fig. 10.15, but for the ratio $-b_1/a_1$.

Figures 10.15 and 10.16 show that with increasing imaginary part of the relative refractive index, nonspherical–spherical differences weaken and ultimately disappear (Mishchenko and Travis 1994b; Mishchenko *et al.* 1997a). For these particle distributions with effective size parameter of $x_{\text{eff}} = 15$, the scattering patterns with $m_I = 0.5$ are dominated by diffraction and external reflections and are essentially the same for spheres and surface-equivalent randomly oriented spheroids. This example

illustrates the general theorem formulated by van de Hulst (1957, Section 8.42): the scattering pattern caused by external reflection from very large convex particles with random orientation is identical to that caused by external reflection from a very large sphere composed of the same material.

10.3 Randomly oriented, polydisperse circular cylinders with moderate aspect ratios

Another class of rotationally symmetric nonspherical particles that can be efficiently studied using the *T*-matrix method are finite circular cylinders. Unlike spheroids, the surface of finite cylinders is not completely smooth but, rather, is characterized by sharp, rectangular edges. These edges make cylinders less regular nonspherical particles than spheroids and might well be expected to have an effect on the scattering and absorption characteristics (Kuik *et al.* 1994; Mishchenko *et al.* 1996a).

For spheroids, nonspherical–spherical differences in all scattering and absorption characteristics vanish as the axis ratio becomes unity, since spheroids with axis ratio unity are spherical particles. Circular cylinders with diameter-to-length ratio unity are, however, already nonspherical particles with a shape deviating significantly from that of a sphere (the ratio of the largest to the smallest cylinder dimension equals $2^{1/2} \approx 1.414$). Accordingly, Figs. 10.17–10.21 show that nonspherical–spherical differences in the extinction, scattering, and absorption cross sections, the single-scattering albedo, and the asymmetry parameter between cylinders with $D/L = 1$ and spheres are already significant. Furthermore, the differences in $C_{\rm ext}$, $C_{\rm sca}$, and $\langle \cos\Theta \rangle$ do not necessarily increase with increasing cylinder aspect ratio. In fact, at effective size parameters larger than approximately 7, nonspherical–spherical differences in the extinction and scattering cross sections and in the asymmetry parameter are smaller for prolate cylinders with $D/L = 1/2$ than for more compact cylinders with $D/L = 1,\ 1/1.4,$ and 1.4. However, nonspherical–spherical differences in the absorption cross section and single-scattering albedo do increase with increasing aspect ratio. The absorption cross section systematically decreases with increasing ε, as is the case for spheroids, whereas ϖ and $\langle \cos\Theta \rangle$ increase with increasing ε at effective size parameters larger than 3. The maximum nonspherical–spherical differences in the integral photometric characteristics for cylinders occur at effective size parameters smaller than about 5, which resembles the case for spheroids (cf. Section 10.2). Similarly, at effective size parameters larger than about 10 the differences in the integral photometric characteristics become relatively small. However, the magnitude of the nonspherical–spherical differences for cylinders can be noticeably larger than that for axis-ratio-equivalent spheroids.

The backscattered fraction for isotropically incident radiation, $\overline{\beta}$, is defined as

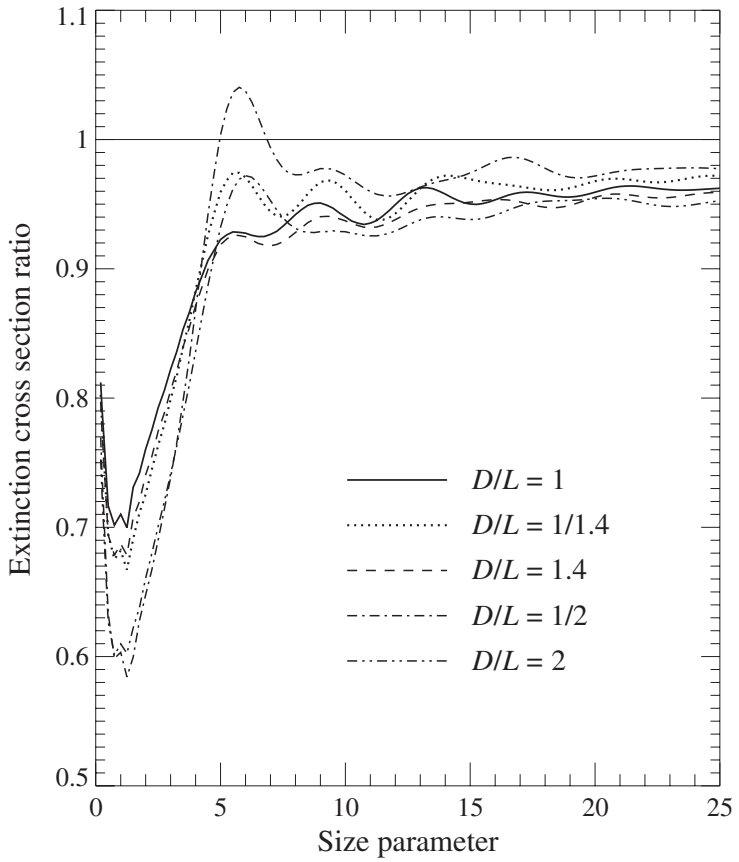

Figure 10.17. Ratio of the extinction cross section for randomly oriented, polydisperse cylinders to that for surface-equivalent spheres, versus effective size parameter; $D/L = 1,\ 1/1.4,\ 1.4,\ 1/2,$ and 2. The distribution of surface-equivalent-sphere radii is given by Eq. (5.246) with $\alpha = -3$ and $v_{\text{eff}} = 0.1$. The relative refractive index is 1.53 + i0.008.

$$\overline{\beta} = \frac{1}{2\pi} \int_0^{\pi} \mathrm{d}\Theta\, a_1(\Theta)\, \Theta \sin\Theta \tag{10.5}$$

(Coakley and Chýlek 1975; Wiscombe and Grams 1976). This quantity enters the two-stream approximation to the scalar radiative transfer equation for plane-parallel media and is sometimes used to estimate experimentally the asymmetry parameter of the phase function (Marshall *et al.* 1995). Figure 10.22 shows the ratio $\overline{\beta}(\text{cylinders})/\overline{\beta}(\text{spheres})$ as a function of x_{eff} and reveals that nonspherical–spherical differences in the backscattered fraction are relatively small. Interestingly, the asymmetry parameter and the backscattered fraction ratios depicted in Figs. 10.21 and 10.22 are approximately mirror images of one another with respect to the horizontal line at the level unity, so that for each size parameter, the larger the asymmetry parameter ratio the smaller the backscattered fraction ratio. This relationship was first found by Mugnai and Wiscombe (1986) in their *T*-matrix computations for randomly oriented Chebyshev particles and then by Mishchenko *et al.* (1997a) in computations

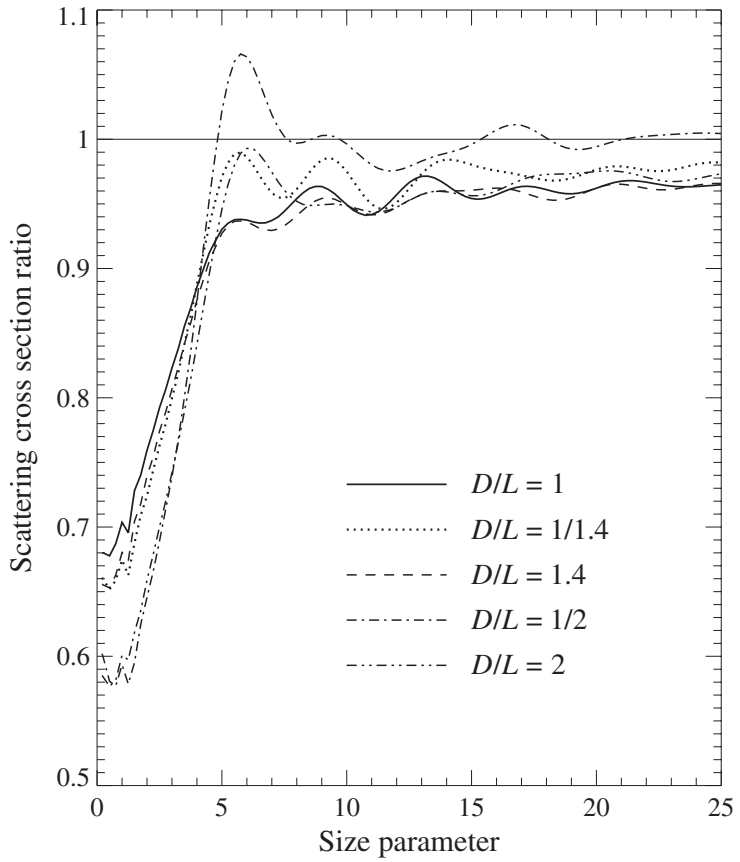

Figure 10.18. As in Fig. 10.17, but for the scattering cross section ratio.

for polydisperse, randomly oriented spheroids.

Plate 10.5 (left-hand column, three lower diagrams) shows that the pattern of the ratio ρ of the phase function for polydisperse, randomly oriented cylinders to that for surface-equivalent spheres, as a function of effective size parameter and scattering angle, strikingly resembles that for spheroids and spheres and shows, for size parameters $\gtrsim 5$, the same five distinct ρ - regions in order of increasing scattering angle (see Eq. (10.1)). The only significant difference between the ρ - patterns for spheroids and cylinders is the noticeably weak dependence of the ρ - pattern for cylinders on the aspect ratio. This means that for cylinders the boundaries of the five regions remain essentially fixed as the diameter-to-length ratio varies; for spheroids, however, the boundaries move substantially with axis ratio.

Region 1, where $\rho \approx 1$, is the region of exact or nearly exact forward scattering, dominated by diffraction. Region 2, where $\rho > 1$, is the region of near-forward scattering and becomes more pronounced with increasing asphericity for both prolate and oblate cylinders, thus resembling the case for spheroids. The third region, where $\rho < 1$, extends from about $20°$ to about $70°$ and is more pronounced for oblate than for prolate cylinders, again in agreement with computations for prolate versus oblate spheroids. Region 4 is the region of side scattering and extends from about $75°$ to

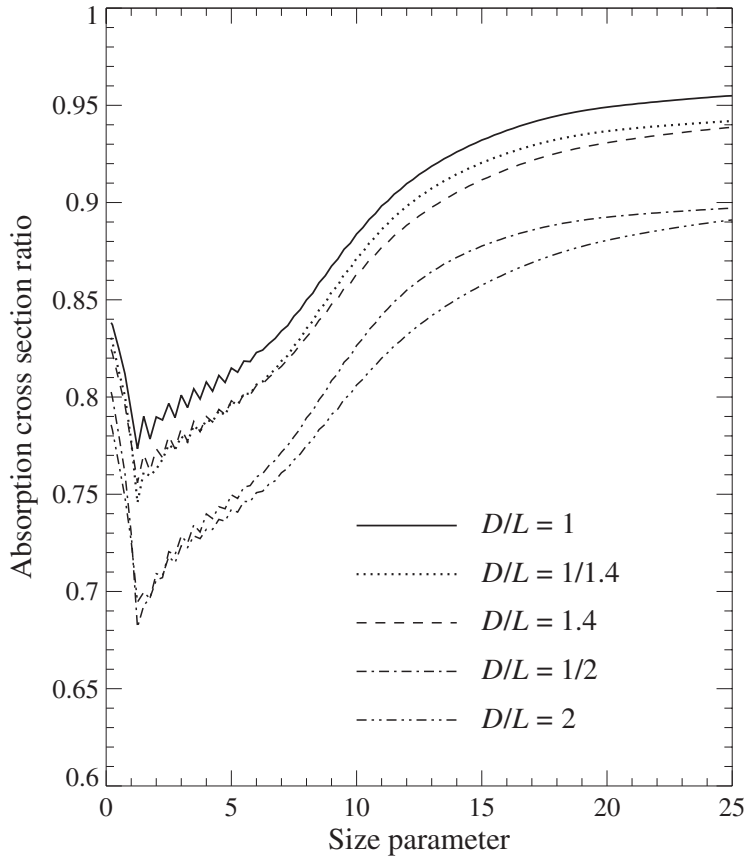

Figure 10.19. As in Fig. 10.17, but for the absorption cross section ratio.

about 155°. Here ρ can exceed 2.5. Although this value is smaller than that for surface-equivalent spheroids, for which ρ can exceed 4, it nonetheless indicates a strongly enhanced side-scattering, as opposed to the wide and deep side-scattering minimum in the phase function for spherical particles (cf. Fig. 10.23). Finally, region 5 is the region of near-backward scattering, where ρ-values as small as 0.3 demonstrate again how nonsphericity can suppress the glory and rainbow features prominent in the phase function for spherical particles. Computations indicate, however, that cylinders with effective size parameters larger than 16 can have larger phase function values at exactly the backscattering direction than surface-equivalent spheres. This is illustrated well in Fig. 10.24, which shows the ratio of the phase function at $\Theta = 180°$ for cylinders to that for surface-equivalent spheres. The only exception among these cases is that of oblate cylinders with a diameter-to-length ratio 2. Since this enhanced scattering at $\Theta = 180°$ for cylinders occurs at relatively larger size parameters, it might be explained using geometrical optics considerations, specifically, in terms of double internal reflections from mutually perpendicular facets (see Section 10.6). We should recall, however, that oblate spheroids with aspect ratios less than about 1.4 and effective size parameters larger than about 12 can also produce greater backscattering phase-function values than surface-equivalent spheres (cf. Plate 10.2(h)).

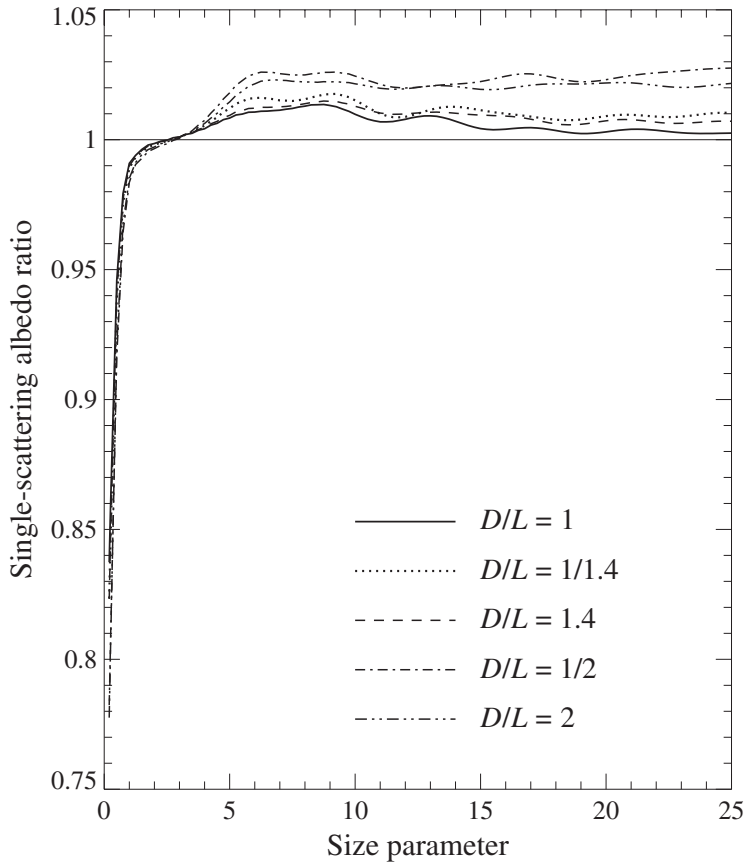

Figure 10.20. As in Fig. 10.17, but for the single-scattering albedo ratio.

Figure 10.25 demonstrates that the backscatter-to-extinction ratio is also strongly shape dependent, so that the ratio $R_{be}(\text{cylinders})/R_{be}(\text{spheres})$ can be either much larger or much smaller than unity. Again, these results as well as those for spheroids strongly suggest that the effect of particle shape should be taken into account explicitly in analyzing radar and lidar measurements for nonspherical particles. As was pointed out in Chapter 8, laboratory measurements of light scattering at exactly the backscattering direction can be rather difficult, thereby enhancing the value of rigorous theoretical computations of nonspherical–spherical differences.

For spheroids with $\varepsilon = 1$, i.e., for spheres, the ratio a_2/a_1 is identically equal to unity. Cylinders with $D/L = 1$ are already nonspherical particles and show a significant deviation of a_2/a_1 from unity (Plate 10.6, left-hand column). For the cylinders with $D/L = 1/2, 1/1.4, 1, 1.4$, and 2 the patterns of the ratio a_2/a_1 as a function of effective size parameter and scattering angle are qualitatively similar, showing side- and back-scattering minima separated by a vertical bridge of larger values centered at around 170°. However, the depths of the minima depend on D/L. The side-scattering minimum is deeper for compact $(D/L = 1)$ and prolate $(D/L < 1)$ cylinders, whereas the depth of the back-scattering minimum increases with increasing aspect ratio. The ratio a_2/a_1 for spheroids also shows a distinct backscattering

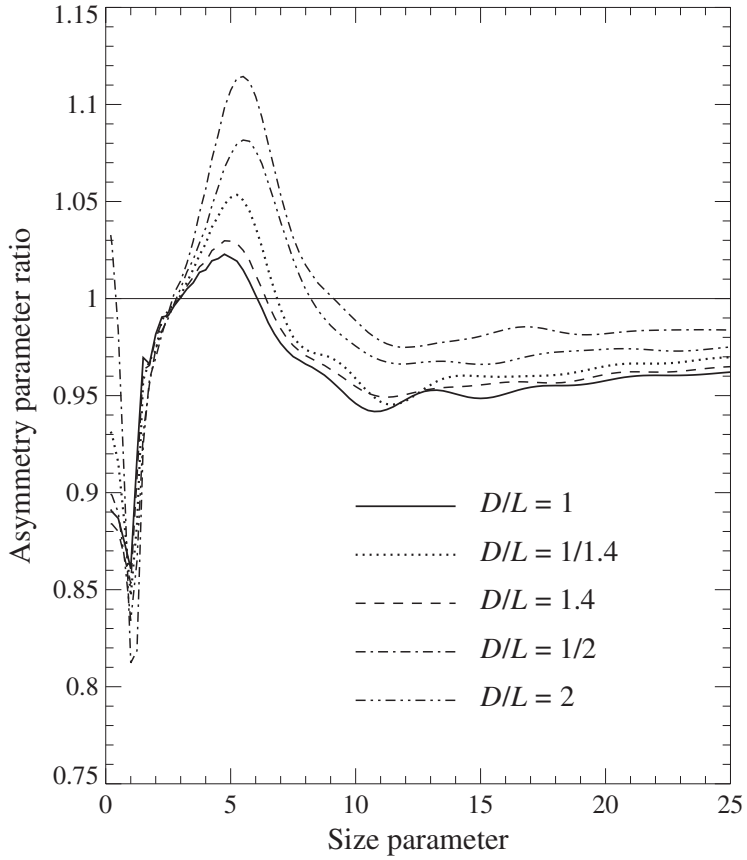

Figure 10.21. As in Fig. 10.17, but for the asymmetry parameter ratio.

minimum. However, unlike the case for cylinders, this minimum becomes significantly deeper as the ε-value for prolate spheroids decreases from 2 to 1.4. As for spheroids, the ratio a_2/a_1 for cylinders is nearly shape independent and close to unity at scattering angles smaller than $90°$ and/or at effective size parameters smaller than 2. In general, cylinders show less variability of this ratio with shape than surface-equivalent spheroids.

Plate 10.5 shows that the narrow positive branch separating the side- and backscattering negative regions in the ratios a_3/a_1 and a_4/a_1 for spheres is already absent for the least aspherical cylinders, with $D/L = 1$, and that the shape dependence of both ratios for cylinders is rather weak. As for the case of spheroids, the region of negative a_3/a_1 values is wider and deeper than that for a_4/a_1. For most scattering angles and size parameters a_4/a_1 is larger than a_3/a_1. Also, unlike the ratio a_3/a_1, the ratio a_4/a_1 can be positive at backscattering angles. However, the shape dependence of the backscattering region of positive a_4/a_1 values may represent a noticeable difference between cylinders and spheroids. Specifically, for cylinders this region becomes more pronounced with increasing ε, whereas for prolate spheroids it can become significantly weaker.

As discussed in the preceding section, the most remarkable feature of the linear

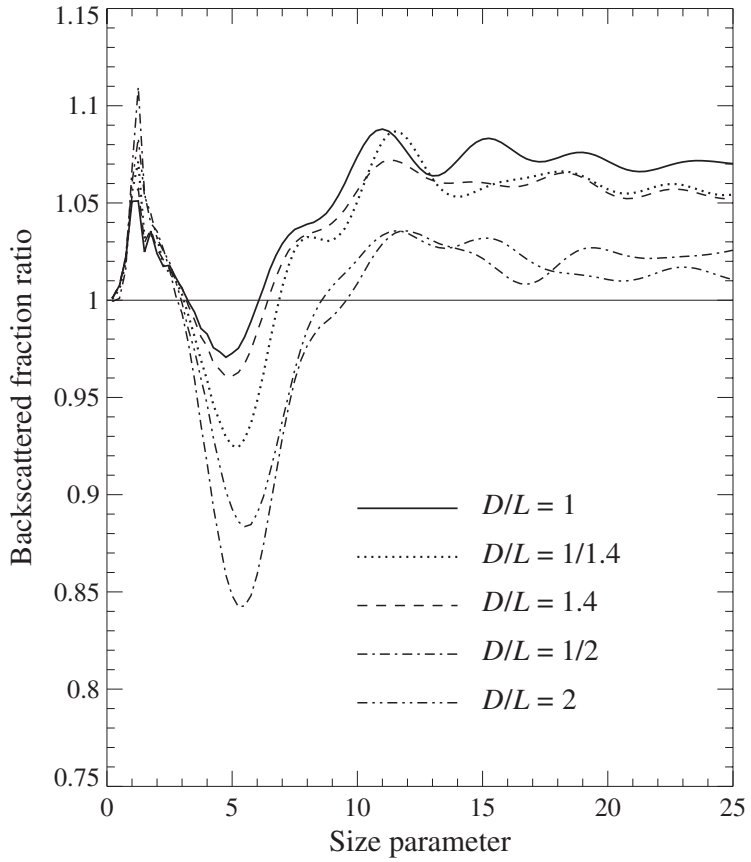

Figure 10.22. As in Fig. 10.17, but for the backscattered fraction ratio.

polarization for polydisperse, randomly oriented spheroids is a bridge of positive polarization at scattering angles near 120° extending upwards from the region of Rayleigh scattering. This bridge was observed by Perry *et al.* (1978) in laboratory measurements of light scattering by narrow size distributions of nearly cubical NaCl particles with mean size parameters ranging from 3.1 to 19.9. Positive polarization at side-scattering angles was also found in laboratory measurements by Sassen and Liou (1979) for platelike ice crystals and in measurements by Kuik (1992) for irregular quartz grains (see also Section 10.7). Plate 10.6 (middle column) shows that randomly oriented polydisperse cylinders do not produce as pronounced a bridge of positive polarization as that found for spheroids. Instead, prolate and oblate cylinders with $D/L = 1/2$ and 2 produce what can be called a bridge of neutral polarization at about the same scattering angles, whereas the axis-ratio-equivalent spheroids produce a bridge of weak but distinctly positive polarization (Plates 10.2(e), (f)). As for spheroids, one of the effects of increasing aspect ratio for cylinders is to make the overall polarization pattern more neutral and featureless. Another common effect of increasing asphericity is to extend the region of Rayleigh polarization to larger size parameters (Section 10.4).

As we have seen previously, the general pattern of the sign of the ratio b_2/a_1 is

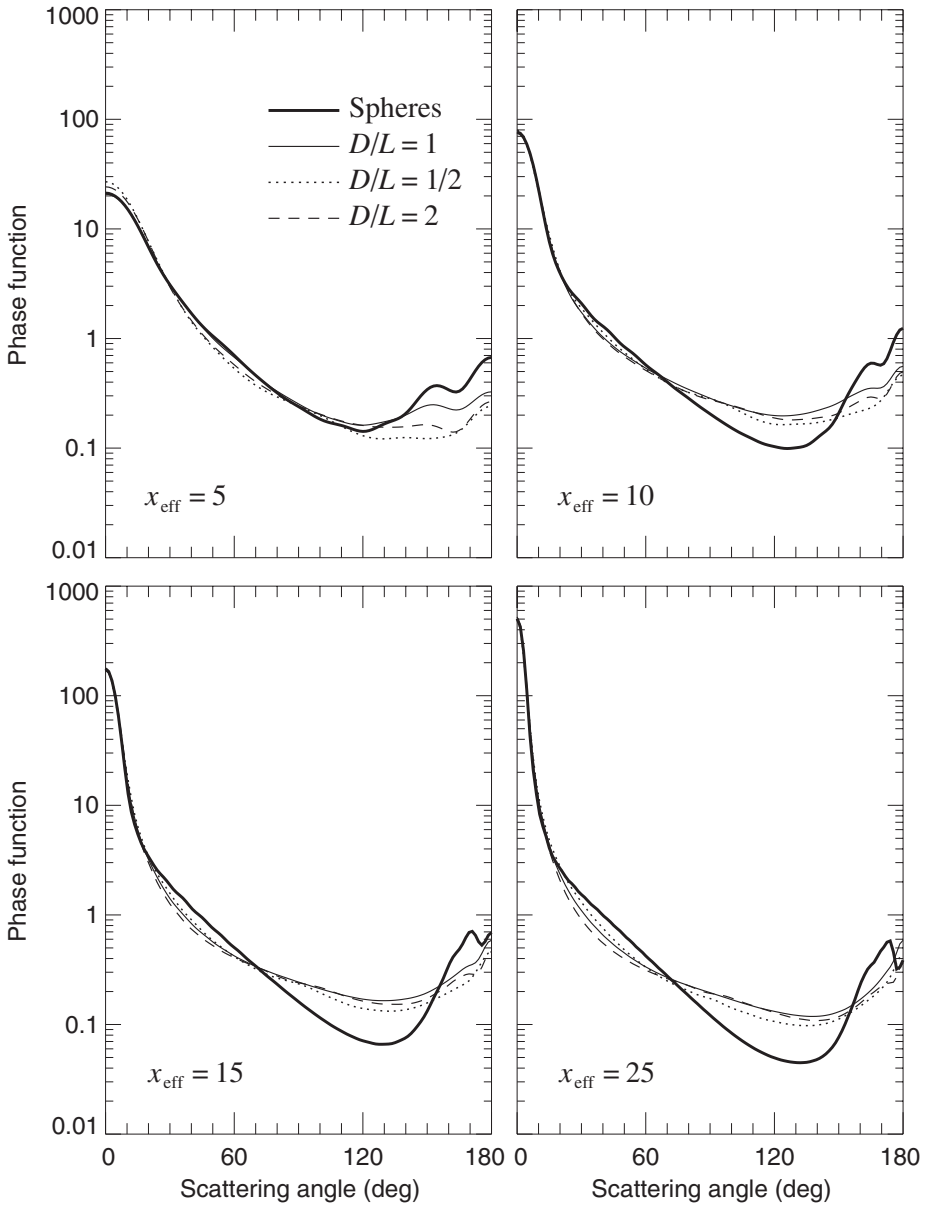

Figure 10.23. Phase function versus scattering angle for polydisperse, randomly oriented cylinders and surface-equivalent spheres with effective size parameters x_{eff} = 5, 10, 15, and 25.

the same for spheres and spheroids, with a broad side-scattering region of negative values separating two positive branches at small and large scattering angles. Plate 10.6 (right-hand column) suggests that this general pattern is also typical of polydisperse, randomly oriented cylinders. However, cylinders show less variability of the ratio b_2/a_1 with particle shape than spheroids. The forward-scattering region seems to be especially shape independent, thus rendering possible the use of the Lorenz–Mie theory at small scattering angles for sizing nonspherical particles. This conclusion is

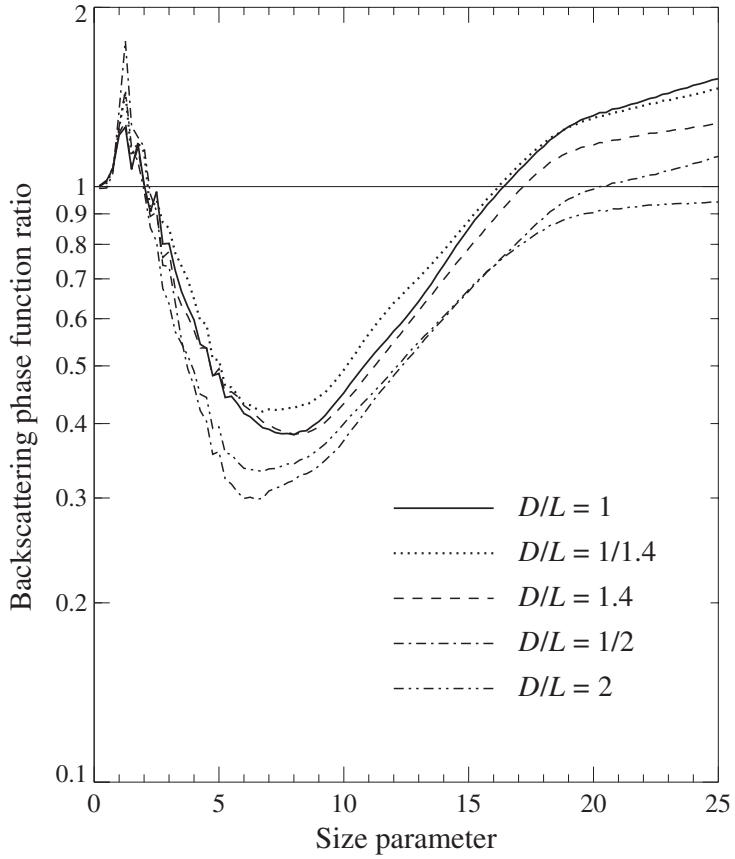

Figure 10.24. As in Fig. 10.17, but for the ratio of the phase function values at $\Theta = 180°$.

in full agreement with the above-mentioned laboratory measurements by Perry *et al.* (1978) for wavelength-sized salt particles.

Figures 10.26 and 10.27 show linear and circular backscattering depolarization ratios computed for randomly oriented polydisperse cylinders. As was the case for spheroids, both ratios for cylinders deviate substantially from zero, thus illustrating their usefulness as indicators of nonsphericity. Similarly, large and even maximal depolarization values can be reached at size parameters smaller than 6, i.e., for particles with equivalent-sphere radii smaller than the wavelength of the incident light.

10.4 Randomly oriented spheroids and circular cylinders with extreme aspect ratios

It turns out that wavelength-sized spheroids and cylinders with extreme aspect ratios may have scattering properties dramatically different from those of moderately aspherical particles. We begin by discussing the results of *T*-matrix calculations for the following five particle shapes: spheres, prolate spheroids with axis ratios $a/b = 1/2$

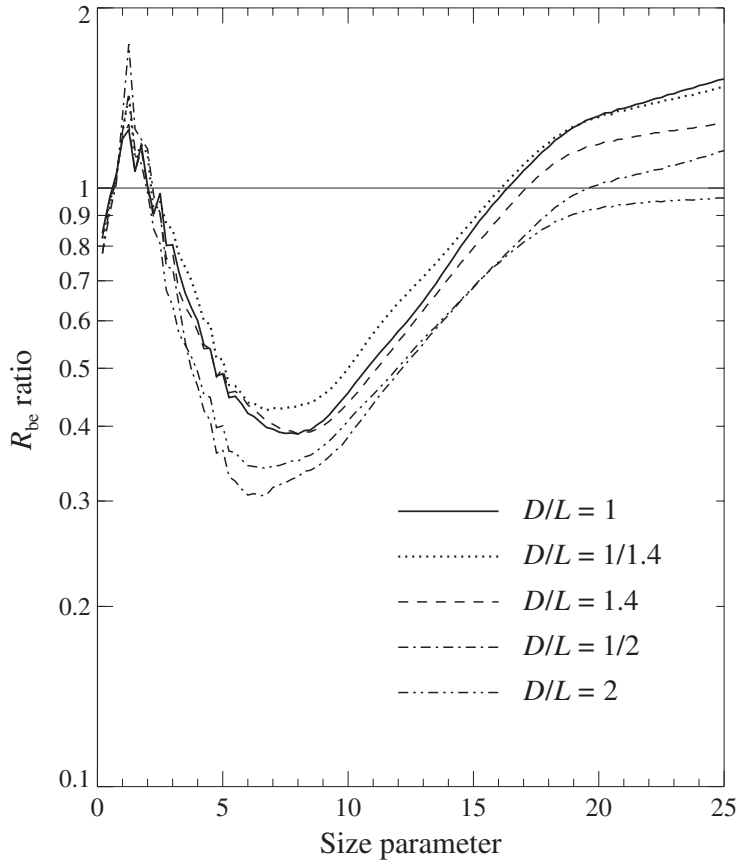

Figure 10.25. As in Fig. 10.17, but for the ratio of the respective R_{be} values.

and $1/20$, and oblate spheroids with $a/b = 2$ and 20 (Zakharova and Mishchenko 2000). The size of a spheroid is specified in terms of the surface-equivalent-sphere radius r_s. To suppress the interference structure in light-scattering patterns for spheres and randomly oriented spheroids with $a/b = 1/2$ and 2, the computation results are averaged over a narrow gamma distribution of equivalent-sphere radii, given by Eq. (5.245) with an effective variance of $v_{eff} = 0.05$. Size averaging is unnecessary for needlelike and platelike spheroids with $a/b = 1/20$ and 20, respectively, since their scattering patterns are sufficiently smoothed out by orientation averaging. Table 10.3 lists the surface-equivalent-sphere size parameters $x_s = 2\pi r_s/\lambda_1$ for monodisperse spheroids with $a/b = 1/20$ and 20 and the effective surface-equivalent-sphere size parameters $x_{s,eff} = 2\pi r_{s,eff}/\lambda_1$ for spheres and polydisperse spheroids with $a/b = 1/2$ and 2 used in the computations. The maximum values of x_s for spheroids with $a/b = 1/20$ and 20 were limited by the growing numerical instability of the T-matrix computations (subsections 5.8.4 and 5.11.7). For comparison, Table 10.3 also lists the corresponding values of the volume-equivalent-sphere size parameters $x_v = 2\pi r_v/\lambda_1$ and $x_{v,eff} = 2\pi r_{v,eff}/\lambda_1$, as well as the respective size parameters along the horizontal and vertical spheroid axes $x_a = 2\pi a/\lambda_1$, $x_{a,eff} = 2\pi a_{eff}/\lambda_1$,

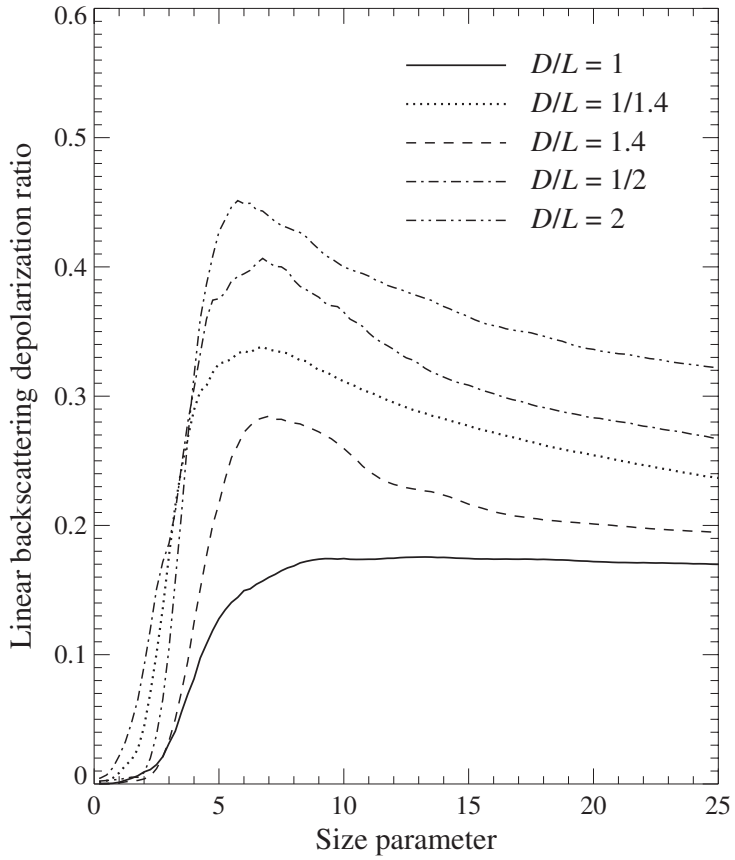

Figure 10.26. Linear backscattering depolarization ratio versus effective size parameter for randomly oriented polydisperse cylinders.

$x_b = 2\pi b/\lambda_1$, and $x_{b,\text{eff}} = 2\pi b_{\text{eff}}/\lambda_1$. The relative refractive index is fixed at 1.311, which is a value typical of water ice in air at visible wavelengths (Warren 1984).

Figure 10.28 shows the extinction efficiency factor $Q_{\text{ext}} = \langle C_{\text{ext}} \rangle / \langle G \rangle$, the asymmetry parameter $\langle \cos\Theta \rangle$, and the efficiency factor for radiation pressure $Q_{\text{pr}} = Q_{\text{ext}}[1 - \langle \cos\Theta \rangle]$, where $\langle C_{\text{ext}} \rangle$ is the ensemble-averaged scattering cross section per particle and $\langle G \rangle$ is the average area of the particle geometric projection. Because the imaginary part of the relative refractive index is set to be zero, the scattering efficiency factor is equal to Q_{ext}, the absorption efficiency factor is equal to zero, and the single-scattering albedo is equal to unity. Figures 10.29 and 10.30 depict the elements of the normalized Stokes scattering matrix versus scattering angle.

Figures 10.29 and 10.30 show that needlelike and platelike particles with moderate equivalent-sphere size parameters possess unique scattering properties. While their phase functions are similar to those of surface-equivalent spheres and compact spheroids and have a pronounced forward-scattering lobe, all other elements of the scattering matrix closely resemble those of particles much smaller than the wavelength (Rayleigh scatterers). In particular, all linear polarization curves $(-b_1/a_1)$ for

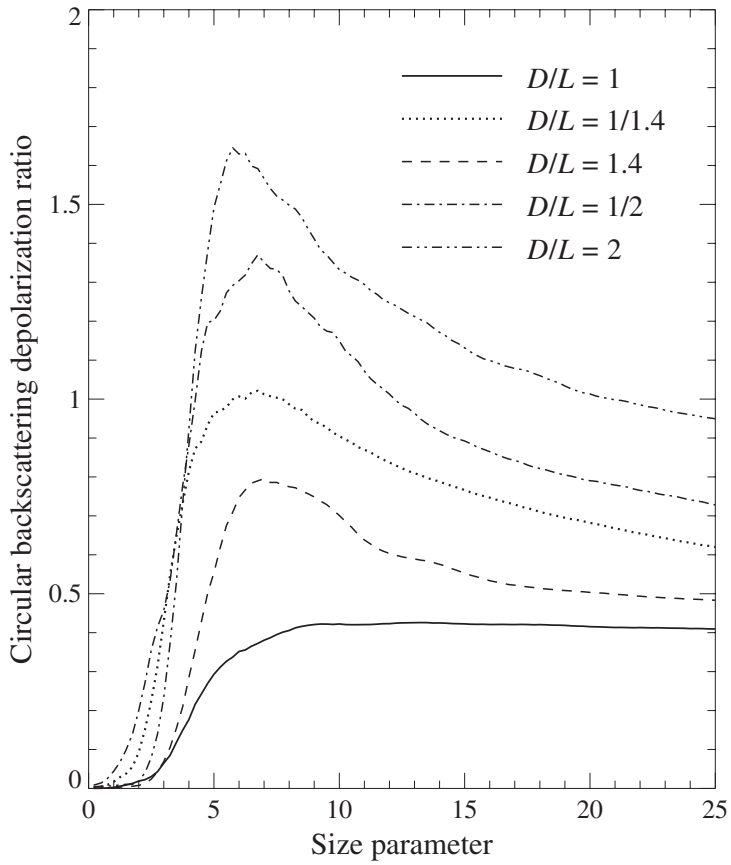

Figure 10.27. As in Fig. 10.26, but for the circular backscattering depolarization ratio.

the spheroids with axis ratios $1/20$ (first row) and 20 (fifth row) have a characteristic bell-like shape, with a maximum reaching nearly 100% at scattering angles close to $90°$; a_2/a_1 is very close to unity; and the elements a_3 and a_4 are nearly equal to each other. The fact that $a_2(\pi) \approx a_1(\pi)$ and $a_4(\pi) \approx -a_1(\pi)$ yields linear and circular depolarization ratios (as defined by Eqs. (10.2) and (10.3)) close to zero, whereas wavelength-sized spheroids with axis ratios $1/2$ and 2 give rise to significant backscattering depolarization. This demonstrates once again that the magnitude of the depolarization ratios is not a universal indicator of the degree of particle asphericity. The extinction and radiation-pressure efficiency factors for highly aspherical spheroids are significantly smaller than those for spheres and compact spheroids having the same average projected area, whereas the values of the asymmetry parameter are rather similar. This is yet another indication that the particular scattering properties of platelike and needlelike spheroids with moderate size parameters can resemble either those of Rayleigh particles or those of surface-equivalent spheres.

The linear polarization curves for spheres show that the regime of Rayleigh scattering breaks down at size parameters close to unity. According to Table 10.3, the

Table 10.3. Surface-equivalent-sphere size parameters x_s (or $x_{s,eff}$), volume-equivalent-sphere size parameters x_v (or $x_{v,eff}$), and size parameters x_a (or $x_{a,eff}$) along the horizontal spheroid axes and x_b (or $x_{b,eff}$) along the vertical spheroid axes, as used in the *T*-matrix computations

$a/b = 1/20$	x_s	x_v	x_a	x_b
	1	0.6845	0.2522	5.0432
	2	1.3690	0.5043	10.087
	3.5	2.3957	0.8826	17.651
$a/b = 1/2$	$x_{s,eff}$	$x_{v,eff}$	$x_{a,eff}$	$x_{b,eff}$
	1	0.9637	0.7649	1.5298
	2	1.9274	1.5298	3.0596
	3.5	3.3730	2.6771	5.3543
	12	11.565	9.1788	18.358
$a/b = 2$	$x_{s,eff}$	$x_{v,eff}$	$x_{a,eff}$	$x_{b,eff}$
	1	0.9554	1.2038	0.6019
	2	1.9109	2.4076	1.2038
	3.5	3.3441	4.2132	2.1066
	12	11.465	14.445	7.2227
$a/b = 20$	x_s	x_v	x_a	x_b
	1	0.5186	1.4077	0.0704
	2	1.0372	2.8155	0.1408
	3.5	1.8151	4.9271	0.2464
	12	6.2233	16.893	0.8446

size parameter along the shorter axis of the spheroids with axis ratios $1/20$ and 20 is smaller than unity even for the largest x_s-values considered. Therefore, these *T*-matrix results may be indicating that the asymmetry parameter and the phase function are mostly determined by the value of the size parameter of the sphere having the same projected area, whereas all other elements of the scattering matrix and the optical cross sections are more sensitive to the value of the size parameter along the smallest particle dimension. It is interesting to note in this regard that West (1991) found similar features in light scattering by low-density aggregates of spheres with outer diameters comparable to the wavelength and monomer sizes much smaller than the wavelength. He concluded that the forward-scattering lobe of the phase function was diagnostic of the mean projected area of the entire cluster, whereas the angular dependence of the linear polarization depended largely on the monomer radius.

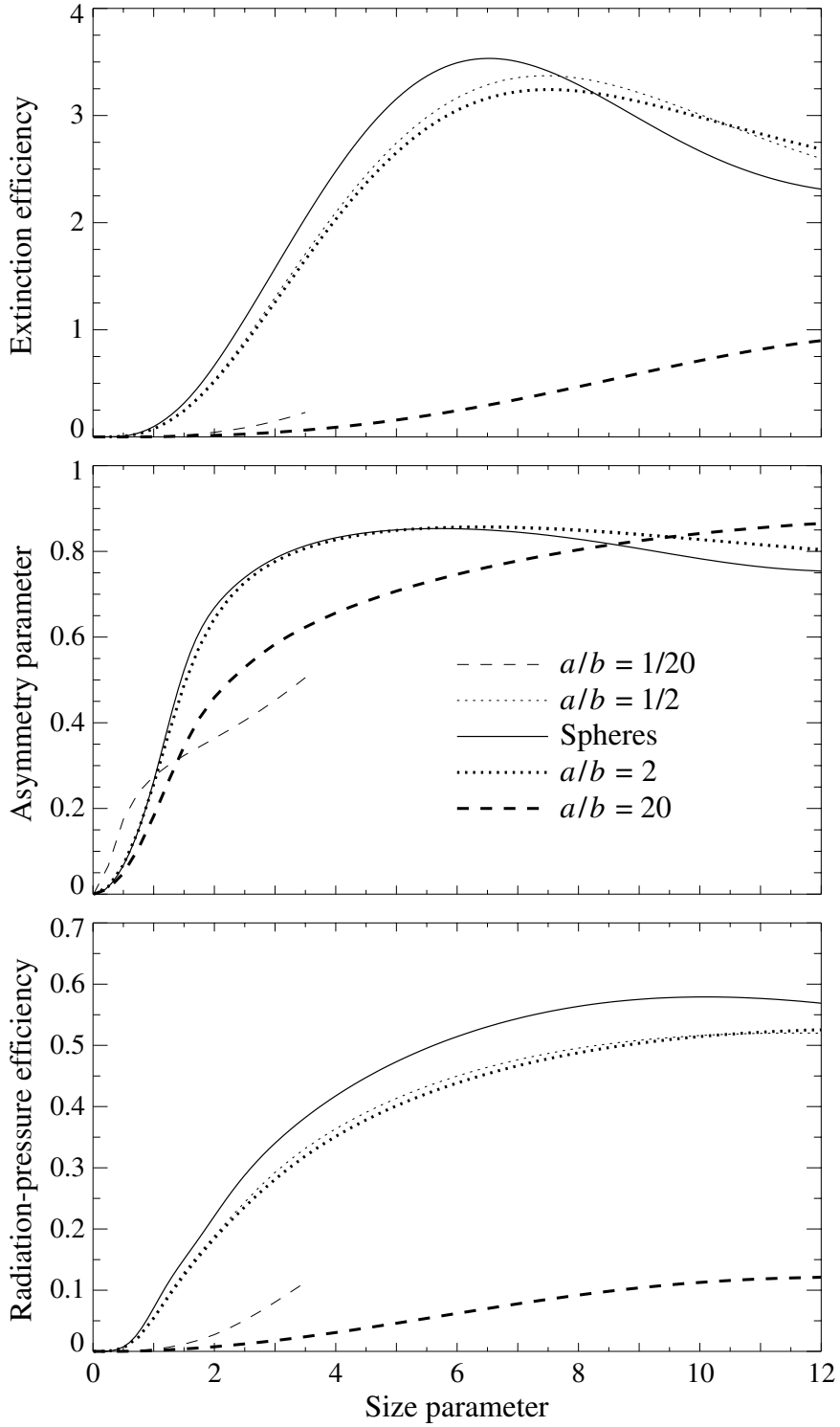

Figure 10.28. Extinction efficiency factor, asymmetry parameter, and radiation-pressure efficiency factor versus surface-equivalent-sphere size parameter for spheres and randomly oriented spheroids with various axis ratios a/b. Note that the asymmetry parameter curves for spheroids with $a/b = 1/2$ and 2 almost coincide.

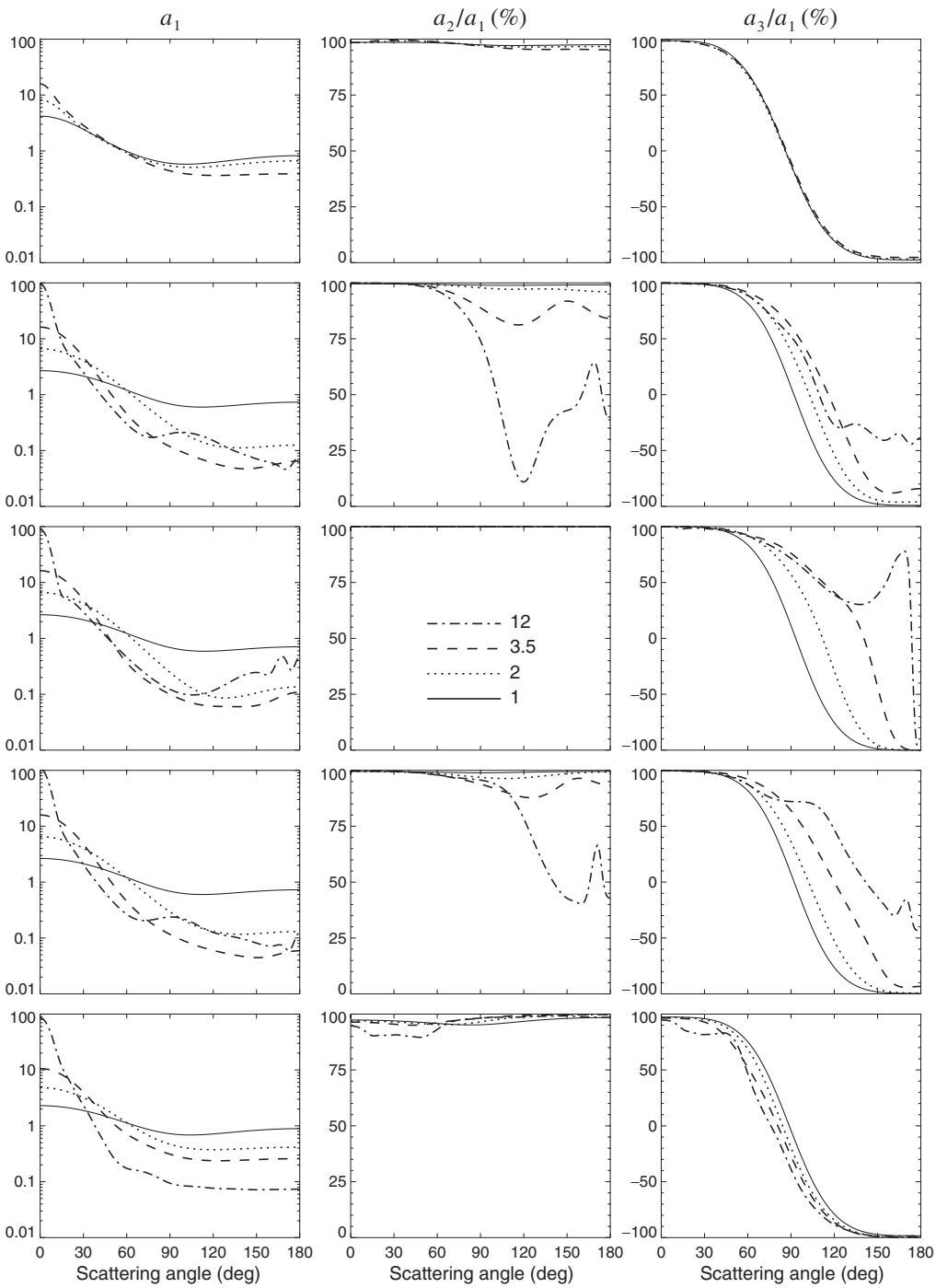

Figure 10.29. The phase function a_1 and the ratios a_2/a_1 and a_3/a_1 versus scattering angle Θ for spheres and surface-equivalent, randomly oriented spheroids with size parameters ranging from 1 to 12 (see legend) and axis ratios $1/20$ (first row), $1/2$ (second row), 1 (third row), 2 (fourth row), and 20 (fifth row). Note that for spheres $a_2/a_1 \equiv 100\%$.

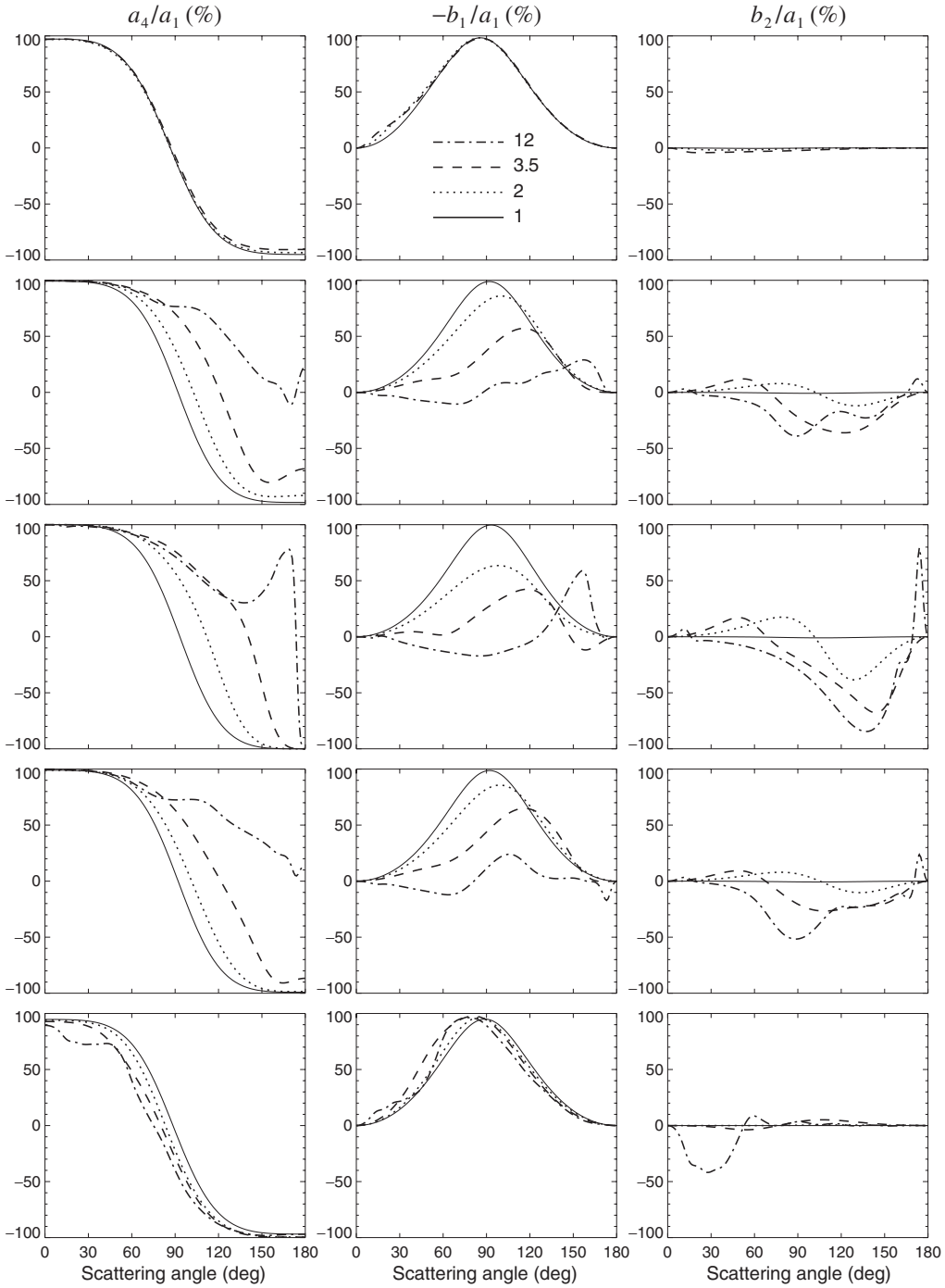

Figure 10.30. The ratios a_4/a_1, $-b_1/a_1$, and b_2/a_1 versus scattering angle Θ for spheres and surface-equivalent, randomly oriented spheroids with size parameters ranging from 1 to 12 (see legend) and axis ratios $1/20$ (first row), $1/2$ (second row), 1 (third row), 2 (fourth row), and 20 (fifth row).

Since spheroids are particles with smooth surfaces, it is instructive to verify whether sharp-edged wavelength-sized cylinders with extreme aspect ratios possess similar scattering properties. The computation of light scattering by prolate ice cylinders with very large length-to-diameter ratios L/D turns out to be problematic even with the extended-precision *T*-matrix code, because of poor convergence. However, Zakharova and Mishchenko (2001) managed to perform computations for randomly oriented oblate ice cylinders with surface-equivalent-sphere size parameters up to 12 and diameter-to-length ratios D/L as large as 20. The results of their computations for cylinders with $D/L = 1$ and 20 and surface-equivalent spheres are summarized in Figs. 10.31–10.33. As in previous computations, the interference structure is suppressed by averaging the results for spheres and cylinders with $D/L = 1$ over a narrow gamma distribution of surface-equivalent-sphere radii with effective variance $v_{\text{eff}} = 0.05$. The curves for monodisperse cylinders with $D/L = 20$ are sufficiently smooth already and do not require averaging over sizes. Accordingly, the size of the cylinders with $D/L = 20$ is specified in Figs. 10.31–10.33 in terms of the monodisperse surface-equivalent-sphere size parameter x_{s}, whereas the size of polydisperse spheres and cylinders with $D/L = 1$ is specified in terms of the effective surface-equivalent-sphere size parameter $x_{\text{s,eff}}$. The relative refractive index is fixed at 1.311.

Examination of Figs. 10.31–10.33 shows that, despite their sharp-edged shapes, wavelength-sized circular ice disks with extreme aspect ratios possess the same scattering properties as smooth platelike spheroids. Specifically, their phase functions are similar to those of surface-equivalent spheres and nonspherical particles (spheroids and cylinders) with moderate aspect ratios and have a forward-scattering lobe whose magnitude rapidly increases with size parameter. In contrast, all other elements of the scattering matrix closely resemble those of the Rayleigh scattering matrix as long as the size parameter along the smallest cylinder dimension is less than unity. Specifically, all curves of linear polarization $(-b_1/a_1)$ for plates with $D/L = 20$ have the renowned bell-like shape with a maximum approaching 100% at side-scattering angles. Unlike the case for the compact particles, the scattering angle of maximal positive polarization decreases rather than increases with increasing size parameter. The ratio a_2/a_1 is close to unity, the elements a_3 and a_4 are almost the same and do not vary significantly with size parameter, and the ratio b_2/a_1 is close to zero at most scattering angles. This behavior differs substantially from that exhibited by surface-equivalent spheres and compact nonspherical particles.

These *T*-matrix results are in excellent agreement with the results of recent laboratory measurements of electromagnetic scattering by randomly oriented plates with very large diameter-to-thickness ratios and thicknesses smaller than the wavelength (Waldemarsson and Gustafson 2000). Indeed, these microwave analog data (Fig. 8.4) also show phase functions characteristic of compact wavelength-sized particles and polarization curves typical of Rayleigh scattering. In particular, the observed maximal polarization values approach 100% and occur at scattering angles less than 90°.

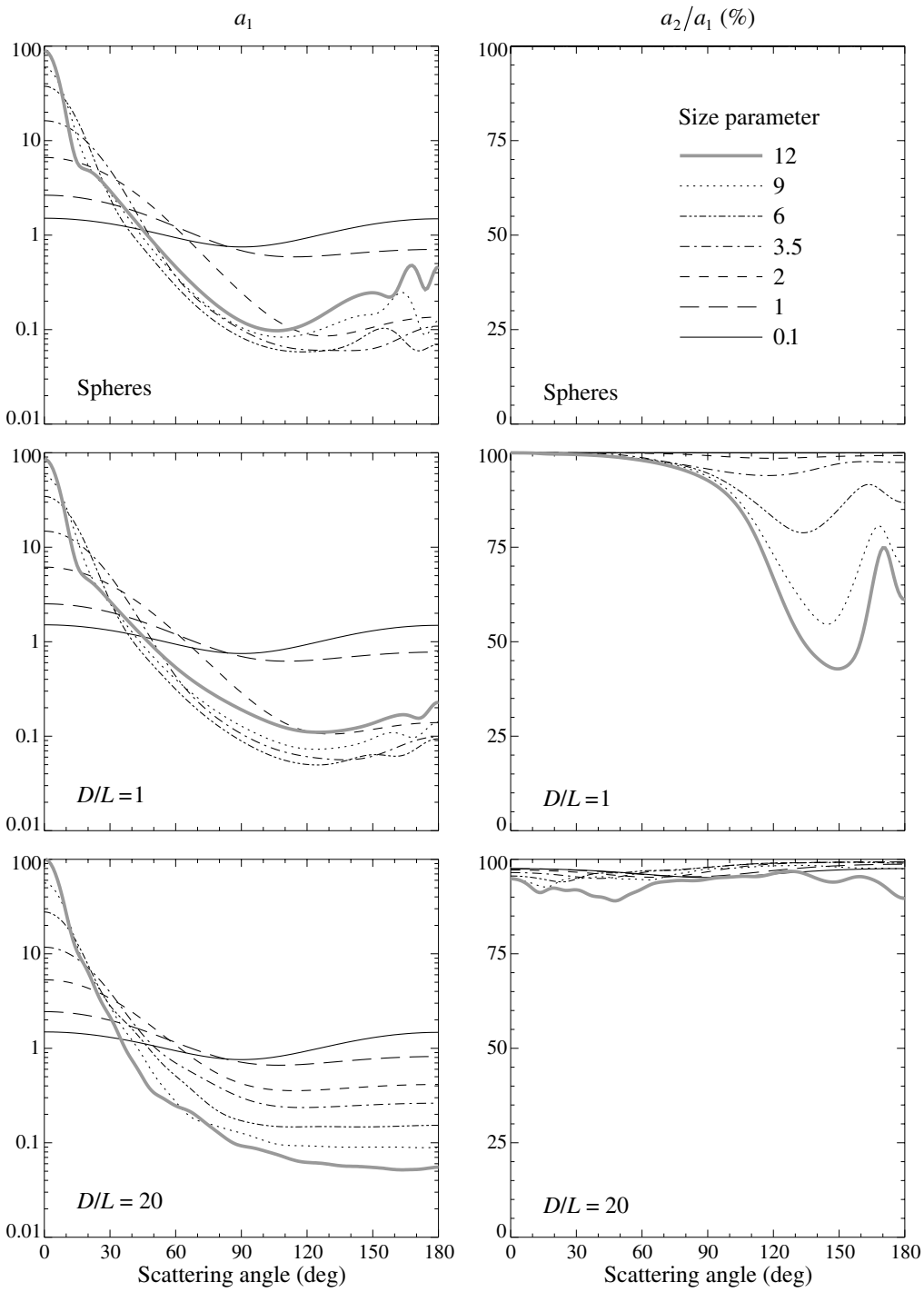

Figure 10.31. The phase function a_1 and the ratio a_2/a_1 versus scattering angle Θ for spheres with size parameters ranging from 0.1 to 12 (see legend) and surface-equivalent, randomly oriented circular cylinders with $D/L = 1$ and 20. Note that for spheres $a_2/a_1 = 100\%$ for all values of Θ.

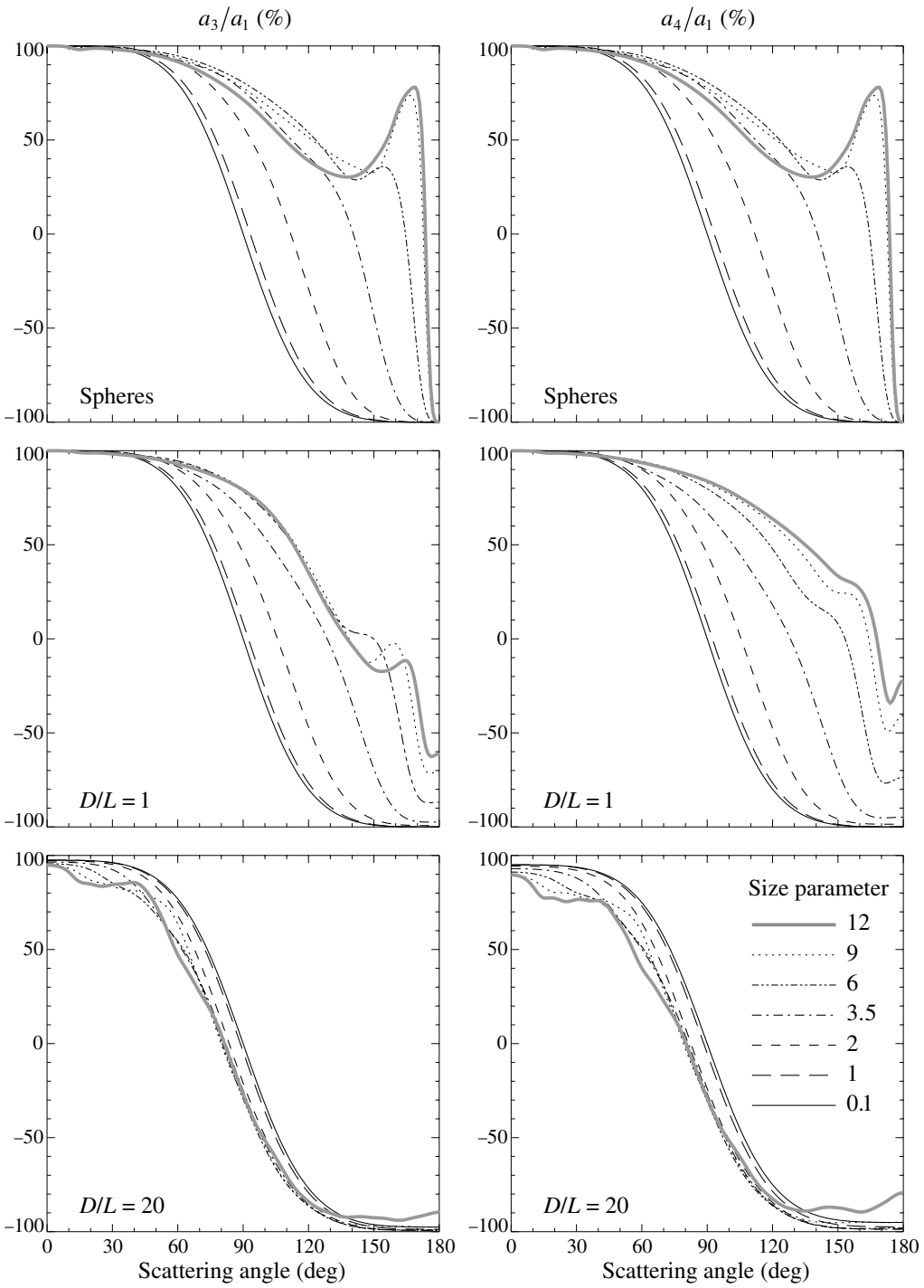

Figure 10.32. The ratios a_3/a_1 and a_4/a_1 versus scattering angle Θ for spheres with size parameters ranging from 0.1 to 12 (see legend) and surface-equivalent, randomly oriented circular cylinders with $D/L = 1$ and 20.

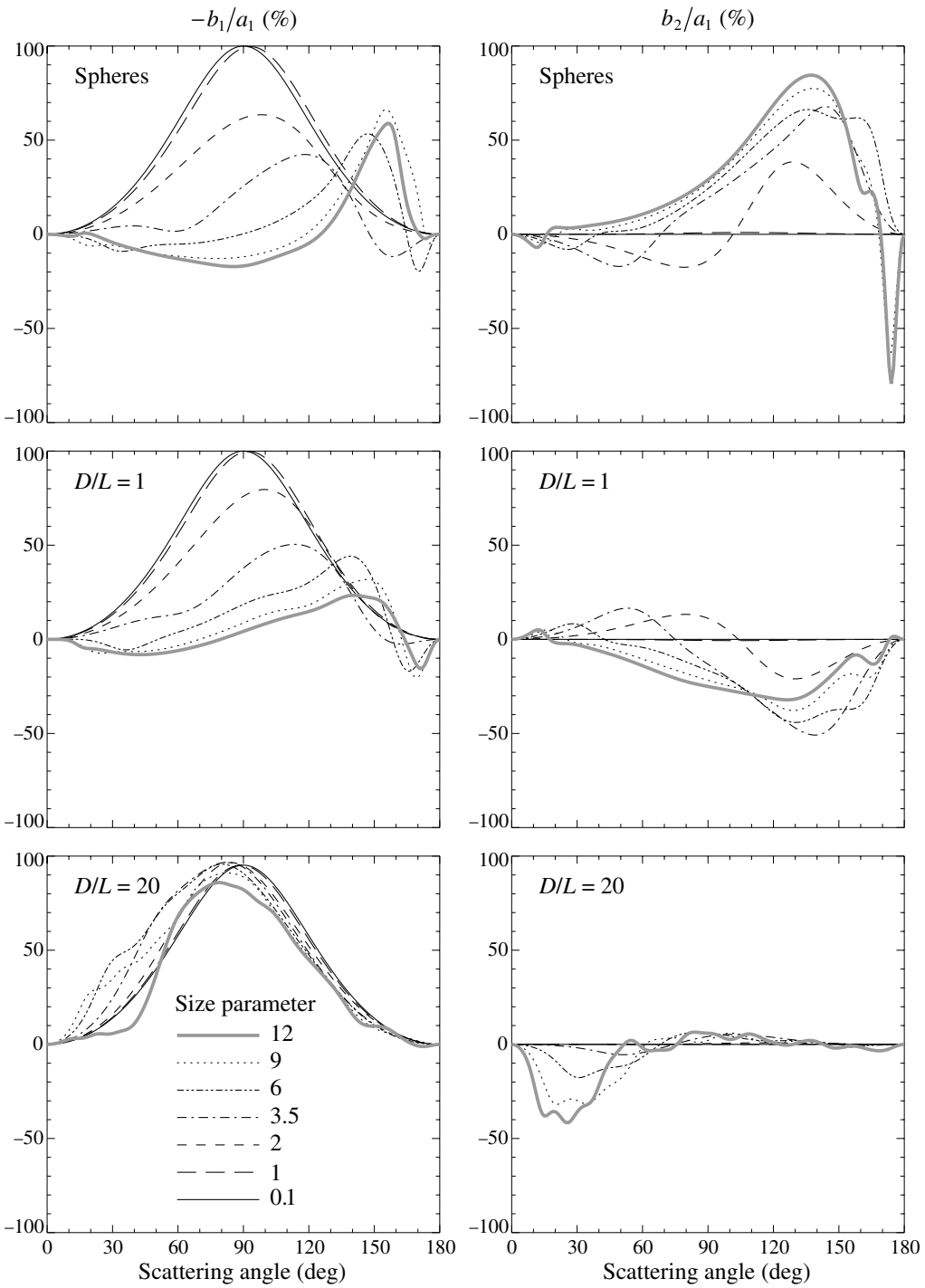

Figure 10.33. The ratios $-b_1/a_1$ and b_2/a_1 versus scattering angle Θ for spheres with size parameters ranging from 0.1 to 12 (see legend) and surface-equivalent, randomly oriented circular cylinders with $D/L = 1$ and 20.

As discussed by Zakharova and Mishchenko (2000), the unusual scattering properties of wavelength-sized nonspherical particles with extreme aspect ratios should be given adequate consideration in analyses of laboratory and remote sensing measurements of light scattering. For example, small measured values of depolarization should not be identified automatically with Rayleigh scattering or a spherical particle shape. Similarly, measurements of Rayleigh-like polarization (e.g. Tozer and Beeson 1974; Witt *et al.* 1976; Tomasko *et al.* 1978; West and Smith 1991) should not be attributed necessarily to particles much smaller than a wavelength.

The simplicity of the normalized Stokes scattering matrix for needlelike and platelike particles with moderate size parameters allows for a convenient analytical parameterization similar to those developed by West *et al.* (1983) and Braak *et al.* (2001). Such parameterizations can be useful in first-order analyses of remote sensing observations when the plausible range of particle microphysical characteristics is unknown and is difficult to guess. Also, the *T*-matrix results discussed in this section provide a benchmark for checking the accuracy of approximate formulations of light scattering by wavelength-sized particles with one dimension much smaller than the wavelength (Weil and Chu 1976, 1980; Uzunoglu *et al.* 1978; Schiffer and Thielheim 1979).

10.5 Chebyshev particles

An interesting study of electromagnetic scattering by rotationally symmetric Chebyshev particles (see subsection 5.11.2 and Fig. 5.8) was performed by Wiscombe and Mugnai (see Mugnai and Wiscombe 1980, 1986, 1989; Wiscombe and Mugnai 1986, 1988). They compared the radiometric scattering and absorption characteristics of randomly oriented Chebyshev particles having various deformation and waviness parameters and those of volume-equivalent spheres. The relative refractive index was fixed at 1.5 + i0.02. The results of Wiscombe and Mugnai largely parallel those described in Sections 10.2 and 10.3. Minor differences in the conclusions reached may be the consequence of comparing the optical properties of volume-equivalent rather than surface-equivalent spherical and nonspherical particles. Perhaps the most interesting geometrical property of Chebyshev particles is that they become partially concave as the absolute value of the deformation parameter exceeds a certain threshold range, whereas spheroids and circular cylinders are always convex bodies. In this regard the conclusion of Wiscombe and Mugnai that concavity almost always enhances the nonspherical–spherical differences appears to be especially important and deserves further study. Mishchenko and Travis (1994b) computed linear polarization patterns for randomly oriented, polydisperse Chebyshev particles with $n = 4$, $\xi = \pm 0.1$, and m = 1.5 + i0.02 and concluded that they were distinctly different from those computed for volume-equivalent spheroids with a comparable degree of asphericity.

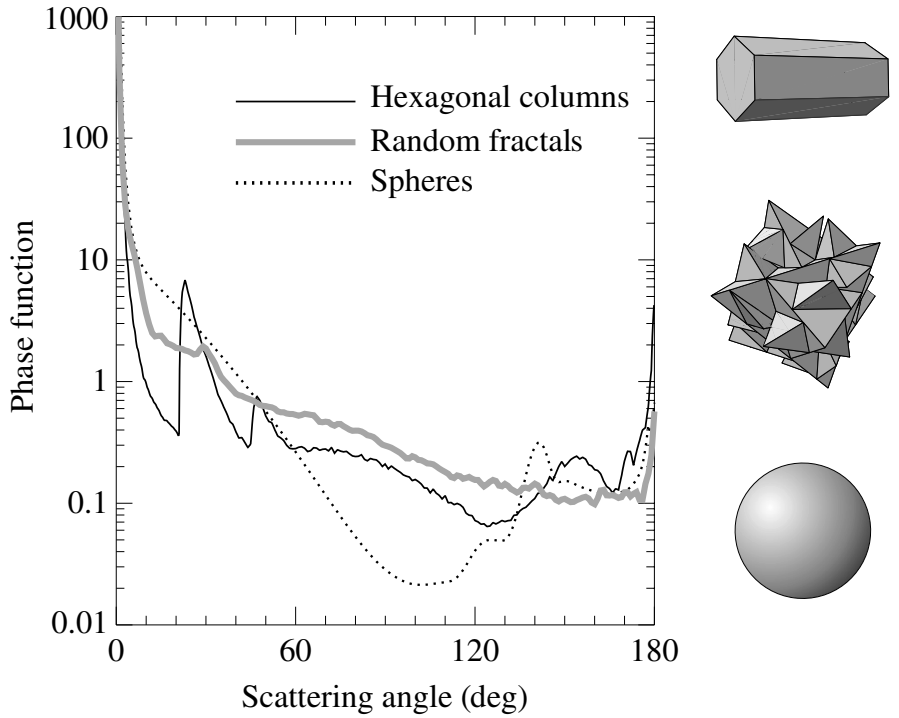

Figure 10.34. Phase function versus scattering angle for polydisperse randomly oriented hexagonal ice columns with length-to-diameter ratio 2, polydisperse random-fractal ice particles in random orientation, and polydisperse spherical water droplets at a wavelength $\lambda_1 = 0.63\,\mu\text{m}$.

10.6 Regular polyhedral particles

By definition, polyhedral particles are bounded by surfaces composed of plane facets. Typical examples of regular polyhedrons are tetrahedrons, cubes, and hexagonal cylinders. The scattering and absorption properties of such particles have been computed mostly using the geometrical optics approximation, hence assuming (explicitly or implicitly) that the wavelength of the incident light is much smaller than the size of the smallest facet on the particle surface. As an example, the heavy solid curve in Fig. 10.34 shows the phase function computed for large, randomly oriented hexagonal ice columns at a visible wavelength. Each hexagonal cylinder comprises three different types of prism: a $60°$ prism formed by alternate side faces, a $90°$ prism formed by side and end faces, and a $120°$ prism formed by adjacent side faces (see Fig. 10.35). The $120°$ prism plays only a minor role in light scattering by ice crystals because total internal reflections prevent any ray entering the first face from being refracted through the second. The most pronounced phase-function features for hexagonal ice crystals are the primary and secondary halos centered at $\Theta \approx 22°$ and $\Theta \approx 46°$ and the strong and narrow backscattering peak. The primary and secondary halos are generated by the same mechanism as the rainbows discussed in Section 9.4 and correspond to minimum angles of deviation for the $60°$ and $90°$ prisms, respec-

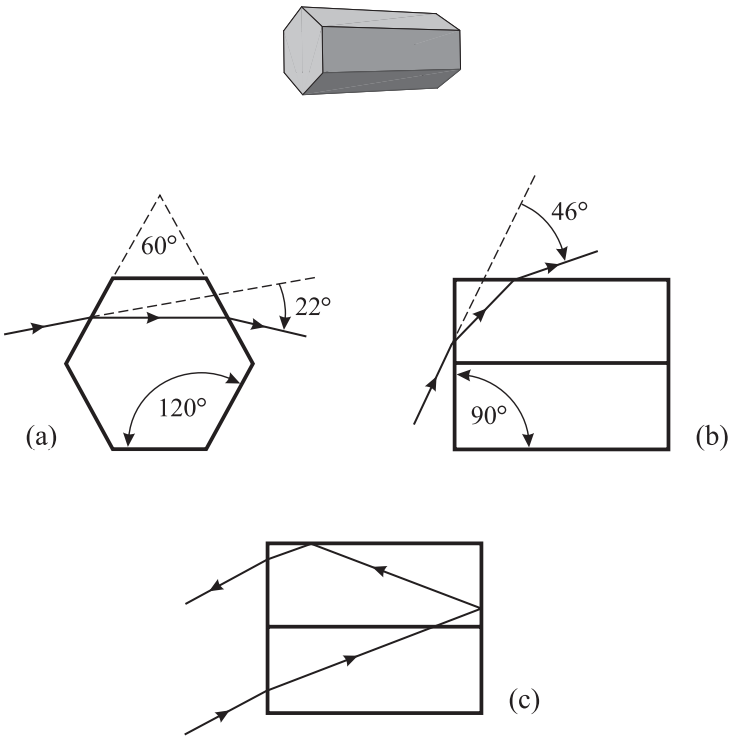

Figure 10.35. (a), (b) Refraction by a hexagonal ice crystal showing the rays associated with the 22° and 46° degree halos. (c) Double internal reflections causing the backscattering intensity peak.

tively, whereas the backscattering peak is caused by rays twice internally reflected by mutually perpendicular faces (see Figs. 10.35 and 10.36). This explains why large, randomly oriented, circular ice cylinders generate the secondary halo and the backscattering peak, but not the primary halo (see the top left-hand panel in Fig. 7.7). The same is true of large, randomly oriented cubes and parallelepipeds (Liou *et al.* 1983).

The geometrical optics approximation allows one to compute the scattering functions for polyhedral particles with extremely complicated shapes (see, e.g., Macke 1993; Iaquinta *et al.* 1995; Takano and Liou 1995; and especially Yang and Liou 1998a) and explains qualitatively many optical phenomena observed for ice crystal clouds (Lynch and Livingston 1995). However, the uncertain numerical accuracy and range of applicability of this approximation are always a concern and often make desirable, if not mandatory, the use of an exact theoretical technique. Figure 10.37 illustrates the application of the finite-difference time-domain method to phase-function computations for randomly oriented, monodisperse polyhedral particles (Yang *et al.* 2000b). Such computations are also possible with the extended boundary condition method (e.g., Laitinen and Lumme 1998; Wriedt and Comberg 1998) and volume integral equation methods (Section 6.5) but they are still limited in terms of the size parameter range and the ability to handle polydisperse ensembles of randomly oriented particles. Further theoretical efforts are obviously required in order to char-

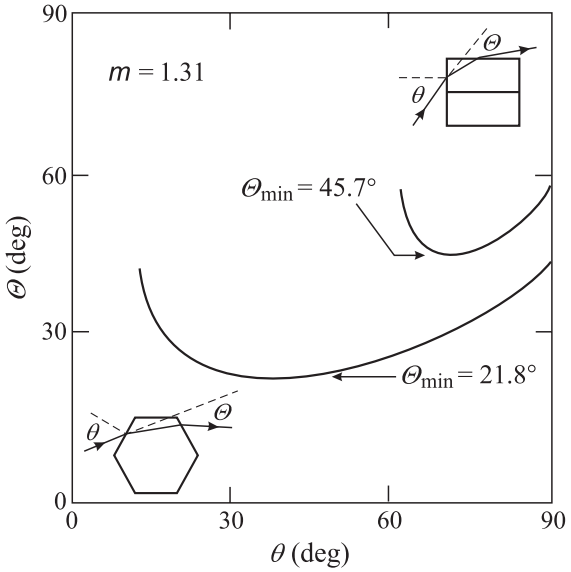

Figure 10.36. Deviation (scattering) angle versus incidence angle for $m = 1.31$. The angle of minimum deviation Θ_{min} is about 22° for the 60° prism and 46° for the 90° prism. The angle of deviation is at a minimum when the light passes symmetrically through the prism and is greater at all other angles of incidence. (After Lynch and Livingston 1995.)

acterize and quantify the specific effects of polyhedral shapes on the scattering and absorption properties of wavelength-sized particles.

10.7 Irregular particles

Many particles encountered in natural and artificial environments have irregular and highly variable shapes. As an example, Fig. 10.38 demonstrates that the shapes of natural cirrus cloud particles can significantly deviate from those of pristine hexagonal columns and plates. In fact, the study by Korolev *et al.* (1999, 2000) indicated that the majority of atmospheric ice particles can be highly irregular, which may explain why, when cirrus clouds are observed, halos and other optical displays characteristic of regular polyhedral ice crystals are seen rather infrequently (e.g., Sassen *et al.* 1994; Francis 1995; Gayet *et al.* 1998; Francis *et al.* 1998; Lawson *et al.* 1998).

The scattering of light by randomly (i.e., stochastically) shaped particles with size parameters less than about 5 has been analyzed using volume integral equation methods and the second-order perturbation approximation (e.g., Lumme and Rahola 1998; Lumme 2000; Muinonen 2000; Chamaillard and Lafon 2001; Nousiainen *et al.* 2001). Nevertheless, the majority of computations for irregular particles have been based on the geometrical optics approximation. For example, Macke *et al.* (1996b) (see also Hess *et al.* 1998) modeled scattering by an ensemble of imperfect hexagonal ice

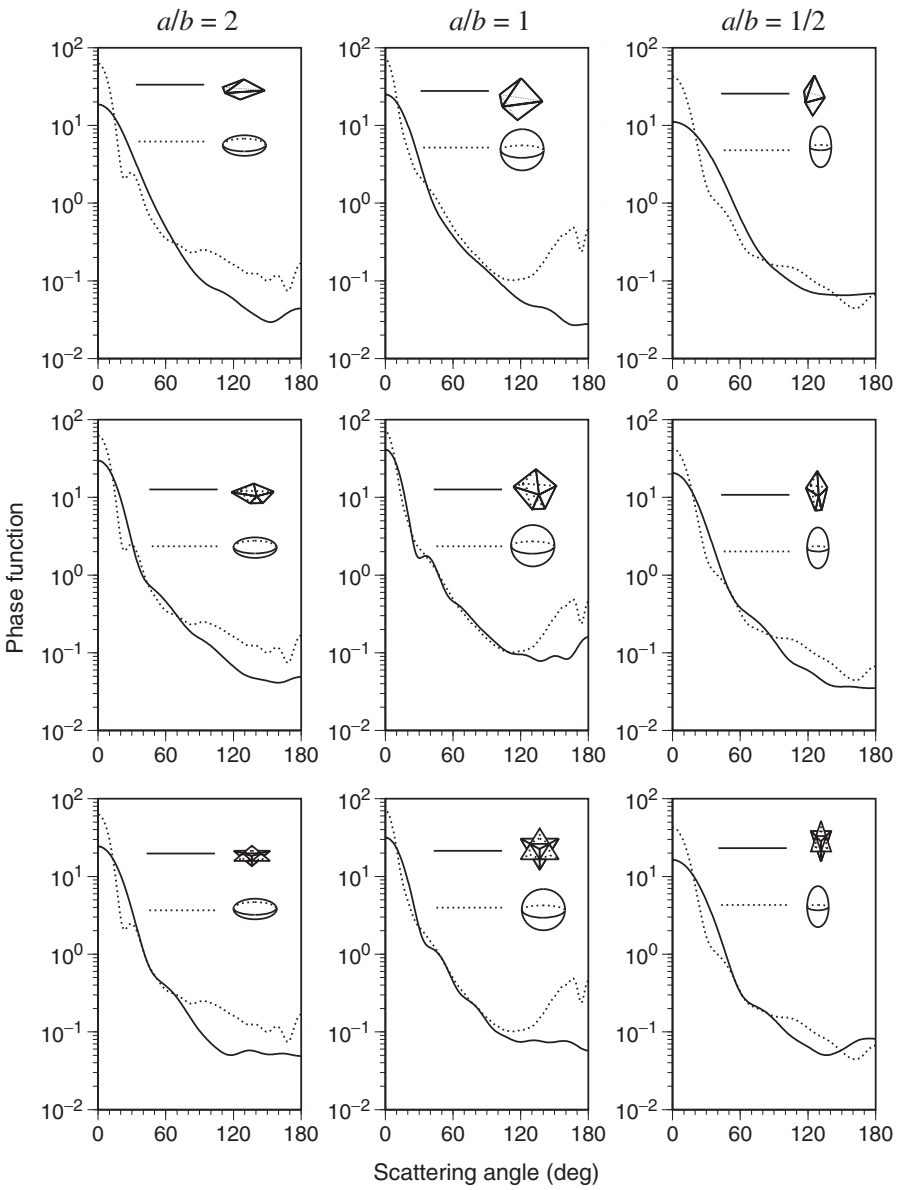

Figure 10.37. Phase functions for monodisperse, randomly oriented, regular polyhedral particles and for spheroids; the relative refractive index is $1.38 + i3.9 \times 10^{-9}$. In the top row, the polyhedra have six faces, in the middle row, ten faces. All particles have the same size parameter, 10, along the semi-major particle dimension. (From Yang *et al.* 2000b.)

crystals by introducing a statistical local distortion of the crystal faces. Specifically, for each reflection–refraction event, the local normal to the crystal surface was tilted randomly about its original direction. The zenith and azimuth tilt angles were chosen randomly from the intervals $[0, \theta^{\max}]$ and $[0, 2\pi]$, respectively, and the degree of crystal distortion was defined by the parameter $t = \theta^{\max}/90°$. Figure 10.39 shows the ray-tracing component of the phase function (i.e., excluding diffraction) and also the linear polarization for large, randomly oriented, prolate ice crystals with an average

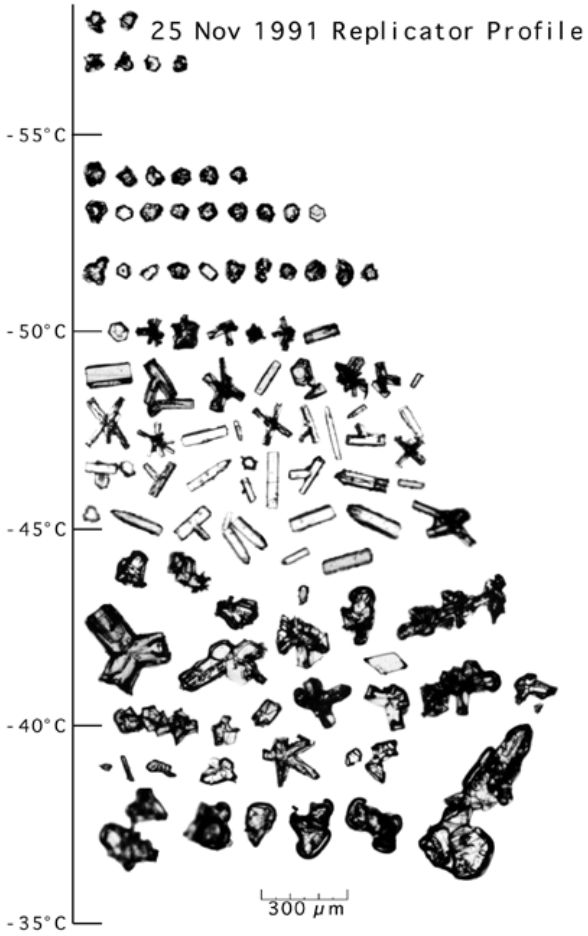

Figure 10.38. Balloon-borne ice crystal replicator data collected on 25 November 1991 near Coffeyville, Kansas. The approximate temperature at the replicator height is indicated along the ordinate. (From Heymsfield and Iaquinta 2000.)

length-to-diameter ratio of 6.2 and three increasing values of the distortion parameter t. Since the relative refractive index is real, the ray-tracing computations do not depend on the particle size relative to the wavelength. While the $t = 0.01$ case shows almost the same phase function and polarization features as those for perfect hexagonal columns (cf. Fig. 10.34), a further increase in the distortion parameter results in progressively smoother phase-function and linear polarization curves. In particular, the primary and secondary halos and the strong backscattering phase-function peak essentially disappear for t-values exceeding 0.1. The side scattering is only slightly affected by increasing crystal distortion because it primarily results from external reflections that are not sensitive to the shape of randomly oriented convex particles. The locations of the neutral polarization points also do not change significantly with increasing t.

Yang and Liou (1998a) employed a similar geometrical optics approach by assuming that surfaces of real ice crystals are rough and consist of a large number of

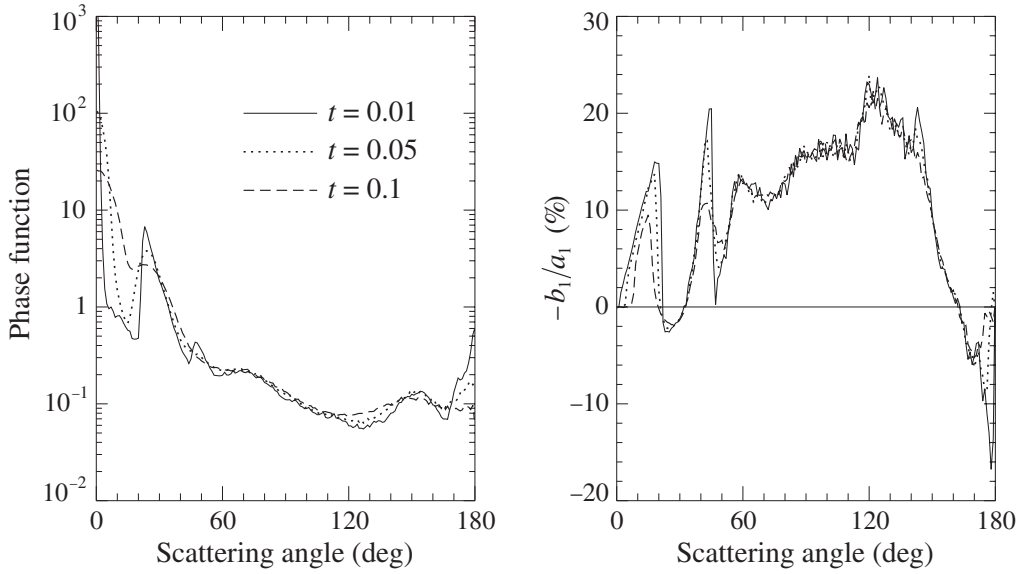

Figure 10.39. The ray-tracing phase function and ratio $-b_1/a_1$ versus scattering angle for randomly oriented hexagonal ice columns with $L/D = 6.2$ and distortion parameters $t = 0.01$, 0.05, and 0.1. The relative refractive index is $m = 1.311$.

microscopic facets that are locally planar and randomly tilted from their orientations corresponding to the case of a smooth surface. The distribution of slopes was assumed to be isotropic and Gaussian with a mean-square surface slope $\sigma^2/2$. Figure 10.40 shows the computation results for randomly oriented clusters composed of nonoverlapping hexagonal ice columns. It is evident that increasing surface roughness strongly affects the scattering properties of ice particles. For the case of smooth crystal surfaces $(\sigma = 0)$, the pronounced peaks at $\Theta = 22°, 46°,$ and $180°$ as well as the intensity maximum at $\Theta \approx 154°$ are features typical of single hexagonal ice crystals in random orientation (cf. Fig. 10.34). Increasing σ smoothes these features out so that the phase function for $\sigma = 0.1$ consists of a strong diffraction peak and a relatively featureless and flat background. Among the other elements of the scattering matrix, the effect of increasing roughness on the ratio $-b_1/a_1$ appears to be the most significant and makes the scattered polarization largely neutral.

In order to model light scattering by highly irregular polyhedral ice particles, Macke *et al.* (1996b) used a random shape generator based on three-dimensional Koch fractals. The construction of a random Koch fractal is demonstrated in Fig. 10.41. The initial particle (zeroth-generation fractal) is a regular tetrahedron. The first- and second-generation regular Koch fractals are shown in the left-hand column and are obtained via the standard process of self-replication. Progressively disordered versions of these particles are achieved by introducing increasing random displacements of the particle vertices, as shown in the right-hand column. The degree of distortion is defined by the maximum displacement length divided by the length of the crystal segments (as a percentage). Figure 10.42 shows the evolution of the ray-

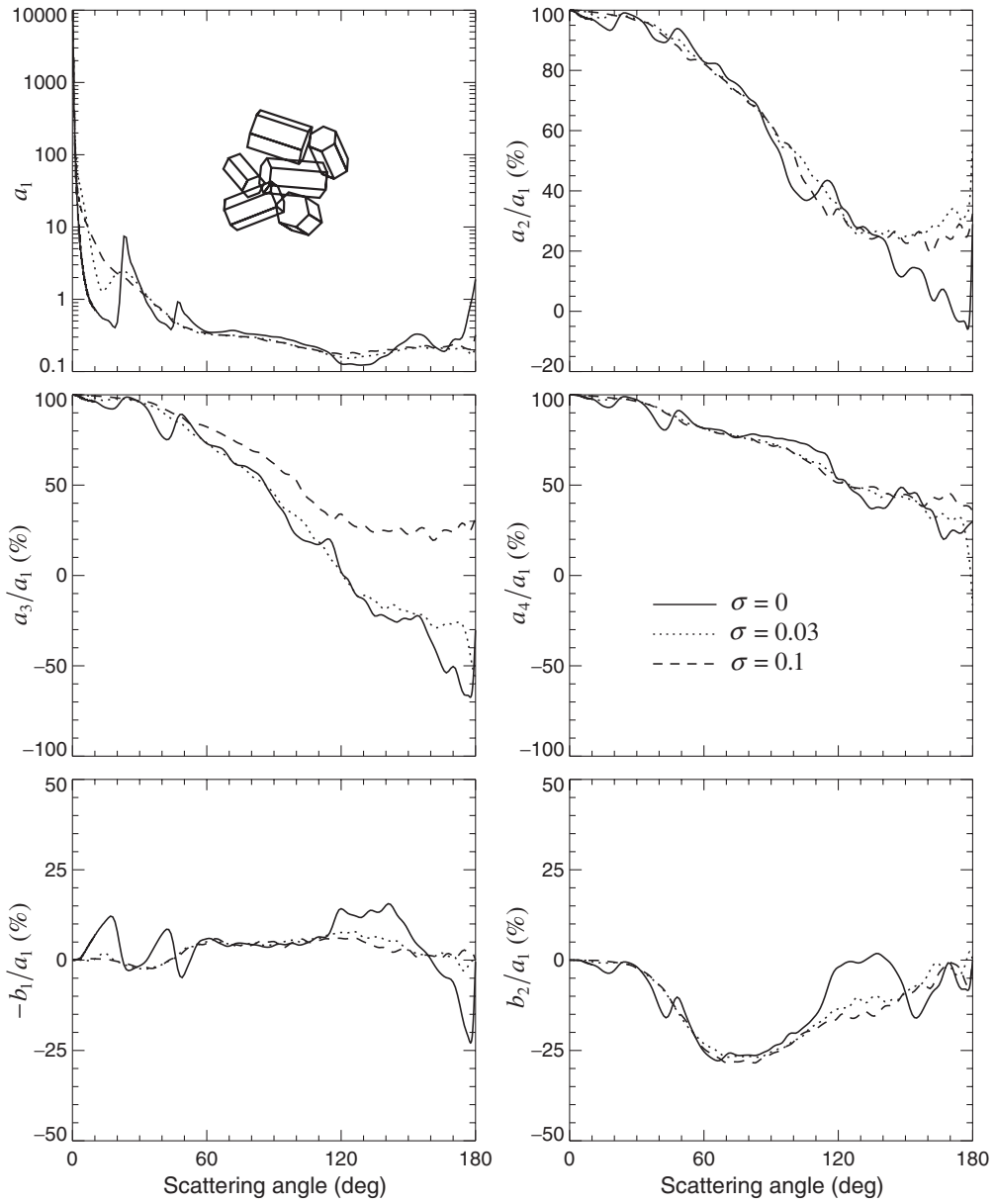

Figure 10.40. Elements of the normalized Stokes scattering matrix versus scattering angle for randomly oriented ice aggregates with smooth ($\sigma = 0$), moderately rough ($\sigma = 0.03$), and deeply rough ($\sigma = 0.1$) surfaces. The maximum dimension of the aggregates is 200 μm, the relative refractive index is 1.311, and the wavelength of light in the surrounding medium is 0.55 μm. (After Yang and Liou 1998a.)

tracing component of the phase function for large, randomly oriented, second-generation ice fractals with increasing distortion. The decrease in direct forward scattering occurs at the expense of an increase in the scattering into adjacent forward-scattering directions. Eventually the phase function becomes almost featureless and approaches a slope at side- and backscattering angles that stays almost constant with a

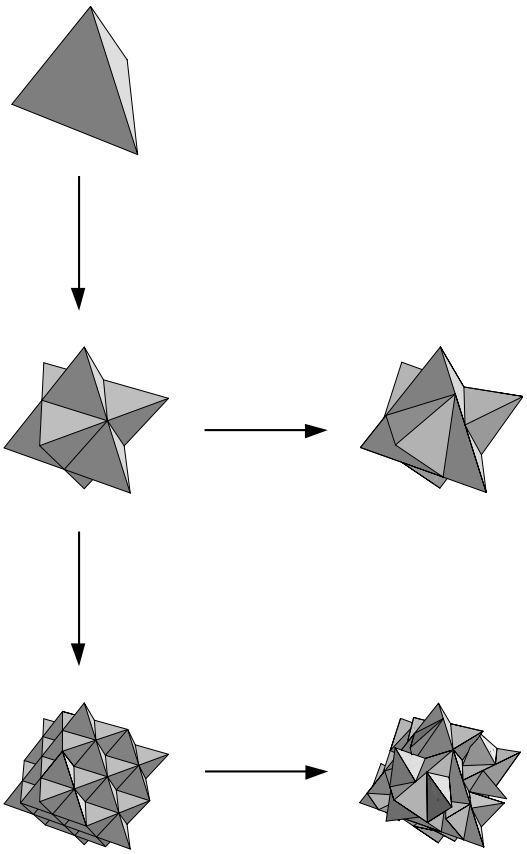

Figure 10.41. Deterministic (left-hand column) and randomized (right-hand column) triadic Koch fractals. Three generations are shown, the zeroth (top) to the second (bottom). (After Macke *et al*. 1996b).

further increase in distortion. This may imply that above a certain level of disorder, the phase function becomes essentially invariant against the particular realization of a random particle shape.

Figure 10.34 contrasts the phase functions computed for randomly oriented hexagonal ice crystals, random second-generation ice fractals with an 18% distortion, and spherical water droplets. The quantitative differences between these phase functions are so large that using an incorrect particle model in retrieval algorithms can seriously affect the results of cloud remote sensing (e.g., Mishchenko *et al.* 1996c; Yang *et al.* 2001b). The corresponding asymmetry parameter differences are relatively smaller: $\langle \cos\Theta \rangle = 0.816$ for the hexagonal ice columns, 0.752 for the random ice fractals, and 0.862 for the water droplets. However, the effect of particle shape on the albedo of

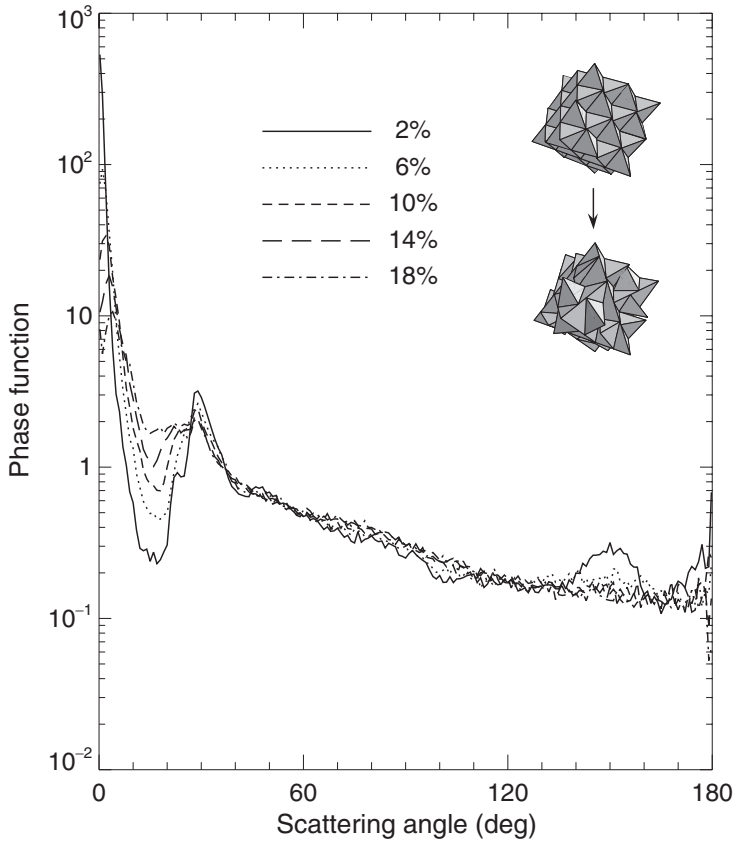

Figure 10.42. Ray-tracing phase function versus scattering angle for randomly oriented second-generation Koch fractals with increasing distortion. The relative refractive index is $m = 1.311$. (After Macke *et al*. 1996b.)

optically thick clouds and the associated radiative forcing of climate can be very strong (e.g., Stephens *et al.* 1990; Mishchenko *et al.* 1996c; Liou *et al.* 2000).

An interesting approach to modeling nearly spherical particles with random rough surfaces was introduced by Muinonen *et al.* (1996). The size and shape of their so-called Gaussian random spheres are specified by the mean and the covariance function of the radius vector. The covariance function is derived from the covariance function of the logarithmic radius, which is expanded in Legendre polynomials. The expansion coefficients are non-negative and provide the spectral weights of the corresponding spherical harmonic components in the Gaussian sphere. The zeroth-degree term controls the overall particle size. The first-degree term is mainly a translation: it moves the particle surface relative to the origin, but the shape itself does not change much. The second-order term produces a deformation with an elongated shape, while higher-degree terms create increasingly complex deformations with larger numbers of protuberances and hollows per solid angle. Increasing the variance of the radius enhances the protuberances and hollows radially. The scattering of light by Gaussian random spheres in the geometrical optics limit has been studied by Muinonen *et al.*

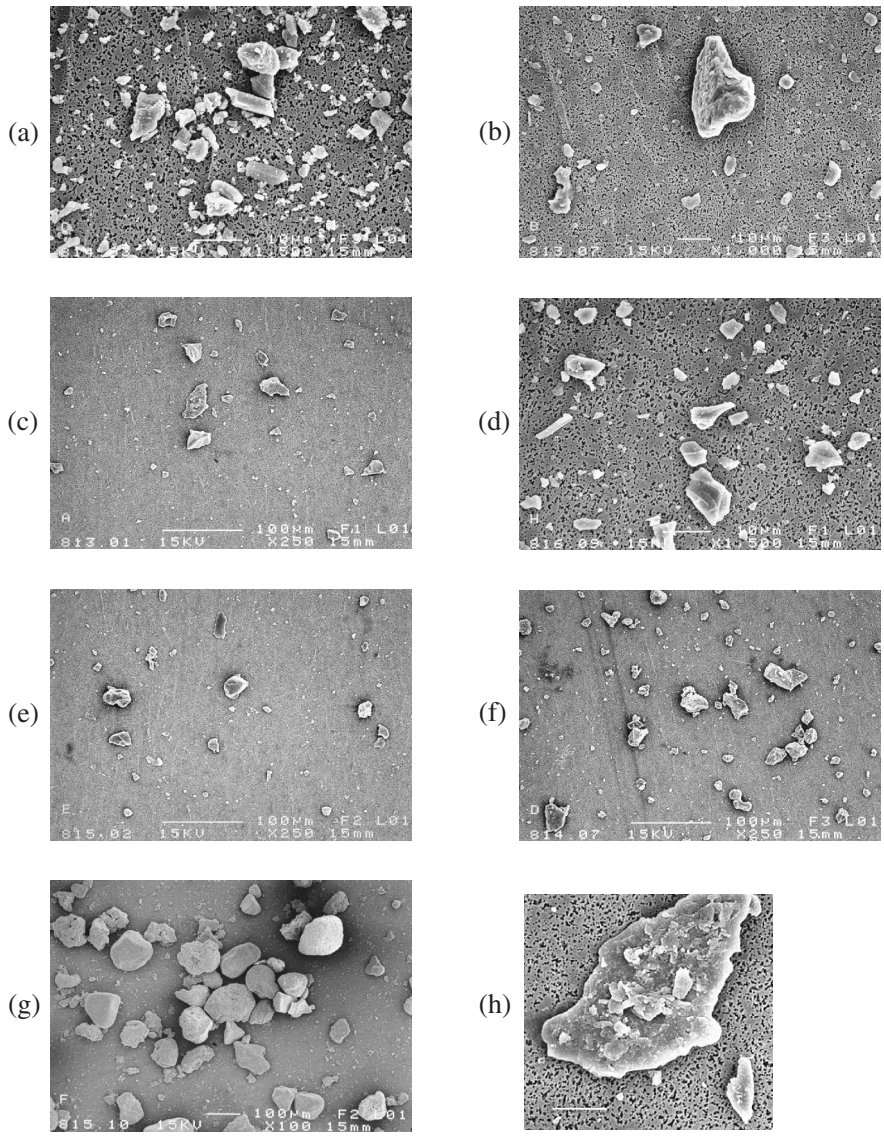

Figure 10.43. Scanning electron microscope images of seven aerosol samples: (a) feldspar, (b) red clay, (c) quartz, (d) Pinatubo volcanic ash, (e) loess, (f) Lokon volcanic ash, and (g) Sahara sand. Panel (h) demonstrates the irregularity of a single quartz particle. The length of the white bars corresponds to 10 μm in panels (a), (b), (d), and (h) and to 100 μm in the remaining panels. (From Volten *et al.* 2001.)

(1996) and Nousiainen and Muinonen (1999) (see also the review by Muinonen 2000).

Despite the recent progress in theoretical modeling, laboratory and *in situ* measurements remain a major source of information about light scattering by irregular particles. Besides the widely acclaimed study by Perry *et al.* (1978), a unique body of experimental data has been collected using the advanced laboratory setup developed at the Free University in Amsterdam (Kuik *et al.* 1991; Kuik 1992; Volten *et al.* 1998,

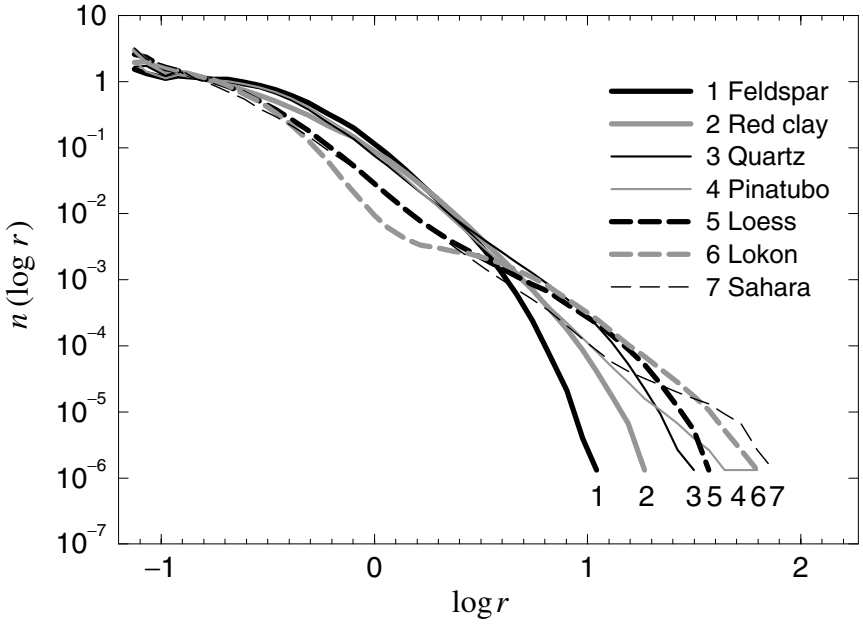

Figure 10.44. Measured normalized size distributions $n(\log r) = rn(r)\ln 10$ of the projected-area-equivalent-sphere radius r for the seven aerosol samples shown in Fig. 10.43. (From Volten *et al.* 2001.)

1999, 2001; Vermeulen 1999; Hovenier 2000; Muñoz *et al.* 2000a, b, 2001; Volten 2001). For example, Fig. 10.43 shows microphotographs of seven mineral aerosol samples studied by Volten *et al.* (2001), while Fig. 10.44 depicts the respective normalized distributions of projected-area-equivalent-sphere radii (in micrometers). It is evident that all particles studied have irregular and strongly variable compact shapes. Table 10.4 provides a brief characterization of the samples including the corresponding effective radii and approximate ranges of the real part of the relative refractive index based on the literature values for the main constituent minerals. The results of measurements at the wavelengths 632.8 and 441.6 nm are shown in Figs. 10.45–10.51. The phase functions are normalized to unity at $\Theta = 30°$. Other elements of the normalized Stokes scattering matrix are shown relative to the corresponding phase function. The measurements were taken at $5°$ intervals for Θ in the range from $5°$ to $170°$ and at $1°$ intervals for Θ from $170°$ to $173°$. Scattering matrix elements other than those shown in these figures were found to be zero within the error bars, which was a good indication that the particles formed a macroscopically isotropic and mirror-symmetric scattering medium.

The phase functions for all samples studied are smooth functions of the scattering angle and exhibit a steep forward peak and essentially no structure at side- and backscattering angles. Most of the phase-function curves are remarkably shallow at side-scattering angles (cf. Perry *et al.* 1978; Nakajima *et al.* 1989; Muñoz *et al.* 2000a) and do not show the deep side-scattering minimum typical of spherical particles, caused

Table 10.4. Characteristics of seven mineral particle samples studied by Volten *et al.* (2001)

Sample	Composition	r_{eff} (μm)	m_{R}	Color
Feldspar	K-feldspar, plagioclase, quartz	1.0	1.5–1.6	light pink
Red clay	biotite, illite, quartz	1.5	1.5–1.7	red brown
Quartz	quartz	2.3	1.54	white
Pinatubo volcanic ash	glass, plagioclase, amphibole, magnetite	3.0	1.5–1.7 2.1	light gray
Loess	K-feldspar, illite, quartz, calcite, chlorite, albite	3.9	1.5–1.7	yellow brown
Lokon volcanic ash	silica glass, plagioclase, magnetite	7.1	1.5–1.6 2.1	dark brown
Sahara sand	quartz, clay minerals, calcium carbonate	8.2	1.5–1.7	yellow brown

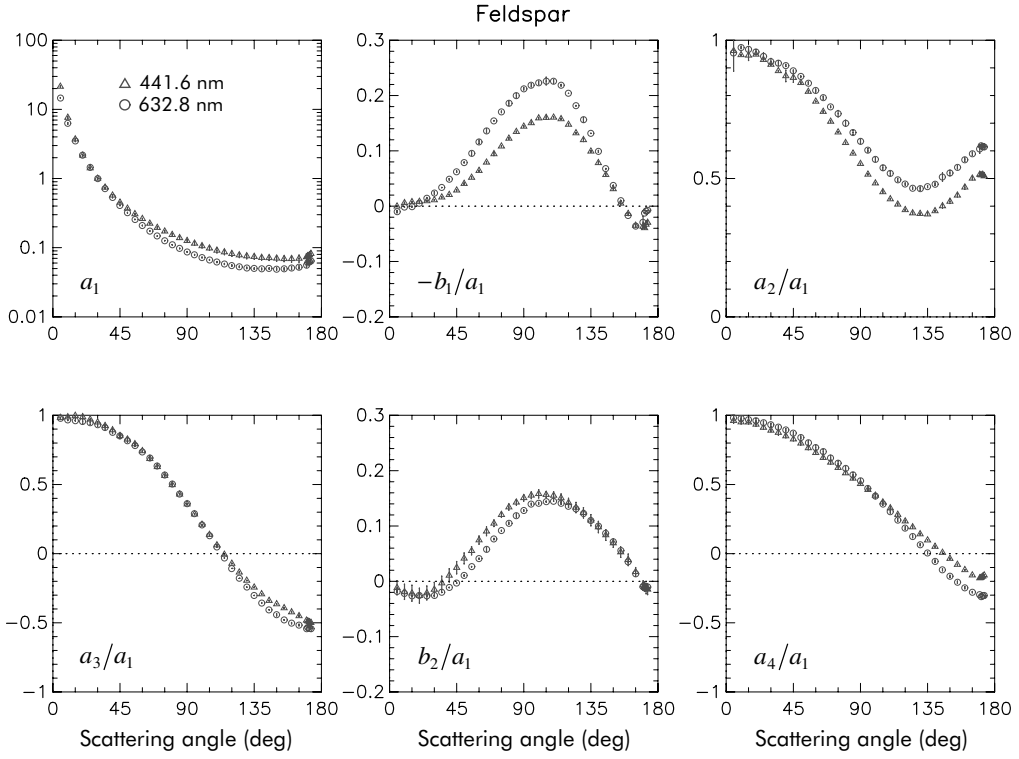

Figure 10.45. The phase function a_1 and the scattering matrix element ratios $-b_1/a_1$, a_2/a_1, a_3/a_1, b_2/a_1, and a_4/a_1 versus scattering angle Θ for feldspar. The circles and triangles denote measurements at wavelengths 632.8 and 441.6 nm, respectively, together with their error bars. The phase functions are normalized to unity at $\Theta = 30°$. The sign of the ratio b_2/a_1 is opposite to that adopted elsewhere in this book. (From Volten *et al.* 2001.)

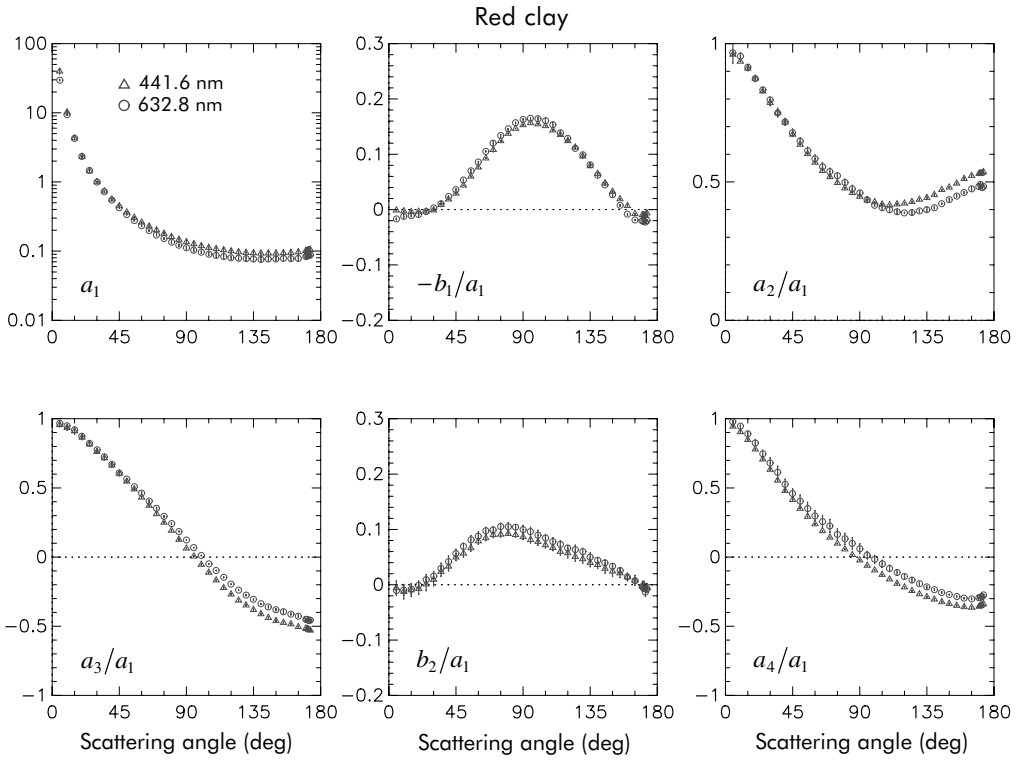

Figure 10.46. As in Fig. 10.45, but for red clay (from Volten *et al*. 2001).

by the Alexander's dark band lying between the primary and secondary rainbows (cf. Fig. 7.4 and Section 9.4). Some of the phase-function curves seem to show the beginning of a backscattering enhancement, but the lack of measurements for $\Theta > 173°$ makes this observation inconclusive. The curves for the ratio $-b_1/a_1$ are also similar for all samples and display a broad positive maximum at side-scattering angles and a weak and narrow negative branch at backscattering angles. The curves for the ratio a_2/a_1 are remarkably similar as well and deviate significantly from unity at side- and backscattering angles: they descend from almost unity at small scattering angles to a minimum at scattering angles close to $120°-130°$ and then increase again as Θ approaches 180°. The depth of the minimum appears to be size dependent and increases as the effective radius grows from 1.0 μm for feldspar to 8.2 μm for Sahara sand. The curves for the ratios a_3/a_1 and a_4/a_1 are largely featureless and deviate significantly from –1 at backscattering angles. The ratio a_4/a_1 is always larger than the ratio a_3/a_1 in the backward hemisphere. Volten *et al.* (2001) use the time factor $\exp(\mathrm{i}\omega t)$ rather than $\exp(-\mathrm{i}\omega t)$ to define the Stokes parameters, which causes a sign change in the numerical values of the ratio b_2/a_1 (cf. Mishchenko *et al.* 2000b). Therefore, in terms of the time-factor convention adopted in this book, the results of Volten *et al.* show that this ratio typically has weak positive branches at small and large scattering angles separated by a wide range of negative values. Most of these observations are in qualitative agreement with the conclusions derived from the *T*-

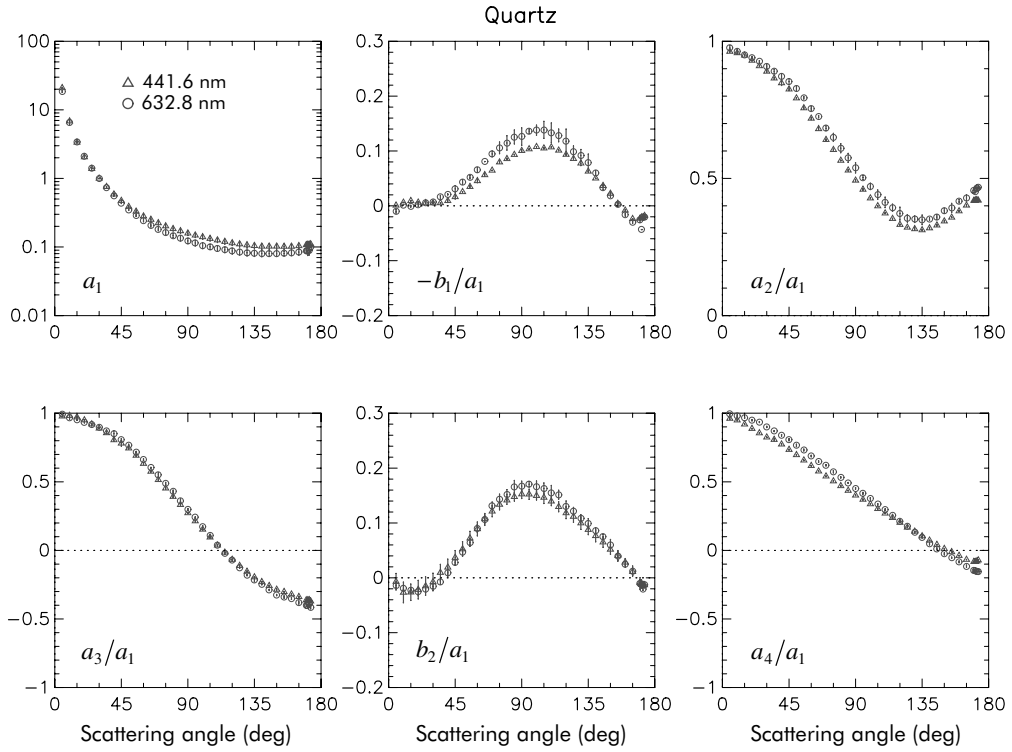

Figure 10.47. As in Fig. 10.45, but for quartz (from Volten *et al*. 2001).

matrix results for moderately aspherical polydisperse spheroids and cylinders as discussed in Sections 10.2 and 10.3.

The similarity of the laboratory results for the different mineral-particle samples prompted Volten *et al.* (2001) to construct an average scattering matrix for use in qualitative or semi-quantitative analyses of remote sensing observations or laboratory and *in situ* measurements, especially in those cases when the specific microphysical characteristics of mineral particles are not known *a priori*. The average phase function was calculated by averaging the 14 phase functions measured at both wavelengths. Since no scattering cross sections were available, the experimental phase functions were averaged by giving them equal weights. Therefore, the normalization to unity at $\Theta = 30°$ also holds for the average phase function. Each measured element ratio was multiplied by the normalized phase function measured for the particular sample and wavelength, thereby yielding elements instead of element ratios. Finally, each element was averaged over the respective 14 measurements and divided by the average phase function. The resulting average phase function and element ratios are depicted in Fig. 10.52. For comparison, this figure also shows the bands of sample variability, defined as the areas between the highest and lowest measured values in Figs. 10.45–10.51 not taking into account the error bars for the individual measurements. The laboratory data displayed in Figs. (10.45)–(10.52) were presented by Volten (2001) in tabular form and will undoubtedly prove very useful in future

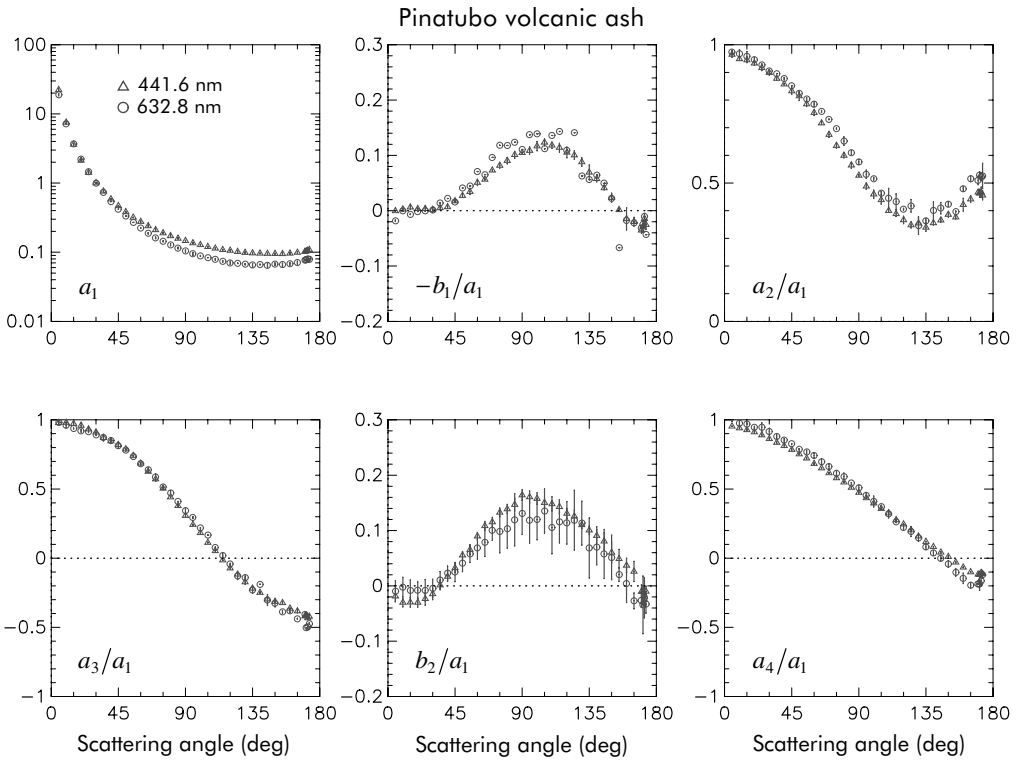

Figure 10.48. As in Fig. 10.45, but for Pinatubo volcanic ash (from Volten *et al*. 2001).

analyses of light scattering by irregular particles. For example, the laboratory data for green clay particles with an effective radius of 1.55 μm (Muñoz *et al.* 2000b) generally agree with the overall trends exhibited by the average scattering matrix elements and fall within the bands of sample variability (Fig 10.53). This comparison suggests that the average model derived by Volten *et al.* (2001) may indeed be representative of ensembles of irregular, compact mineral particles with sizes comparable to and larger than a wavelength.

10.8 Statistical approach

Since theoretical computations for irregular particles with sizes comparable to the wavelength remain problematic, several attempts have been made to model the scattering and absorption properties of irregular particles using simple, regular shapes. These attempts are based on the realization that in addition to size and orientation averaging, as discussed in Section 10.1, averaging over shapes may also prove to be necessary in many cases. More often than not, natural and artificial particle samples exhibit a great variety of shapes, thereby making questionable the ability of a single nonspherical shape to represent scattering properties of a shape mixture. We have

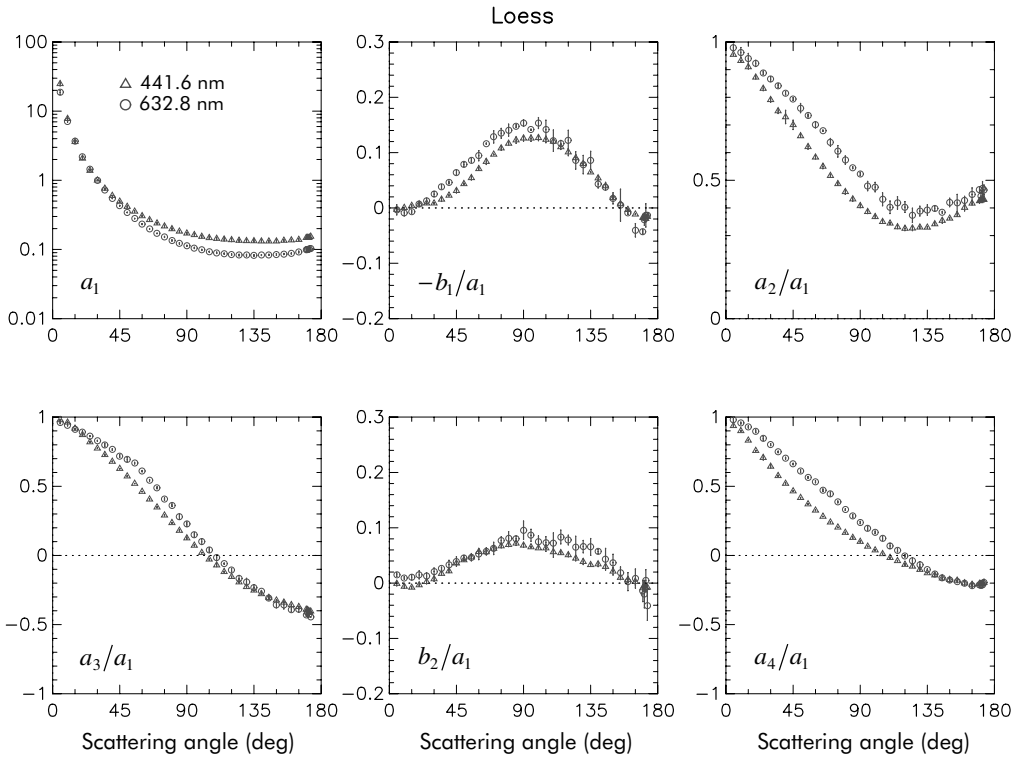

Figure 10.49. As in Fig. 10.45, but for loess (from Volten *et al*. 2001).

seen, indeed, that even after size and orientation averaging, essentially any deterministic particle shape produces a unique, shape-specific scattering pattern, whereas experimental measurements for real nonspherical particles usually show smooth, featureless patterns. As an example, Plate 10.7(a) depicts the phase function for a monodisperse sphere with radius 1.163 μm and surface-equivalent, monodisperse, randomly oriented prolate spheroids with aspect ratios ε increasing from 1.2 to 2.4. The wavelength of the light in the surrounding medium is 0.443 μm, and the relative refractive index is 1.53 + i0.008. Whereas the monodisperse curves form a tangle of lines with no clear message, averaging over sizes, as shown in Plate 10.7(b), makes the phase functions much smoother and reveals a systematic change with increasing aspect ratio that renders each phase-function curve unique and dissimilar to all other curves. However, this uniqueness is suppressed and ultimately removed by averaging over an increasingly wide aspect-ratio distribution of prolate spheroids, centered on $\varepsilon = 1.8$, Plate 10.7(c), and by a subsequent mixing of prolate and oblate spheroids, Plate 10.7(d). The resulting phase function (the red curve in Plate 10.7(d)) is very smooth and featureless and, in fact, almost perfectly coincides with the phase function experimentally measured by Jaggard *et al.* (1981) for micrometer-sized, irregularly shaped soil particles (cf. Fig. 10.54). Both phase functions show the typical en-

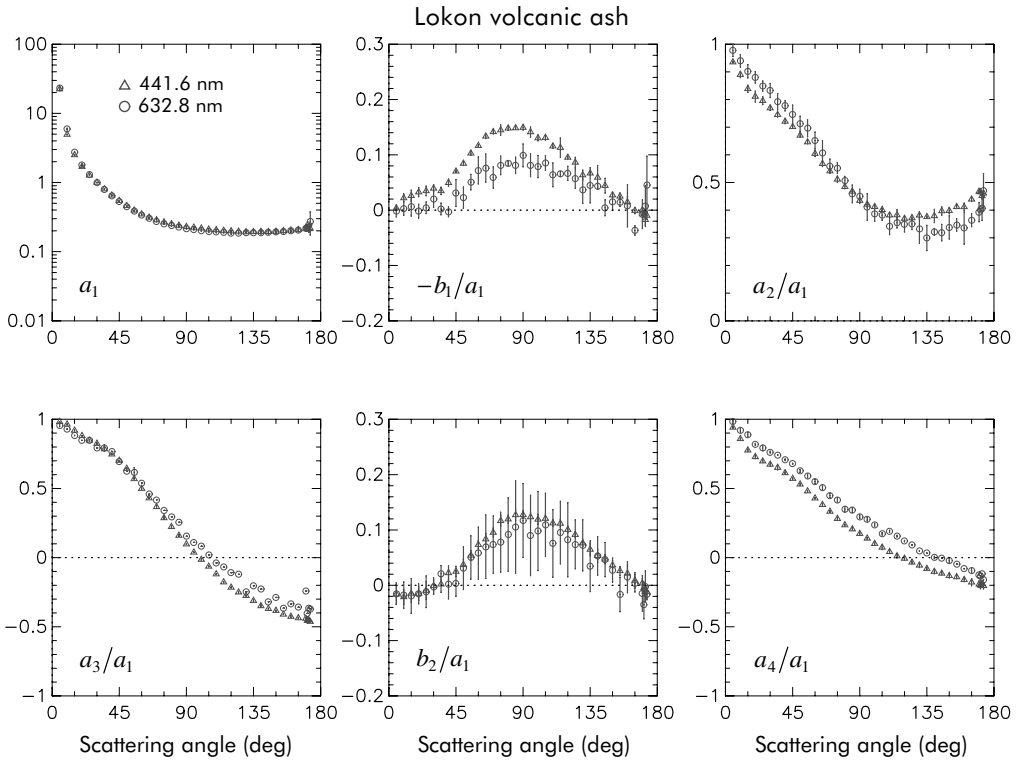

Figure 10.50. As in Fig. 10.45, but for Locon volcanic ash (from Volten *et al*. 2001).

hancement of side scattering and suppression of backscattering relative to the phase function for surface-equivalent spheres.

This example may have two important implications. First, it may indicate that the often observed smooth scattering-angle dependence of the elements of the scattering matrix for samples of natural and artificial nonspherical particles is largely caused by the diversity of particle shapes in the samples. Second, it may suggest that at least some scattering properties of ensembles of irregular particles can be adequately modeled using a polydisperse shape mixture of simple particles such as spheroids. The assumptions that particles chosen for the purposes of ensemble averaging need not be in one-to-one correspondence with the ensemble of irregular particles of interest and that they may have relatively simple shapes are central to the so-called statistical approach (Shifrin and Mikulinsky 1987; Mugnai and Wiscombe 1989; Bohren and Singham 1991). The need for this kind of approach stems from the fact that it is often impossible to specify exactly the shapes and sizes of all particles forming a natural or artificial sample. Even if it were possible, the low efficiency of the exact numerical techniques applicable to arbitrarily shaped particles would entail a prohibitively expensive computational effort. However, the availability of techniques like the *T*-matrix method, which is very fast for randomly oriented, rotationally symmetric particles and is applicable to large size parameters, makes the statistical approach feasible. Applications of this approach by Bohren and

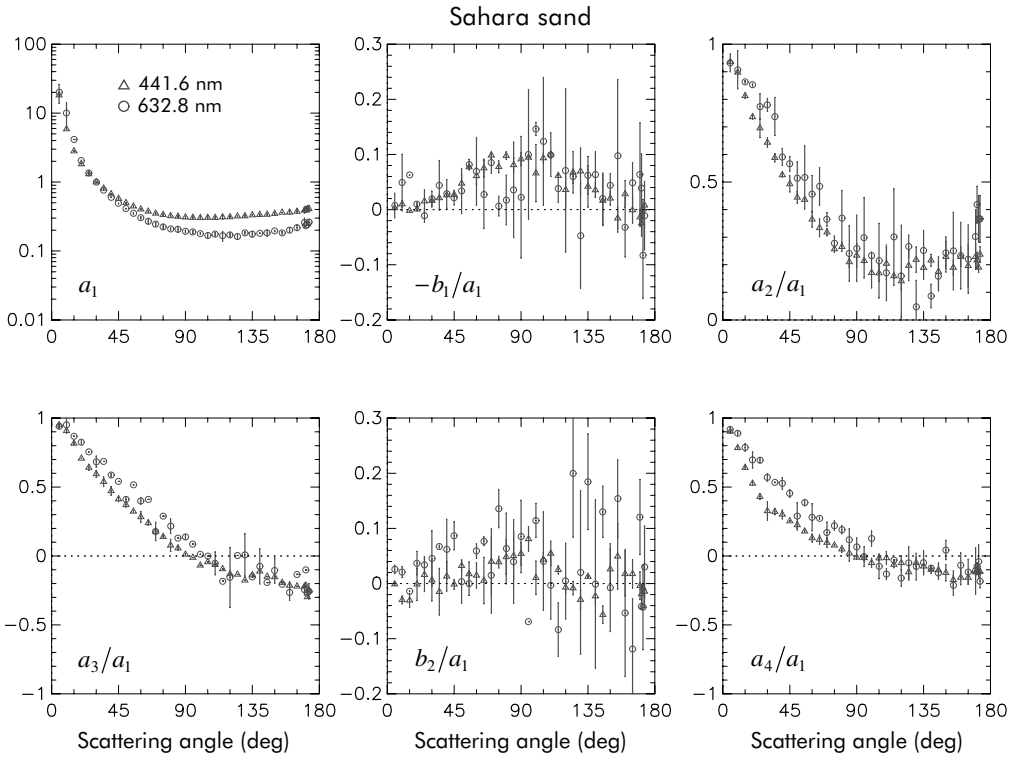

Figure 10.51. As in Fig. 10.45, but for Sahara sand (from Volten *et al*. 2001).

Huffman (1983, Chapter 12), Nevitt and Bohren (1984), Hill *et al.* (1984), Mishchenko *et al.* (1997a), and Goncharenko *et al.* (1999) suggest that it may indeed be a valuable practical tool in many cases.

10.9 Clusters of spheres

The scattering and absorption properties of simple two-sphere clusters (bispheres) have been extensively studied by Mishchenko *et al.* (1995) using the superposition *T*-matrix method. Panels (b) and (c) of Plate 10.8 depict the degree of linear polarization for scattering of unpolarized incident light, i.e., the ratio

$$-\frac{Z_{21}(\vartheta^{\rm sca},\,\varphi^{\rm sca}=0;\,\vartheta^{\rm inc}=0,\,\varphi^{\rm inc}=0)}{Z_{11}(\vartheta^{\rm sca},\,\varphi^{\rm sca}=0;\,\vartheta^{\rm inc}=0,\varphi^{\rm inc}=0)},$$

as a function of the zenith angle of the scattering direction and the monodisperse constituent-sphere size parameter for two orientations of the bisphere axis with respect to the laboratory reference frame. The bispheres have identical touching components, and the bisphere axis is defined as the line connecting the constituent-sphere centers. These plots show that the bisphere polarization is strongly dependent on the particle

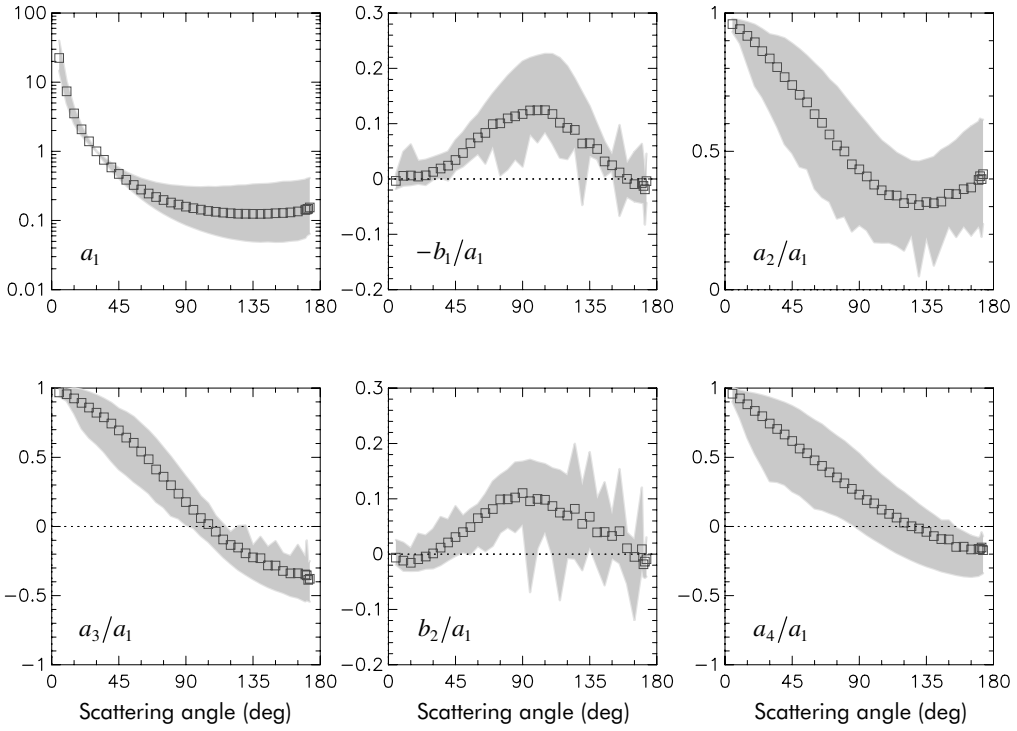

Figure 10.52. The squares show the average phase function a_1 (normalized to unity at $\Theta = 30°$) and the scattering matrix element ratios $-b_1/a_1$, a_2/a_1, a_3/a_1, b_2/a_1, and a_4/a_1 versus scattering angle Θ. The gray bands indicate the domains spanned by the measurements for individual particle samples. The sign of the ratio b_2/a_1 is opposite to that adopted elsewhere in this book. (From Volten *et al*. 2001.)

orientation and reveals a much more complicated structure than the single-sphere polarization pattern shown in Plate 10.8(a). In particular, the lack of axial symmetry for the scattering geometry in Plate 10.8(c) makes the linear polarization non-zero at $\vartheta^{\rm sca} = 0°$ and, more noticeably, at $\vartheta^{\rm sca} = 180°$. Also, the number of local maxima and minima has increased sharply. This means that in addition to the single-sphere resonant structure the bispheres exhibit a significant contribution due to the cooperative scattering of light from the two constituent spheres.

Plate 10.8(d) shows the calculation results for monodisperse bispheres in random orientation. Somewhat unexpectedly, we see a polarization pattern that is strikingly similar to that of single monodisperse spheres, Plate 10.8(a). The only obvious difference is that the amplitudes of the local maxima and minima are reduced, although their locations and numbers are exactly the same. This means that averaging over bisphere orientations largely cancels the cooperative scattering contribution and slightly blurs the single-sphere resonant structure. This result is well illustrated by Fig. 10.55, which shows the elements of the normalized Stokes scattering matrix for a randomly oriented two-sphere cluster with identical touching components, together with those for a single sphere with size parameter equal to that of the cluster compo-

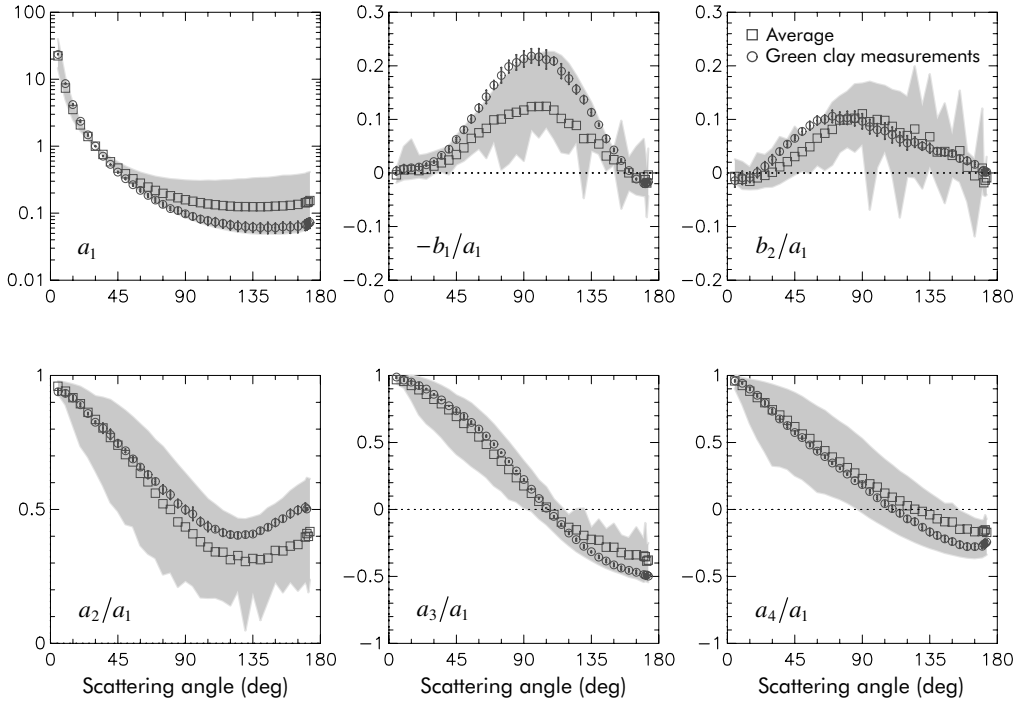

Figure 10.53. The circles depict the measured phase function a_1 and scattering matrix element ratios $-b_1/a_1$, b_2/a_1, a_2/a_1, a_3/a_1, and a_4/a_1 versus scattering angle for green clay particles at a wavelength 633 nm (from Muñoz *et al.* 2000b). The squares and the gray bands indicate the average scattering matrix and the domains spanned by the measurements for seven mineral particle samples (Volten *et al.* 2001).

nents for comparison. It is obvious that the dominant feature in the cluster scattering is the single scattering from the component spheres, albeit diminished by orientation averaging. The only distinct manifestations of the fact that the bisphere is a nonspherical particle are the departure of the ratio a_2/a_1 from unity and the detectable lack of equality of the elements a_3 and a_4. These two effects are especially noticeable at backscattering angles and are further illustrated in Fig. 10.56, which shows the linear and circular depolarization ratios for randomly oriented bispheres with touching components as a function of the component-sphere size parameter. Both depolarization ratios vanish in the limit of zero size parameter, but become appreciable for $x \gtrsim 1$ and reach especially large values at size parameters from about 15 to 20.

Figures 10.57 and 10.58 show ratios of bisphere and single-sphere quantities: the optical cross sections, the single-scattering albedo, and the asymmetry parameter. The bispheres are randomly oriented and the size of the single sphere is equal to the size of each bisphere component. Interestingly, all these ratios are nearly constant at size parameters exceeding 15. The ratio of the extinction cross sections (the solid curve in Fig. 10.57) shows both high-frequency ripple and low-frequency oscillations. However, the amplitude of the oscillations is small, and the entire curve for size parameters exceeding

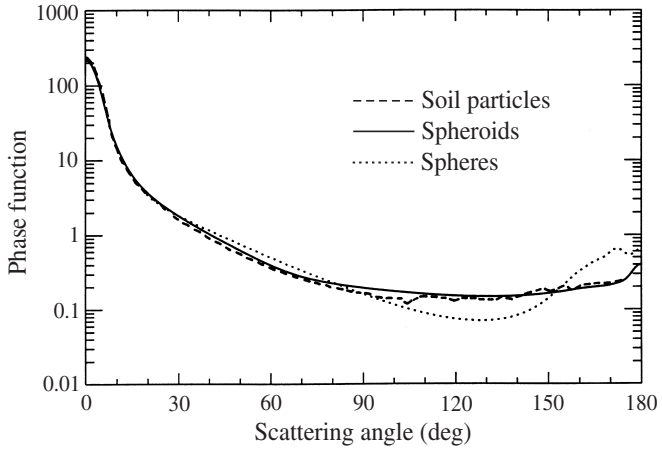

Figure 10.54. Phase functions measured by Jaggard *et al.* (1981) for natural wavelength-sized soil particles and computed for a broad shape distribution of polydisperse, randomly oriented spheroids and surface-equivalent spheres.

6 is close to 1.8–1.85. The ratio of the orientation-averaged geometrical cross section of a bisphere to the geometrical cross section of a sphere with size equal to that of each bisphere component is 1.849. Therefore, in the geometrical optics limit the ratio of the bisphere and single-sphere extinction cross sections must be equal to this value, 1.849. It can be seen that the extinction ratio curve shows a distinct trend toward this limit with increasing size parameter. However, it is interesting that the extinction ratio is close to the geometrical optics limit for size parameters as small as 7.

Despite a small-amplitude high-frequency ripple, the ratio of the absorption cross sections (the broken-and-dotted curve in Fig. 10.57) is close to 2 for the entire range of size parameters shown, thus indicating that the absorption cross section is roughly proportional to the particle volume. However, if the imaginary part of the relative refractive index is non-zero then in the limit of infinite size parameter all light refracted into the particle is absorbed and does not escape. Therefore we should expect that the ratio of the absorption cross sections should decrease with increasing size parameter and approach the geometrical cross section ratio of 1.849, as seen indeed in Fig. 10.57. The scattering cross section ratio (the dotted curve in Fig. 10.57) closely follows the extinction cross section ratio except at size parameters smaller than unity, where extinction is dominated by absorption.

The single-scattering albedo ratio (the dotted curve in Fig. 10.58) is especially size-parameter independent for size parameters greater than unity and varies within a very narrow range, 1 ± 0.02. The asymmetry parameter ratio (the solid curve in Fig. 10.58) is also close to unity. However, all these ratios, except for the absorption cross section ratio, rise substantially as the size parameter becomes smaller than 2, which demonstrates the increasing influence of cooperative scattering effects for smaller particles.

As we have seen previously, one of the main effects of averaging scattering

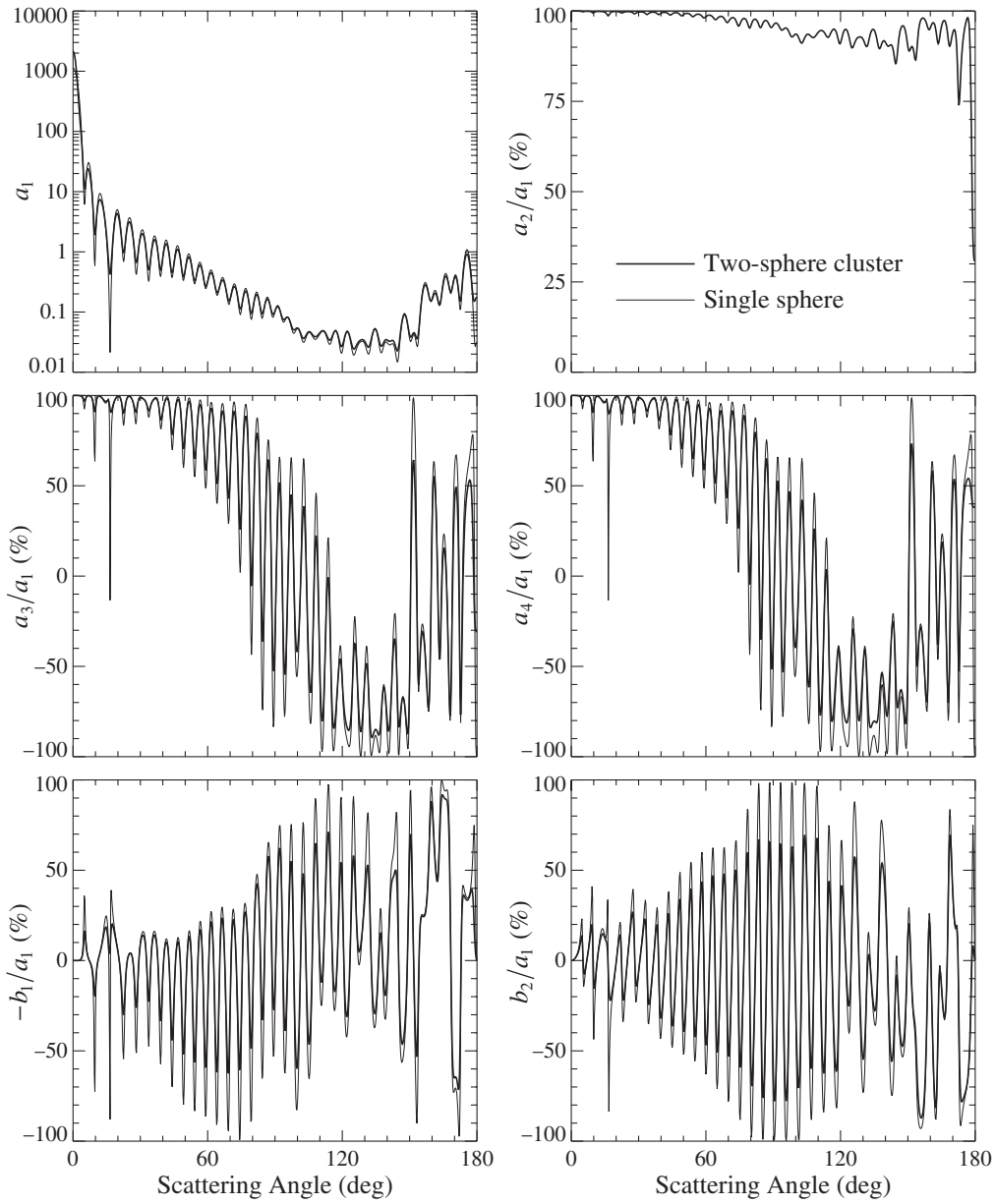

Figure 10.55. Scattering matrix elements for a randomly oriented two-sphere cluster with touching components and a single sphere. The component spheres and the single sphere have the same size parameter 40 and the same relative refractive index 1.5 + i0.005.

characteristics over a size distribution is to wash out the resonance structure typical of monodisperse particles. This effect facilitates comparisons of light-scattering properties of particles with different shapes and is illustrated in Fig. 10.59, which shows the elements of the normalized Stokes scattering matrix for power law size distributions of spheres and of randomly oriented bispheres. This figure demonstrates again that the angular dependence of the elements of the scattering matrix for bispheres is similar to that for single spheres with effective size parameter equal to the effective

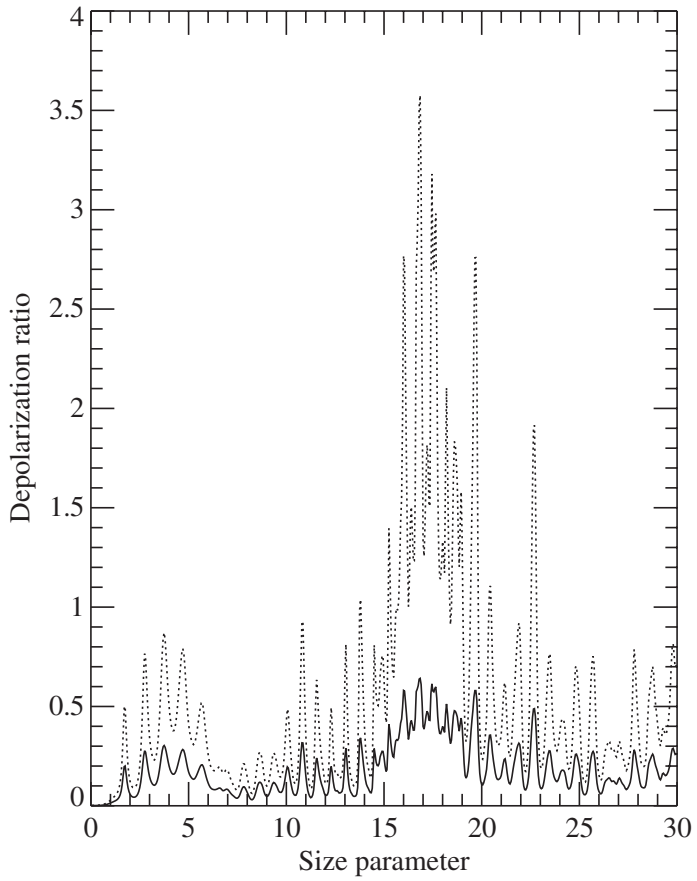

Figure 10.56. Linear (solid curve) and circular (dotted curve) backscattering depolarization ratios versus constituent-sphere size parameter for randomly oriented monodisperse bispheres with equal touching components and a relative refractive index 1.5 + i0.005.

bisphere monomer size parameter. The ratios $-b_1/a_1$ and b_2/a_1 for the bispheres and the single spheres are especially similar. The phase functions a_1 are also close to one another except at scattering angles smaller than 10°, where the bisphere intensity is nearly twice that for single spheres because of the constructive interference of light singly scattered by bisphere components in the exact forward direction (Mishchenko 1996a). Again, the only unequivocal indications of particle nonsphericity for bispheres are the differences between the ratios a_3/a_1 and a_4/a_1 and the departure of the ratio a_2/a_1 from unity. For comparison, Fig. 10.59 also depicts the scattering matrix elements for polydisperse, randomly oriented prolate spheroids with aspect ratio 2 and effective volume-equivalent-sphere size parameter 10. It is seen that, unlike the case for the spheres and the bispheres, the spheroid phase function exhibits enhanced side scattering and suppressed backscattering, while the degree of linear polarization is positive at scattering angles around 120°. The differences between the ratios a_2/a_1, a_3/a_1, a_4/a_1, and b_2/a_1 for the spheres and the spheroids are also greater than those for the spheres and the bispheres.

Figures 10.60 and 10.61 depict the scattering matrix elements for two distinctly

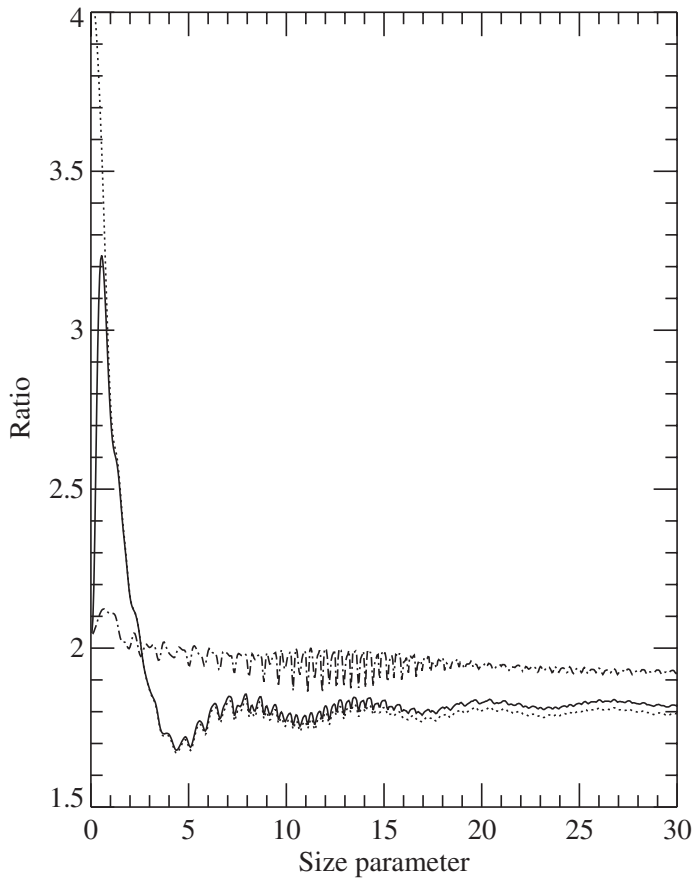

Figure 10.57. Ratios of extinction (solid curve), scattering (dotted curve), and absorption (broken-and-dotted curve) cross sections for monodisperse randomly oriented bispheres with equal touching components and for monodisperse single spheres, versus single-sphere size parameter. For bispheres, the horizontal axis shows the values of the constituent-sphere size parameter. The relative refractive index is 1.5 + i0.005.

different types of sphere cluster, each with N_s identical wavelength-sized components, for $N_s = 1, 2, 3, 4, \text{or } 5$. In Fig. 10.60 the cluster is a straight chain whereas in Fig. 10.61 the spheres are packed into a tetrahedral lattice. These two types of clusters represent extrema in the packing density of touching spheres. A quick inspection of the figures reveals that the configuration of the component spheres can have a significant effect on the cluster scattering properties. Aside from the increase in the forward-scattering value of the phase function caused by the constructive interference of the light singly scattered by the cluster components in the exact forward direction, the matrix elements for the straight chain (Fig. 10.60) attain a form that is nearly independent of N_s for $N_s \geq 2$. As for bispheres, clustering results in a damping of the oscillations in the matrix elements compared with those for a single sphere, yet the locations of the maxima and minima for the chain are essentially the same as those for the single-sphere case. The obvious exception is the ratio a_2/a_1, which is identically unity for the sphere. However, the matrix elements for the densely packed cluster

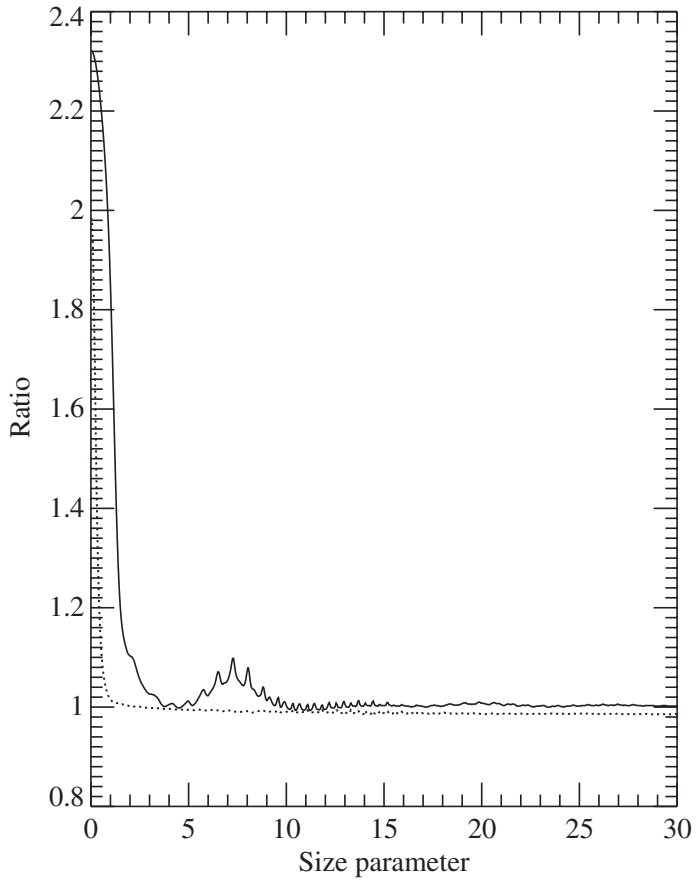

Figure 10.58. As in Fig. 10.57, but for the ratios of the single-scattering albedos (dotted curve) and of the asymmetry parameters (solid curve).

change significantly with increasing N_s and appear to approach a saturation level in which all oscillations eventually vanish. The effect of packing density is especially noticeable in the backward-direction values of the ratios a_2/a_1, a_3/a_1, and a_4/a_1 and, thus, in increased linear and circular depolarization ratios.

To explain the differences in the scattering patterns for these two types of cluster configuration, we first note that the two major effects of aggregation on scattering are interference of the fields scattered by the cluster components in the far-field zone and multiple internal scattering among the components. When the size parameters of the spheres are of order unity or greater (as is the case for Figs. 10.60 and 10.61), averaging over a uniform orientation distribution acts to zero out the effect of interference in all directions but the exact forward direction. The differences between the single-sphere and orientation-averaged cluster scattering patterns are therefore caused mostly by multiple scattering. Multiple scattering for the linear chain configuration occurs primarily between neighboring spheres, and because of this the scattering matrix elements for $N_s \geq 3$ do not differ much from those of the bisphere – except for the phase function at $\Theta = 0°$. However, the packed-cluster configuration offers a

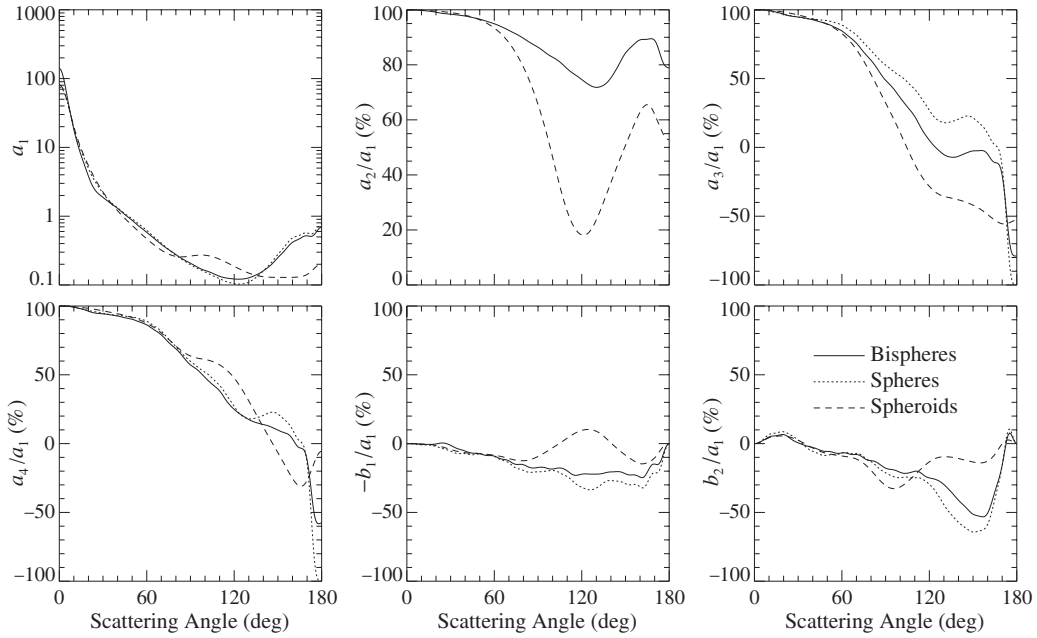

Figure 10.59. Elements of the normalized Stokes scattering matrix for polydisperse randomly oriented bispheres with equal touching components and effective constituent-sphere size parameter $x_{\text{eff}} = 10$ and for polydisperse single spheres with the same effective size parameter. For comparison, the figure also shows the results for polydisperse, randomly oriented prolate spheroids with aspect ratio 2 and effective volume-equivalent-sphere size parameter 10. The relative refractive index is 1.5 + i0.005 and the size distribution is given by Eq. (5.244) with an effective variance $v_{\text{eff}} = 0.2$.

much greater opportunity for multiple scattering among all the spheres forming the cluster and results in stronger differences between the single-sphere and random-orientation-cluster elements of the scattering matrix.

Based on the results for linear chains of spheres, we may expect that scattering patterns for low-density aggregates of wavelength-sized particles look similar to those for bispheres. This is indeed demonstrated by the laboratory data measured by Muñoz *et al.* (2000b, 2001) for a sample of fly ash aerosols (fluffy aggregates composed of nearly spherical inorganic particles; see Fig. 10.62). Figure 10.63 shows that the normalized scattering matrix for this sample is distinctly different from the average scattering matrix for compact irregular particles derived by Volten *et al.* (2001) (see Section 10.7). Moreover, the experimental results depicted in Fig. 10.63 appear to be remarkably similar to the results of theoretical computations displayed in Fig. 10.59. In particular, the phase function of fly ash particles has the deep side-scattering minimum typical of single spheres and bispheres, the ratios a_3/a_1 and a_4/a_1 tend to values close to –1 as the scattering angle approaches 180°, and the ratio a_2/a_1 is closer to unity than that for compact nonspherical particles. Also, the ratios $-b_1/a_1$ and b_2/a_1 for fly ash and compact irregular particles are qualitatively similar to those computed for polydisperse bispheres and spheroids, respectively.

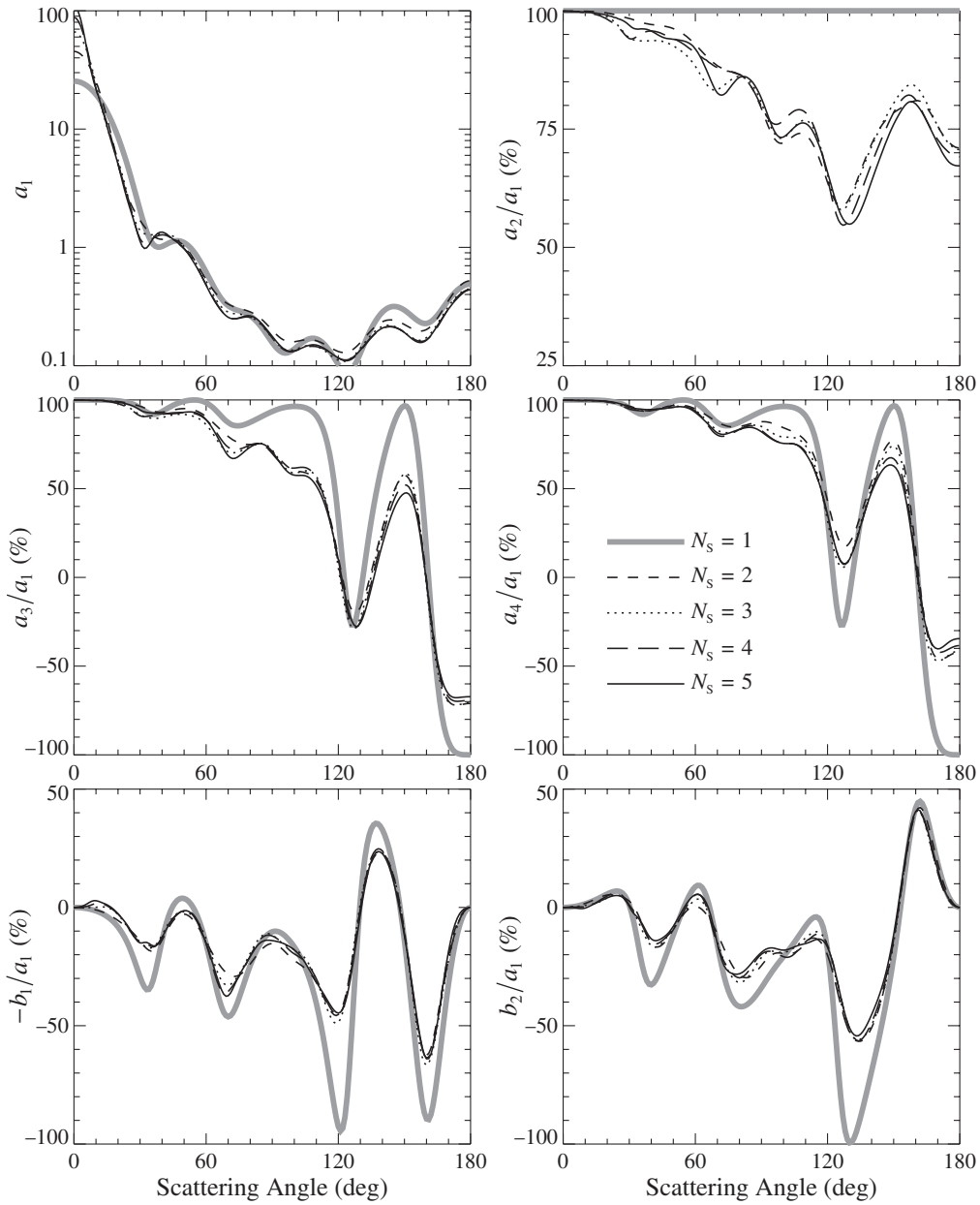

Figure 10.60. Orientation-averaged scattering matrix elements for linear chains of N_s equal spheres. The component-sphere size parameter is 5 and the relative refractive index is 1.5 + i0.005. (After Mackowski and Mishchenko 1996.)

Since clusters of small monomers are abundant in various natural and artificial environments, cluster optics is an important and active area of research. Detailed information and further references can be found in the reviews by Fuller and Mackowski (2000) and Sorensen (2001) and the book edited by Markel and George (2001).

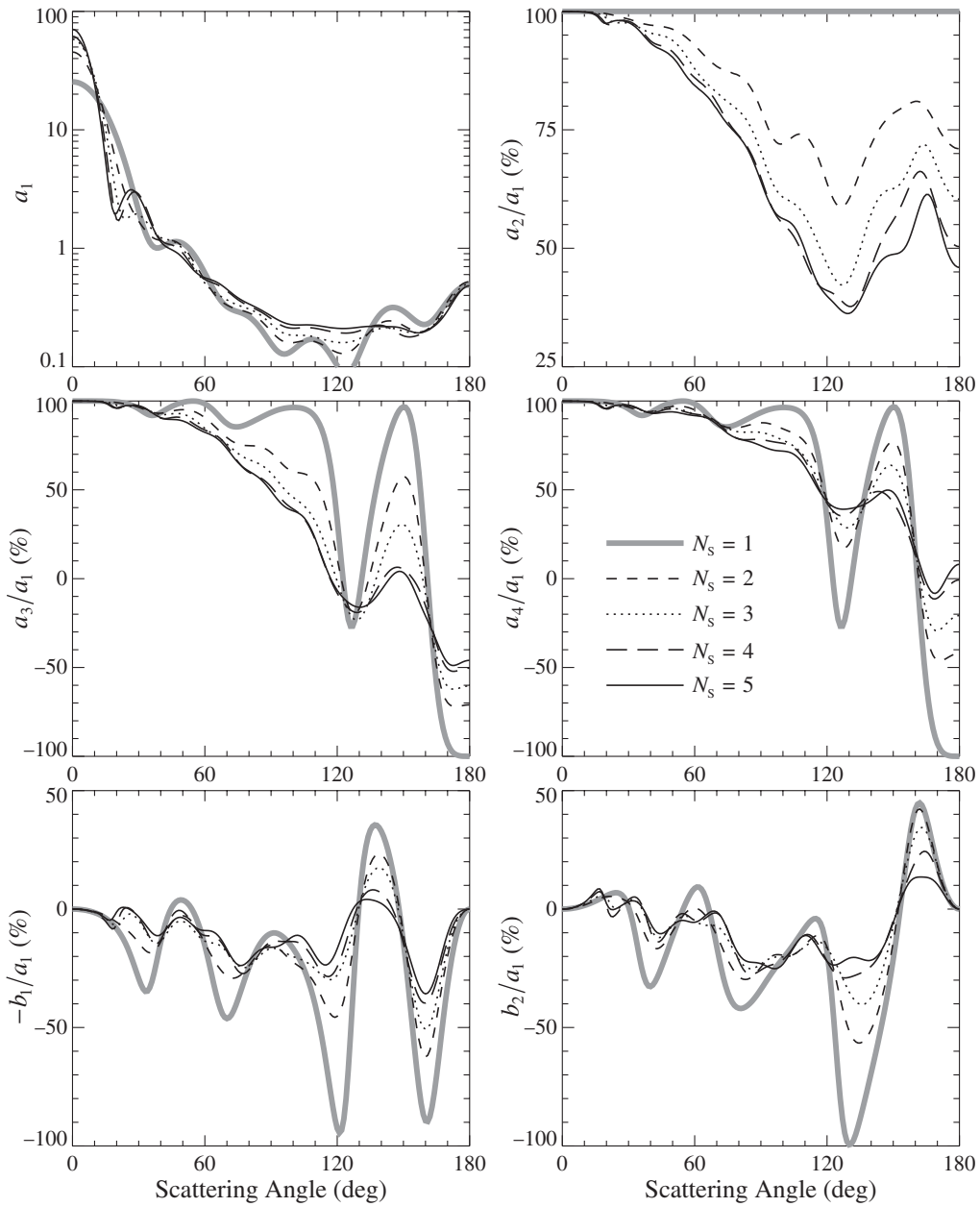

Figure 10.61. As in Fig. 10.60, but for packed clusters of N_s equal spheres. (After Mackowski and Mishchenko 1996.)

10.10 Particles with multiple inclusions

Another interesting class of scatterers are particles with multiple randomly positioned inclusions. Typical examples are water droplets and sulfate aerosols in the terrestrial atmosphere that contain various insoluble impurities (Chýlek *et al.* 1995, 1996), ice particles with internally trapped air bubbles and mineral and soot inclusions (Macke

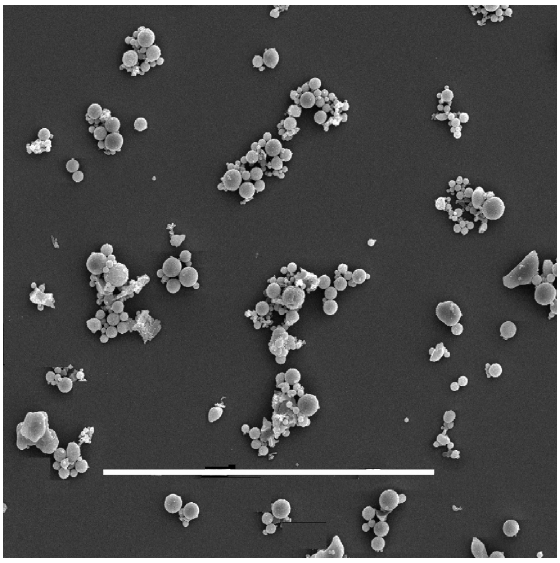

Figure 10.62. Scanning electron microscope photograph of inorganic fly ash particles produced by the combustion of powdered coal in electric powerplants. The length of the white bar corresponds to 100 μm. (From Muñoz *et al.* 2000b.)

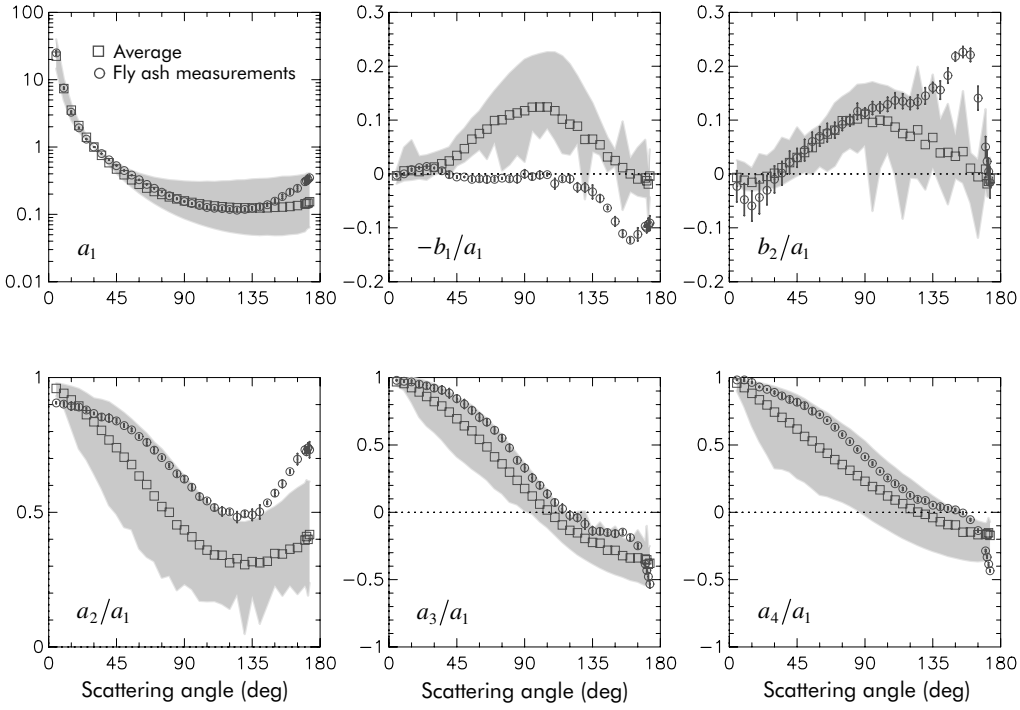

Figure 10.63. The circles depict the measurements by Muñoz *et al.* (2000b) for fly ash particles at a wavelength 633 nm. The squares show the average scattering matrix derived by Volten *et al.* (2001) using measurements for seven samples of compact mineral particles, while the gray bands indicate the domains of sample variability. The sign of the ratio b_2/a_1 is opposite to that adopted elsewhere in this book.

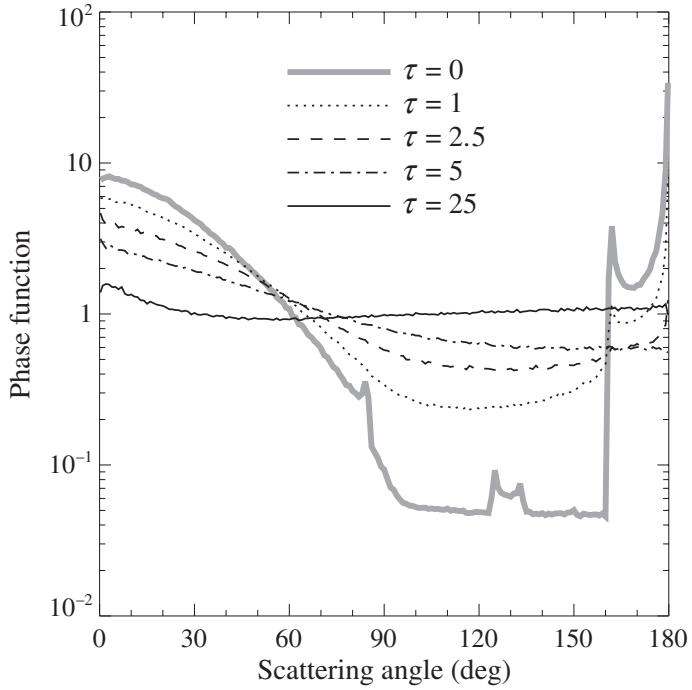

Figure 10.64. The ray-tracing part of the phase function versus scattering angle for a 50-μm-diameter spherical particle containing type-1 inclusions. The optical thickness of the inclusions increases from $\tau = 0$ (no inclusions) to $\tau = 25$ (after Mishchenko and Macke 1997).

et al. 1996a; C.-Labonnote *et al.* 2001), and inhomogeneous composites of mineral particles.

Light scattering by wavelength-sized spheres with a few inclusions can be computed using the superposition *T*-matrix method (cf. Section 5.9). When the host particle is much larger than the wavelength of the incident light, the only feasible approach is the Monte Carlo ray-tracing procedure described in Section 7.4. Figures 10.64 and 10.65 show the ray-tracing part of the phase function for a large spherical host particle with two types of small inclusions. The host has diameter $D = 50\,\mu\text{m}$ and refractive index relative to vacuum 1.55. The latter is a value typical of the real part of the refractive index of silicate materials. The inclusions are modeled as a gamma distribution, Eq (5.245), of spherical particles, with effective radius $0.5\,\mu\text{m}$ and effective variance 0.1. The refractive indices of the inclusions relative to vacuum are 1 (type 1, shown in Fig. 10.64) and 2 (type 2, Fig. 10.65). Type-1 inclusions represent small voids inside the host particle, whereas type-2 inclusions correspond to highly refractive impurities. The vacuum wavelength of the light is fixed at $0.55\,\mu\text{m}$. The overall scattering and absorption effect of the inclusions depends on their "optical thickness" $\tau = n_0 D\langle C_{\text{ext}}\rangle$, where n_0 is the inclusion number density and $\langle C_{\text{ext}}\rangle$ the average extinction cross section per inclusion. For reference, the total numbers of type-1 and type-2 inclusions inside the 50-μm-diameter spherical host corresponding to $\tau = 25$ are 29 469 and 18 967, respectively.

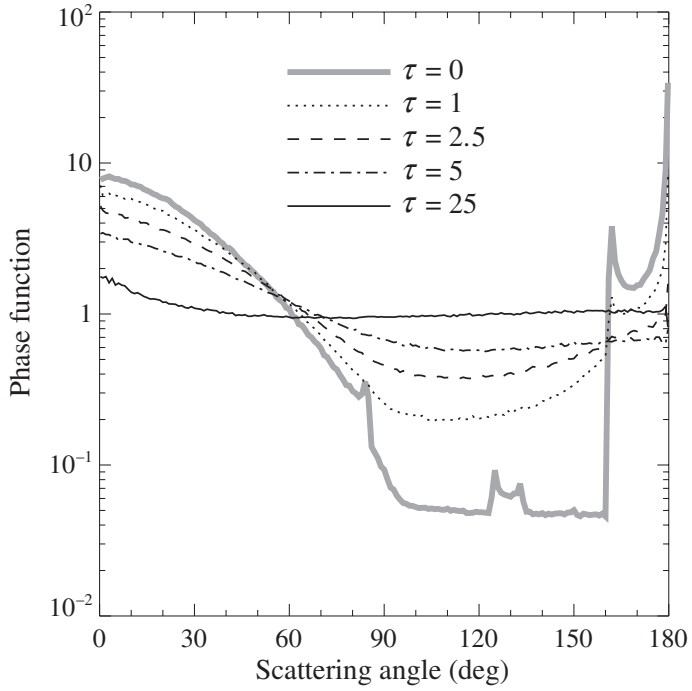

Figure 10.65. As in Fig. 10.64, but for type-2 inclusions (after Mishchenko and Macke 1997).

Figures 10.64 and 10.65 show that the ray-tracing phase function for a clear host (i.e., one having no inclusions) exhibits the pronounced geometrical optics features that are typical of large spherical particles and are discussed in detail in Section 9.4. With increasing τ, these features rapidly weaken and the ray-tracing phase functions become more and more isotropic, in qualitative agreement with the results of laboratory measurements by McGuire and Hapke (1995). Similarly, the effect of inclusions on the phase function of hexagonal ice crystals is to wash out the primary and secondary halos and the backscattering peak (Macke *et al.* 1996a). These effects can be explained qualitatively by increased multiple scattering among the inclusions, which tends to randomize the directions of rays exiting the host. Accordingly, the total asymmetry parameter of the composite spherical particles decreases from approximately 0.815 for $\tau = 0$ to approximately 0.5 for $\tau = 25$ (Fig. 10.66).

When the size of the inclusions is much smaller than the wavelength, a widely used approach is to assume that the composite particle is homogeneous and has an "effective" permittivity obtained by combining in a certain way the permittivities of the host and the inclusions. Several effective-medium approximations and their ranges of applicability are reviewed by Sihvola (1999) and Chýlek *et al.* (2000).

10.11 Optical characterization of nonspherical particles

There are two basic reasons why the optical characterization of nonspherical particles is significantly more involved than that of spherical particles. First, solving the direct

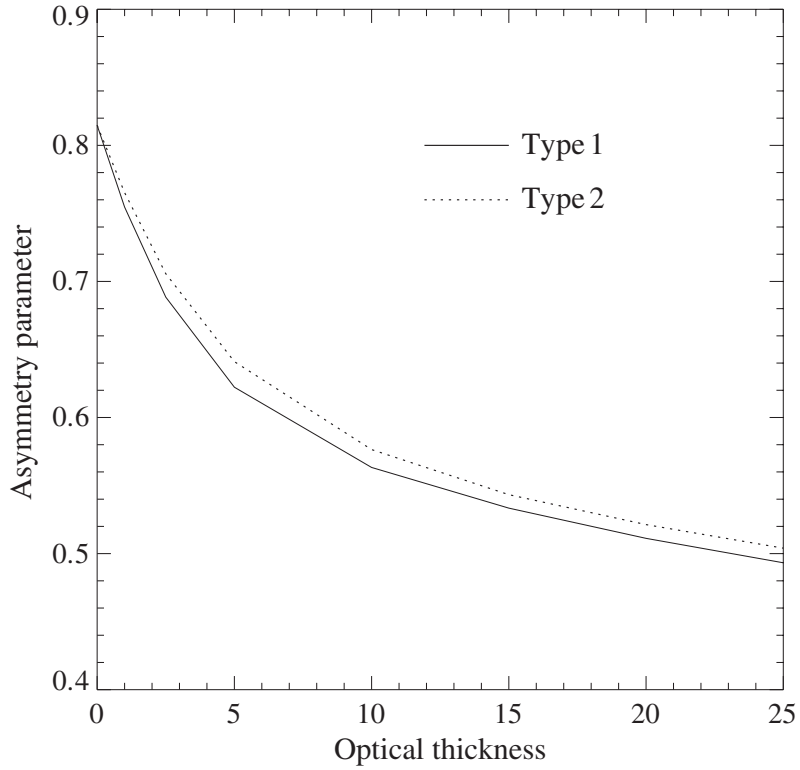

Figure 10.66. Total asymmetry parameter for 50-μm-diameter composite spherical particles containing type-1 and type-2 inclusions, with optical thickness varying from $\tau = 0$ (no inclusions) to $\tau = 25$ (after Mishchenko and Macke 1997).

scattering problem for nonspherical particles is more difficult than applying the standard Lorenz–Mie theory for spheres. Second, solving the inverse problem requires the introduction of at least two (and often many more) additional model parameters describing the particle shape and the orientation distribution function. These additional parameters are often unknown and must be retrieved from the experimental data, along with the particle size and the relative refractive index.

Apparently the simplest task is the detection of preferentially oriented nonspherical particles using the qualitative criteria summarized in Section 4.9. We have already mentioned in this regard observations of interstellar polarization and measurements of the depolarization of radio waves propagating through falling hydrometeors. Another technique involves directing the incident unpolarized beam along the z-axis of the laboratory reference frame and measuring the two-dimensional angular distribution of the scattered intensity. The lack of axial symmetry in this distribution will be an unequivocal indication of the presence of oriented nonspherical particles (see Figs. 10.1–10.5 and Section 10.1). This technique will fail, however, when axially symmetric particles are present whose rotation axes are also directed along the z-axis (note the upper left panels of Figs. 10.2–10.5). Also, it may be difficult to use such

measurements to say something specific about the particle microphysical characteristics. We have seen in Section 10.1 that the number of patches per unit solid angle in the scattering diagram may be indicative of the particle size parameter, while features such as the bright vertical bands in the upper right panels of Figs. 10.3 and 10.5 may suggest the presence of cylindrical particles with axes perpendicular to the scattering plane. However, more research is obviously needed in order to realize fully the potential information content of two-dimensional scattering measurements (e.g., Sachweh *et al.* 1995; Barthel *et al.* 1998; Dick *et al.* 1998; Kaye 1998; Braun and Krieger 2001; Crosta *et al.* 2001; Prabhu *et al.* 2001; Secker *et al.* 2001).

An interesting laboratory technique for detecting nonspherical aerosols is to subject the particles in question to a pulsed external electric field and look for accompanying changes in the particle optical properties (Kapustin *et al.* 1975, 1980). The amplitude of the field is chosen to be sufficient to cause a significant degree of particle alignment provided that the aerosols are nonspherical, while the duration of the pulse is long enough to allow an equilibrium orientation to be reached. After the electric field is turned off, the particles return to random orientation, owing to Brownian motion. Any differences in the elements of the phase and extinction matrices or the total optical cross sections between the states with the electric field turned on and off indicate the presence of nonspherical particles. Furthermore, the magnitude of the differences and the relaxation time for the disorientation process after the electric field is turned off may indicate a value for the average particle aspect ratio.

As we have seen previously (cf. Section 4.9), the only unequivocal indicator of nonsphericity for randomly oriented particles forming a macroscopically isotropic and mirror-symmetric medium is violation of the Lorenz–Mie identities $F_{22}(\Theta) \equiv F_{11}(\Theta)$ and $F_{44}(\Theta) \equiv F_{33}(\Theta)$. As a consequence, the linear and circular backscattering depolarization ratios defined by Eqs. (10.2) and (10.3) become non-zero. Backscattering depolarization measurements are widely used for detecting and characterizing nonspherical particles in lidar (Gobbi 1998; Sassen 2000) and radar (Aydin 2000; Bringi and Chandrasekar 2001) atmospheric remote sensing and biomedicine (Schmitt and Xiang 1998; de Boer *et al.* 1999). For example, Liu and Chandrasekar (2000) and Straka *et al.* (2000) reviewed the foundation of fuzzy logic systems for classification of hydrometeor type based on polarimetric radar observations. Sassen (1991) developed a depolarization classification of different cloud-particle types based on data collected by a helium–neon continuous-wave laser-lidar analog device in the laboratory and field during the early 1970s (Fig. 10.67). Browell *et al.* (1990) used lidar depolarization observations to differentiate between various types of polar stratospheric clouds. Although most lidars operating at visible wavelengths measure the linear depolarization ratio, measurements of the circular depolarization ratio are also gaining popularity (Woodard *et al.* 1998).

The strong depolarization of light by large transparent particles such as ice cloud crystals at visible wavelengths (Fig. 10.67) is traditionally attributed to refractions and multiple internal reflections (Fig. 7.2), which tend to randomize the polarization

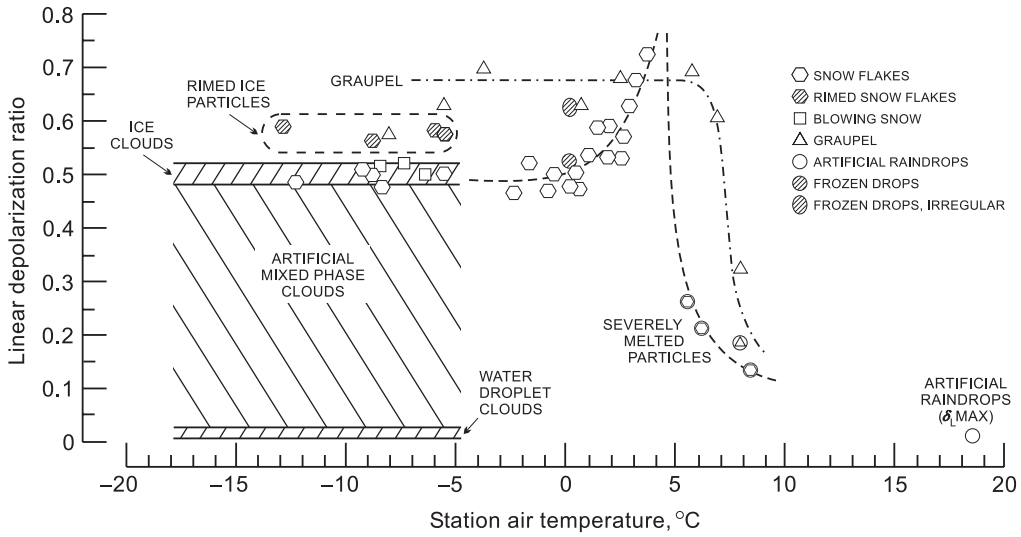

Figure 10.67. Results of early laboratory and field studies showing the wide range of linear depolarization ratios encountered from various types of hydrometeors at visible wavelengths (from Sassen 1991).

plane of rays exiting the particle (Liou and Lahore 1974). However, the geometrical optics concepts of rays, refractions, and reflections become inapplicable when the size of the particle is comparable to the wavelength. Yet wavelength-sized particles can produce even larger depolarization ratios, as demonstrated in Fig. 10.68. An interesting feature of essentially all the depolarization curves shown in this figure and computed with the exact *T*-matrix method is a rapid increase in δ_L as the effective size parameter increases from 0 to about 10. Moreover, maximal δ_L-values for most shapes are observed at size parameters close to and sometimes slightly smaller than 10. The *T*-matrix results show no obvious relationship between δ_L and the particle aspect ratio. Even spheroids with aspect ratio as small as 1.05 (a 2.5% deviation from the perfect spherical shape) produce strong depolarization. The largest δ_L-values are generated by prolate spheroids with aspect ratios as small as 1.2 (a 10% deviation from a sphere). Furthermore, δ_L for spheroids and, especially, cylinders tends to saturate with increasing aspect ratio.

The steep rise in δ_L with size parameter in the range $0 \lesssim x_{\text{eff}} \lesssim 10$ exhibited by the *T*-matrix results can explain the initial increase in lidar linear depolarization with time for very young, rapidly growing aircraft condensation-trail (contrail) particles observed by Freudenthaler *et al.* (1996). Figure 10.68 suggests that further growth of ice particles may lead to a decrease in δ_L with time, which was indeed observed by Sassen and Hsueh (1998). Furthermore, the *T*-matrix results seem to explain the occurrence of unusually large depolarization ratios for contrails ($\delta_L \sim 0.65$), which exceed significantly the values normal for most cirrus ($\delta_L \sim 0.35$–0.5). Similar *T*-matrix computations have been used by Carslaw *et al.* (1998), Toon *et al.* (2000), Beyerle *et al.* (2001), and Liu and Mishchenko (2001) to explain the results of lidar

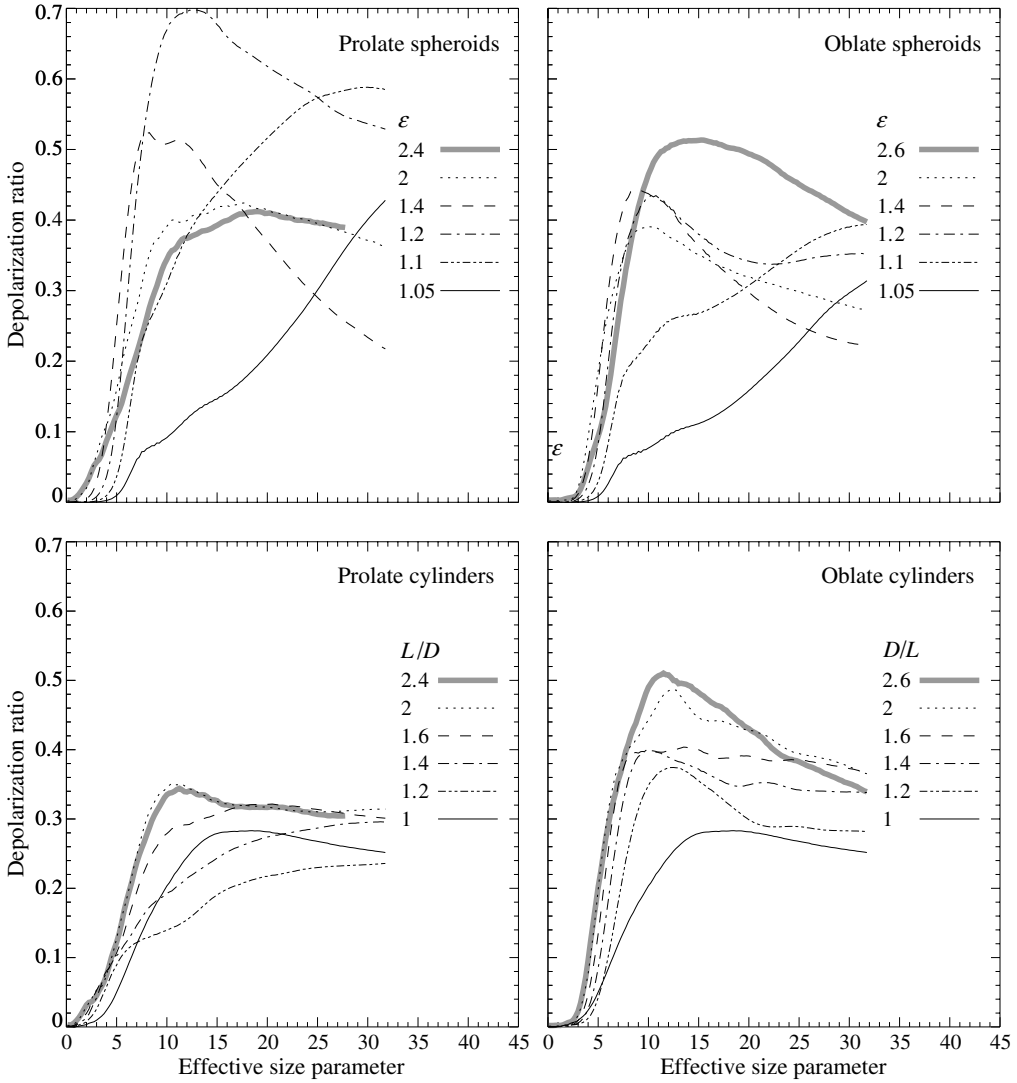

Figure 10.68. Linear backscattering depolarization ratio versus effective size parameter for polydisperse, randomly oriented ice spheroids with aspect ratios ranging from 1.05 to 2.6 and circular cylinders with various length-to-diameter or diameter-to-length ratios. The relative refractive index is 1.311 and the size distribution is given by Eq. (5.246) with $\alpha = -3$ and $v_{\text{eff}} = 0.1$. (After Mishchenko and Sassen 1998.)

observations of polar stratospheric cloud particles, which are another interesting example of natural wavelength-sized scatterers generating strong depolarization ratios.

In view of the apparent strong dependence of depolarization on size parameter for wavelength-sized particles, measuring depolarization at multiple wavelengths should be very useful for retrieving particle size and studying its temporal evolution. As an example, Plate 10.9 shows a variety of remote sensing observations of a mesoscale cirrus cloud band with contrails along its edges performed by Sassen *et al.* (2001) on 5 March 1999. It can be seen from the fish-eye images and the depolarization

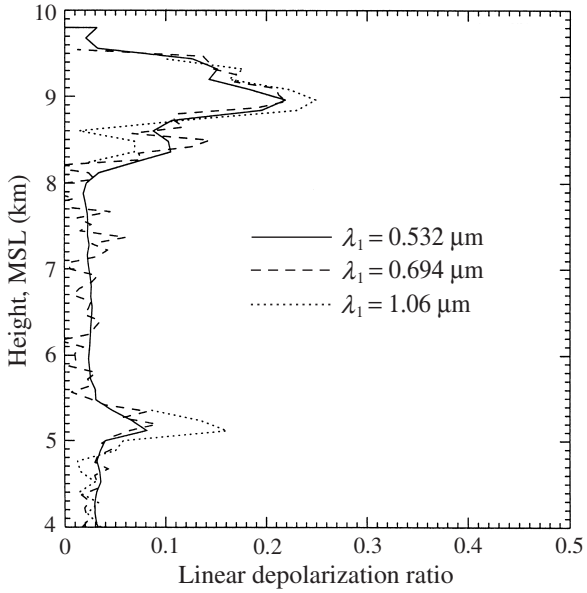

Figure 10.69. Comparison of 5-minute-averaged (1854–1859 UTC) linear depolarization profiles for three lidar wavelengths during a period when the backscattered intensity from the elevated aerosol layer was relatively strong. Table 10.5 gives the depolarization values at the ~5.25 km aerosol maximum in terms of the total molecular and aerosol and aerosol-only values. (From Sassen *et al.* 2001.)

displays that the contrails occurred just above the cirrus cloud top at the very beginning (missing the contrail leading edge) and at the end of the measurement period, when two contrails passed overhead in succession. Although the backscattered intensity displays at the $0.532\,\mu m$ (bottom left panel) and $1.06\,\mu m$ (bottom right) wavelengths are similar, there are large differences between the respective depolarization displays. The significantly smaller δ_L-values in the contrail at the longer wavelength imply the presence of $\sim 2\,\mu m$ diameter crystals (cf. Fig. 10.68), despite the fact that the contrails were probably of order one hour old when observed in the zenith. In contrast, the δ_L-values in the main cirrus cloud at the two wavelengths are quite similar, as can be expected of nonabsorbing particles with sizes much larger than a wavelength. It can, therefore, be concluded that contrails are unique among ice clouds in their ability to generate and maintain sufficiently tiny ice-particle sizes to manifest the depolarization dependence typical of the transition zone between the Rayleigh and the geometrical optics region of size parameters.

Another interesting feature of the lidar displays in Plate 10.9 is the significant depolarization caused by the elevated aerosol layer centered at about 5.3 km. This aerosol was almost certainly a product of the transport of dust from Asian dust storms. As more clearly seen in Fig. 10.69, the δ_L-values at the three lidar wavelengths reveal differences which may be attributed partly to significant noise in the weak aerosol backscattering and partly to the decreasing contribution of weakly depolarizing

Table 10.5. Linear depolarization ratio at the ~ 5.25 km aerosol maximum in terms of the total molecular and aerosol (δ_{L}) and aerosol-only ($\delta_{\mathrm{L,a}}$) values at the three lidar wavelengths (after Sassen *et al*. 2001)

λ_1 (μm)	δ_{L}	$\delta_{\mathrm{L,a}}$
0.532	0.08	0.21
0.694	0.09	0.23
1.06	0.16	0.25

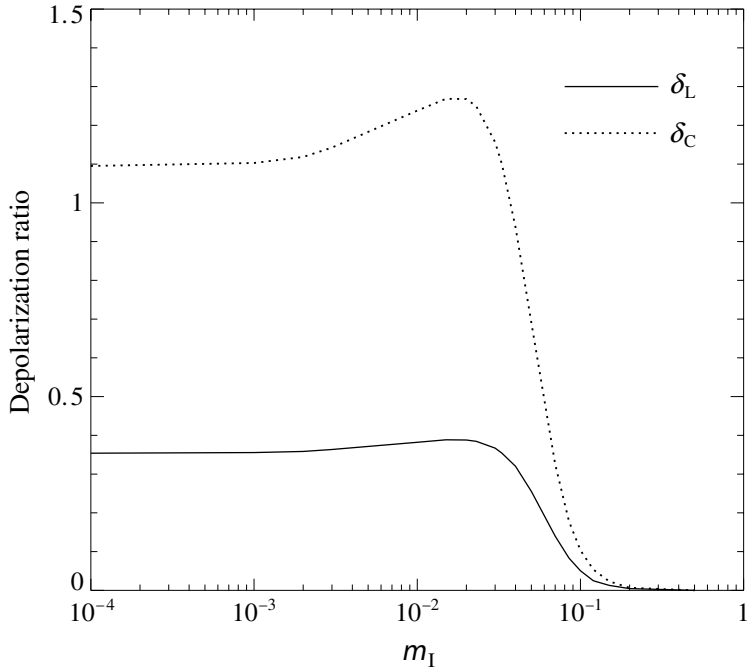

Figure 10.70. Linear and circular backscattering depolarization ratios versus imaginary part of the relative refractive index for polydisperse, randomly oriented oblate spheroids with $a/b = 1.7$. The size distribution is given by Eq. (5.246) with $\alpha = -3$ and $v_{\mathrm{eff}} = 0.1$. The effective surface-equivalent-sphere size parameter is $x_{\mathrm{eff}} = 15$ and the real part of the relative refractive index is 1.31.

molecular scattering to the total molecular plus aerosol depolarization with increasing wavelength (cf. Eq. (7.6), which indicates that the molecular contribution to the total molecular plus aerosol scattering matrix decreases as the inverse fourth power of wavelength). Table 10.5 shows that when the molecular backscattering contributions are approximately removed, the aerosol-only peak depolarization values are about 0.2–0.25, which is similar to the strong Kosa dust-dominated depolarization measured in Japan (Murayama *et al.* 1999; Sassen 2000). The spectral effect of molecular scattering on the total molecular plus cloud depolarization, the feature at about 9 km

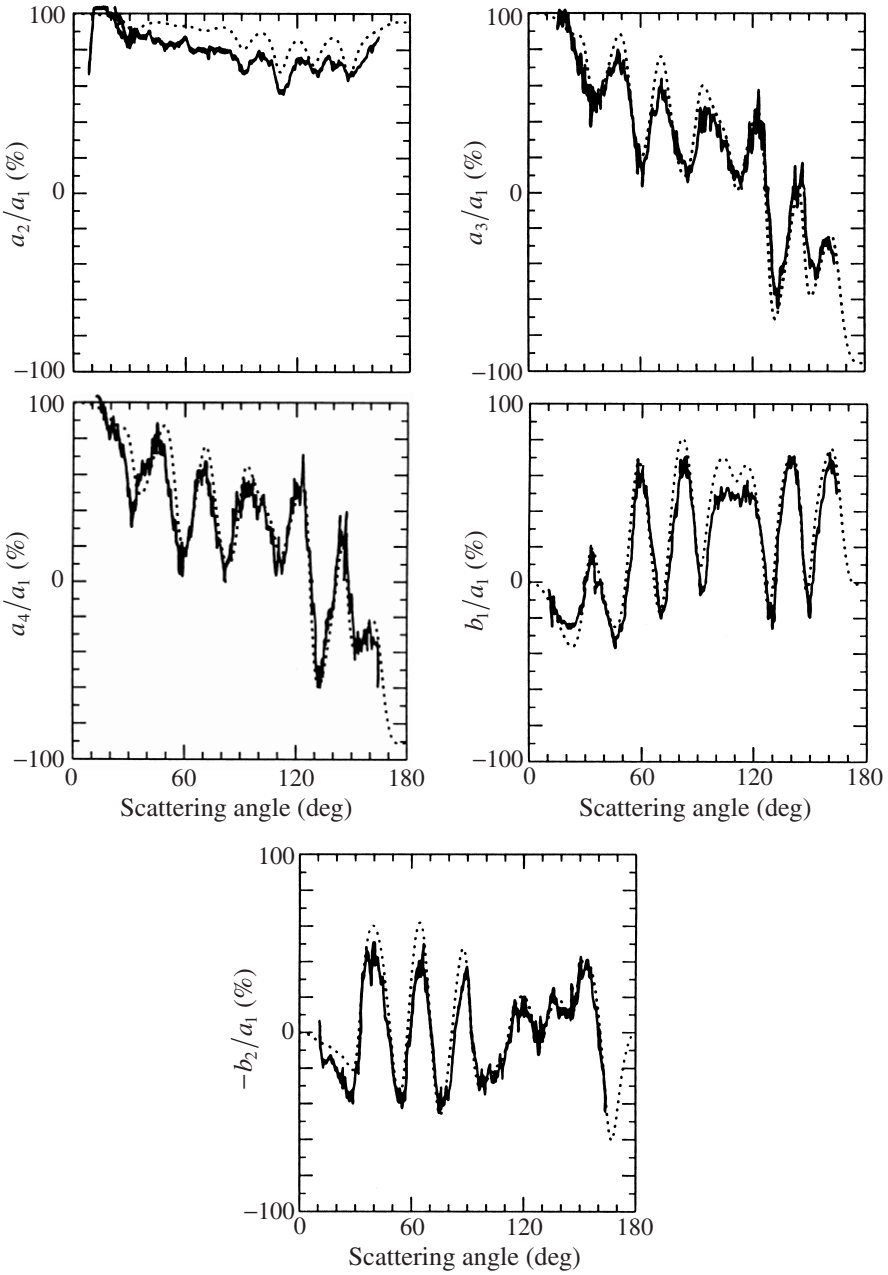

Figure 10.71. Ratios of the elements of the normalized Stokes scattering matrix for a latex two-sphere cluster in random orientation. The solid curves depict laboratory data of Bottiger *et al.* (1980) at a wavelength 441.6 nm, whereas the dotted curves show the results of *T*-matrix computations for a component-sphere diameter 1129 nm.

in Fig. 10.69, is significantly weaker because of the much stronger cloud backscattering.

We saw in Section 10.2 that increasing imaginary part of the relative refractive index m_{I} reduces and eventually eliminates the differences between the scattering pat-

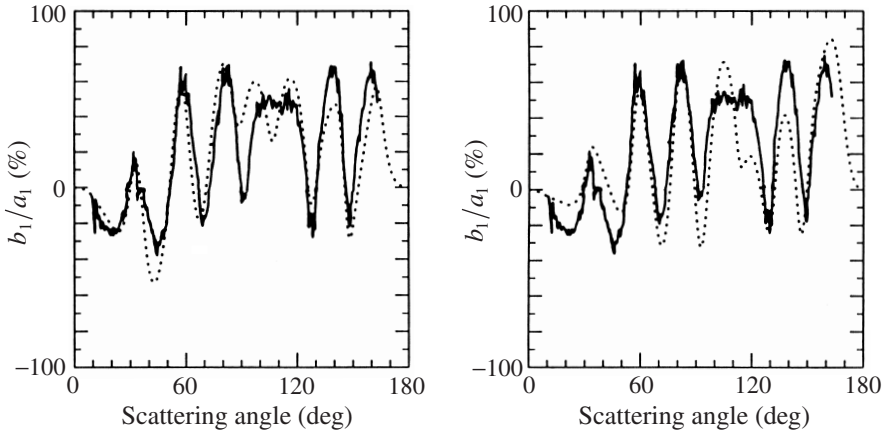

Figure 10.72. As in Fig. 10.71, but for component-sphere diameters 1108 nm (left-hand panel) and 1150 nm (right-hand panel).

terns of spherical and surface-equivalent convex nonspherical particles. Accordingly, increasing m_I leads to reduced and ultimately zero linear and circular depolarization ratios, as Fig. 10.70 illustrates. This factor limits the usefulness of depolarization observations of cirrus clouds and contrails at infrared wavelengths (Eberhard 1992), where water ice is strongly absorbing (Warren 1984).

A more detailed characterization of randomly oriented nonspherical particles can be achieved by exploiting multi-angle measurements of the full scattering matrix (e.g., Volten *et al.* 1999). The results can be especially precise when one or more particle microphysical parameters are known beforehand. As an example, Figs. 10.71 and 10.72 parallel Figs. 9.30 and 9.31 in showing the results of laboratory measurements (Bottiger *et al.* 1980) and *T*-matrix computations (Mishchenko and Mackowski 1996) for a two-sphere cluster with touching components. An electrostatically levitated latex bisphere was subject to Brownian motion and rapidly changed its orientation during the measurement. Therefore, although the sample was a single particle, the measurement of the scattering matrix was equivalent to that for randomly oriented monodisperse particles. According to Bottiger *et al.*, this was indeed corroborated by simultaneous measurements of the (1,3), (1,4), (2,3), (2,4), (3,1), (3,2), (4,1), and (4,2) elements of the scattering matrix, which were all found to be zero within the experimental accuracy (cf. Eq. (4.51)). Since the particle morphology and relative refractive index are known, the only free parameters are the diameters of the component spheres. Mishchenko and Mackowski have found that good agreement between the results of *T*-matrix computations and laboratory measurements can be obtained for component sphere diameters equal to 1129 nm (Fig. 10.71). Figure 10.72 shows the results for sphere diameters 1108 nm and 1150 nm, which give limits on the plausible range of diameters. This illustrates once again the potential accuracy of particle sizing techniques based on measurements of the scattering matrix.